Theoretical and Numerical Analysis of Laminar Ethanol Spray Flames for the creation of a Spray Flamelet Library

Christos Panagopoulos

Technische Universiteit Delft

TU Delft Delft University of Technology

Challenge the future

Theoretical and Numerical Analysis of Laminar Ethanol Spray Flames for the creation of a Spray Flamelet Library

by

Christos Panagopoulos

in partial fulfillment of the requirements for the degree of

Master of Science
in Mechanical Engineering

at the Delft University of Technology,
to be defended publicly on Friday July 7, 2017 at 09:00 AM.

Supervisor:	Prof. Dr. D.J.E.M. Roekaerts
	Dr. Likun Ma
Thesis committee:	Dr. ir. R. Pecnik
	Dr. D. J. P. Lahaye
	M.Sc. X. Huang

P&E report number 2827

TU Delft Delft University of Technology

Abstract

Combustion of fuels appears in many sets of equipment and applications that involve transformation of a primary not useful form of energy into a secondary usable one that can be employed for purposes of electricity generation, transportation and industrial thermochemical processes. Strict environmental regulations demand for the reduction of the pollutants emissions (e.g. NO_x CO_2, CO, SO_2, etc.) that are responsible for the global warming of the planet and the formation of acid rain and smog. Since renewable energy sources cannot replace the use of fossil fuels in the foreseeable future alternative ways have to be investigated. Combustion of biofuels such as liquid ethanol, a well known and widely used alcohol, under MILD (Moderate or Intense Low-oxygen Dilution) conditions is a scenario on that direction. From the one hand, combustion of biofuels offers sustainability and lower greenhouse gas emissions and from the other, MILD conditions offer more uniform and lower peak temperature profiles reducing so the nitrogen oxides emissions and increasing the lifetime of the combustion chamber.

However, modeling of ethanol spray turbulent combustion is a complicated problem since it involves many different phenomena that are coupled between each other including the injection of the spray, the atomization into droplets and the dispersion in the domain, the turbulence of the gaseous flow, the mass, momentum and energy exchange between the two phases and finally the combustion. The closure of the unresolved chemical source terms in the numerical analysis of such a problem is a challenge and the Flamelet Generated Manifolds (FGM) method appears as a perspective approach to deal with it. This method approximates the turbulent flame as an ensemble of laminar, thin, one dimensional, counterflow flames the so-called flamelets. In that way the chemical reactions can be decoupled from the turbulence field and be calculated separately. The results are stored in look-up tables that are retrieved during the turbulence simulation with the use of connecting variables. Not having found a way so far to relate a spray flamelet look-up table with the turbulence flow many researchers create a gaseous flamelet table instead ignoring the spray and evaporation effects in it. As it has been reported this omittance can possibly lead to over-prediction of the temperature and important species profiles in the modeling of the turbulent flame. In this study, both a gaseous and spray ethanol flamelet library are created so that a direct comparison between the two can be done. The interference of spray influences the structure of the flame making it deviate significantly from the gaseous flamelets.

The results show that not only the strain rate (as for the case of the gaseous flamelets), but also the equivalence ratio implied in the fuel side and the initial droplets' diameter influence the flame structure of the spray flamelets. A non-slip velocity between the droplets and the carrier gas is kept as a boundary condition for all the cases. Increased initial droplets' momentum due to increased strain rate and initial diameter makes the droplets survive and follow longer trajectories in the domain. If droplets manage to cross the stagnation plane and meet the opposing gaseous stream, one or more droplets' reversals are observed. The motion of droplets in the domain is associated with the evaporation process the location of which affects the viability of the flame. Enhanced evaporation at the stagnation plane favors the creation of a double reaction zone. If the ethanol vapor is brought in the reaction zone

at a high temperature level a hotter flame compared to the gaseous case can be created. Moreover, if evaporation takes place in regions where combustion is not strong enough, local flame extinction might happen. Thus, not only the residence time of the reactants (as for the case of the gaseous flamelets), but also the location and the intensity of the evaporation affect the flame structure. Decomposition of the ethanol gas into intermediate species can occur for all the cases but is more apparent in the gaseous flamelets and for lower strain rates. Mass fraction profiles of CO_2 and H_2O indicate the outer flame structure and follow the temperature profile, while local presence of CO indicates that the reactions are weakened, incomplete or they have just started. Local evaporation of the droplets is also predicted by the evaporation source term of the continuity equation and at the location where a local peak is observed additional peaks of the ethanol and oxygen consumption rates are found which are in a stoichiometric ratio. For increased droplets' initial momentum, slip velocity effects are found that lead to increased drag force and the deceleration of the droplets. Increasing the equivalence ratio at the boundary two reaction zones are observed for all the cases, but it does not influence the motion of the droplets. Finally, as a result of the evaporation two or more peaks of scalar dissipation rate can be found compared to the single peak observed in the gaseous flamelets.

It becomes evident that the motion and the evaporation of the droplets strongly affects the flame structure. More reaction zones, of varying intensity and location can be found in the spray flamelets. Temperature and species profiles show deviations between the two libraries and as a result the creation of a complete spray flamelet library and finding a way to relate it with the turbulence calculation is an important issue to be studied in a future study. Finally, it is also recommended that the influences of a slip boundary velocity condition should be studied for the spray calculations.

Acknowledgements

I would like to thank and express my highest gratitude to my supervisor Professor D.J.E.M. Roekaerts for his kind, patient and always creative supervision. Through the discussions we had all this time, for me it was a great pleasure to listen to his ideas and advises which could always keep me on the right track and inspire me for thinking alternative possible solutions for the completion of this thesis. His expertise in writing and reviewing scientific reports also gave me insight on how to report with consistency, be explanatory and describe in a correct and scientific way the fundamental aspects of theory and calculations.

I would also like to express my sincere gratitude to Dr. Likun Ma for his kind and passionate willingness to discuss with me technical and theoretical aspects of combustion. His guidance and assistance in the new programming environment for me of OpenFOAM was invaluable. Moreover, I would also like to thank Xu Huang for the fruitful discussions we had and the advises he gave me for both programming and theoretical issues i faced during my thesis project.

Special thanks go to the examination committee for taking time to read and evaluate my thesis. I want also to acknowledge the NWO Physical Sciences for providing me supercomputer facilities.

I would also like to express my gratitude to my family for their unconditional support, love and encouragement they showed to me all these years. Many thanks go to my friends Pradeep, Liang and Bao here in Delft for the pleasant time we spent together. The last words are for Eugenia and Nikos for their warm encouragement and support despite the distance.

Christos Panagopoulos
Delft, June 2017

Contents

List of Figures

List of Tables

Nomenclature

L	characteristic length
p	pressure
T	temperature
V	velocity vector
Y_k	mass fraction of species k
x, y, z	spatial cartesian coordinates
t	time
u, v, w	scalar velocity components
S	surface area that surrounds a control volume
$\mathcal{V}$	control volume
dS	elemental surface area
$d\mathcal{S}$	normal vector upon an elemental surface area, pointing out
$d\mathcal{V}$	elemental control volume
F	force
m	mass
f	net body (volume) force
$\mathrm{V_k}$	diffusion velocity of species k
$\mathrm{u_k}, \mathrm{v_k}, \mathrm{w_k}$	scalar diffusion velocity components
$\dot{q}_v$	rate of volumetric heat per unit mass
$\dot{q}_x, \dot{q}_y, \dot{q}_z$	surface heat fluxes
h	specific enthalpy
k	thermal conductivity
$\cdot q$	surface heat flux vector
e	specific internal energy
h_s	sensible enthalpy
h_{chem}	chemical enthalpy
$\Delta h^o_{f,k}$	enthalpy of formation
C_p	specific heat at constant pressure
R	specific gas constant
D_k	species mass diffusivities
D_{th}	thermal diffusivity
W_k	molecular weight of species k
v''_{kj}, v'_{kj}	molar stoichiometric coefficients in reaction j
Q_j	rate of progress of reaction j
$[X_s]$	molar concentration of species s
K_{fj}, K_{rj}	forward and reverse rates of reaction j
A_{fj}	preexponential constant of Arrhenius law
E_j	activation energy of reaction j
R_u	universal gas constant
ΔS^0_j	entropy change for reaction j
ΔH^0_j	enthalpy change for reaction j
W	mean molecular weight

X_k	mole fraction of species k
S^v	source terms due to spray evaporation
m_p	mass of a particle or droplet
$\dot{m}_v$	time rate of the fuel vapor mass leaving a droplet
x_p	position vector of a particle or droplet
V_p	velocity vector of a particle or droplet
V_{seen}	velocity of the gaseous phase at the location of a droplet
D_p	particle's diameter
C_D	drag coefficient
$\widetilde{V}$	velocity vector of a mean flow
u''_{seen}	fluctuating velocity
L_v	latent heat of evaporation
s	stoichiometric ratio
Z	mixture fraction
z	normalized mixture fraction
a	strain rate
Y_c	progress variable
C	normalized progress variable
r	numerical residual
e	numerical error

Greek symbols

λ	mean-free path
ρ	density
τ	viscous (surface) stress
μ	dynamic viscosity
λ	bulk viscosity
$\dot{\omega}_k$	rate of production of species k
β_j	temperature exponent of Arrhenius law
τ_p	particle relaxation time scale
ρ_p	particle's density
μ_{film}	dynamic viscosity evaluated at a film layer around a particle
β	evaporation parameter
χ	scalar dissipation rate
$\dot{\omega}_T$	combustion heat release
τ_f	flow time scales
τ_c	chemical time scales
τ_t	turbulent time scale
Φ	equivalence ratio

Dimensionless numbers

M	Mach number
Re_p	particle's Reynolds number
B_M	Spalding mass transfer number
Nu	Nusselt number
Sh	Sherwood number
Pr_{film}	Prandtl number, evaluated in the film layer of a droplet

Sc_{film}	Schmidt number, evaluated in the film layer of a droplet
Da	Damkohler number

Abbreviations

FGM	Flamelet Generated Manifold
CFD	Computational Fluid Dynamics
DNS	Direct Numerical Simulation
RANS	Reynolds Averaged Navier Stokes
LES	Large Eddy Simulation
PDF	Probability Density Function
OOP	Object Oriented Programming
PCG	Preconditioned Conjugate Gradient method
PBiCG	Preconditioned Bi-Conjugate Gradient method

1

Introduction

1.1. Energy demands, environmental issues and possible solutions

The global energy demands are increasing year by year mainly due to the continuous growth of the population and the unstoppable industrial developments. According to the annual report of International Energy Agency (IEA) [3] the total energy consumption has been doubled from the year of 1973 till 2014. The fossil fuel resources as an energy supply hold the lion's share with eighty percent of the total energy supplies, a contribution that has barely changed the last forty years. Their usage originates back to the ancient history mainly for heating purposes, and their exploitation as a mean of work production comes with the Industrial revolution of the 19th century and the development of the steam engines. The easy and direct access to the fossil fuel resources, their high energy efficiency and their technical background knowledge that has already been established makes them as the first energy supply choice for the industrial energy sector.

Nevertheless, the conventional combustion of the fossil fuels promotes the formation of chemical species that affect the public health and cause environmental issues. To name a few, the sulfur dioxide (SO_2) which is a product of coal burning and the nitrogen oxides (NO_x) induce acid rain which has harmful effects in the flora and fauna but also in the human respiratory system. Also, the carbon monoxide (CO) which is formed due to partial oxidation of carbon-containing compounds is a highly toxic and poisonous compound and on the other hand, complete oxidation leads to creation of carbon dioxide (CO_2) which is a greenhouse gas and contributes to the global warming of the planet.

For those reasons the last decades, research is on progress attempting to explore the potentials of exploiting renewable energy resources. Governments and global earth/welfare organizations in turn push on that direction by legislating strict policies and regulations for reducing pollutants emissions and providing funds for the intensification of the research effort. However, due to serious technology limitations and the same time the strong dependency of renewable sources on local place, weather and time conditions, it seems that the energy market is not going to be released from its dependence on the fossil fuels in the foreseeable future. Indeed, according to the projections of IEA [4] it is expected that the fossil fuel resources will keep on constituting a share of more than the three quarters of the total energy supply by 2040. Therefore, apart from the research in the renewable energy resources, an

emphasis should be given in the optimization of the combustion of fossil fuels by improving the combustion as a process introducing new techniques and the same time replacing fuels that in proof are damaging for the environment by more eco-friendly fuels such as biofuels.

1.2. MILD Combustion

A recent and promising combustion technique that can drastically reduce the NO_x emissions with no cost in the overall efficiency is the MILD (Moderate or Intense Low-oxygen Dilution) combustion. According to this concept as it is described by in [5], the oxidizer is introduced at high temperature above the auto-ignition point of the fuel. Usually, the oxidizer is constituted of conventional combustion products and as a result it contains low amount of oxygen. A.Cavaliere et al. [5] define the term MILD combustion for a premixed system as the combustion process in which the inlet temperature of the reactant mixture is higher than mixture self-ignition temperature, whereas the maximum allowable temperature increase with respect to inlet temperature during combustion is lower than mixture self-ignition temperature. According to [5], the characterization MILD (apart from the acronym name) is given because under these operating conditions the resulting temperature range is not wide from the one hand and the evolution of the molecular transport phenomena (e.g. diffusion) is gradual and "mild". The main advantage of MILD combustion is that by controlling the temperature inlet and the oxygen level of the reactants, a limitation of the maximum temperature in the reaction can be obtained resulting in reduced formation of soot and NO_x [5]. Moreover, the control over the maximum reaction temperature is useful for safety reasons and the prolongation of the lifetime of the combustion chamber. However, as A.Cavaliere et al. [5] warn, achieving lower reaction temperature, it may lead to partial oxidation of chemical components (e.g. carbon-based components) and the formation of possible pollutants.

1.3. Biofuels

An alternative way for reducing the fossil fuels consumption rate and limit the same time the pollutants emissions that are catastrophic for the environment is the use of biofuels. P.Nigam et al. [6] distinguish biofuels into primary where organic material (e.g. wood, pellets) is used in its natural and non-modified chemical form and secondary where biomass material is modified and processed to create biofuel products. Depending on the type of process that the biomass undergoes a further classification of the secondary biofuels can be made. Thus, we distinguish between the first generation where biofuels are produced through biochemical conversion, the second generation where thermochemical processes are used instead and the third one in which the biofuels' feedstock is algae [6]. Compared to fossil fuels, biofuels have regional independency since they are not a matter of geological anaerobic processes in the Earth's crust and can be developed locally. In addition, biofuels offer sustainability and reduction of greenhouse gas emissions [7]. The greenhouse gases reduction is considered based on the fact that the carbon dioxide is recycled, starting from the process of generating biomass feedstock where CO_2 is consumed (e.g. photosynthesis) and ending to the combustion of the biofuel where CO_2 is emitted back to the atmosphere [7]. Among the different kinds of biofuels, ethanol is one of the most well known and widely used biofuel. It is an alcohol and comes as a liquid component at atmospheric conditions (boiling temperature is 351K) and falls under the category of the first generation of secondary biofuels. To some extend, ethanol can be considered as a form of renewable energy, since its production starts by transforming solar

to chemical energy [8]. The produced chemical energy is stored in carbohydrate molecules, which in turn break into sugar molecules through a hydrolysis reaction. As a next step the sugar components are converted into alcohol via fermentation. The main crops that favor for alcohol/ethanol production are sugarcane and corn [7].

1.4. Numerical analysis of turbulent spray combustion

Combustion of fuels appears in many sets of equipment and applications that involve transformation of a primary not useful form of energy into a secondary usable one that can be employed for purposes of electricity generation, transportation and industrial thermochemical processes. Hence, it is important that the burner or the combustion chamber be designed in an optimal way for operational and safety reasons. For the design of such devices and the prediction of the flame structure and the pollutants emissions as well, numerical analysis appears as an ideal tool. In that way, decisions for the geometry, the dimensions and the materials can be taken in advance without having to set up testing devices, saving time and money. A very efficient computational method for modeling turbulent combustion in terms of accuracy and simulation time is the Flamelet Generated Method (FGM) [9] in which the chemical reactions are decoupled from the turbulence field and are calculated separately in a laminar approach following certain assumptions. According to this approach, the chemistry is resolved in counterflow, one dimensional laminar simulations (flamelets) of varying boundary conditions. The results of those laminar simulations are stored into tables and are retrieved during the simulation of the turbulence flow using appropriate connecting variables/indices that make up the link between the two.

1.5. Objectives

Following this procedure, L.Ma [2] recently developed and validated a predictive computational model for ethanol spray combustion in MILD conditions. The validation of the model was based on the Delft Spray-in-Hot-Coflow (DSHC) experimental dataset. The DSHC burner has been designed in the University of Technology of Delft to study the fundamental aspects of MILD combustion of light oils [10]. L.Ma's results [2] showed quite good agreement with the respective experimental ones except from the regions of the flame where strong evaporation effects were present leading to an over-prediction of the temperature profile locally. A reason for this divergence could possibly be the fact that he generated the laminar flamelet table based on a gaseous ethanol stream ignoring the spray and evaporation effects in that part.

In this thesis the aim is to investigate this possibility and to do so two sets of laminar flamelets are calculated. In the first one the ethanol fuel is provided in an already vaporized form, so no liquid phase is present and we name this set as gaseous flamelets and for the second one, the ethanol appears in a cloud of droplets and we name it as spray flamelets. In the second case, the motion and the evaporation rate of the droplets in the computational domain is expected to influence the structure of the flame. As a result, we aim to investigate to what extent the two sets of flamelets differ and what are the parameters that make them deviate. To answer this question temperature, important species mass fractions, consumption rates of fuel and oxidizer and evaporation rates are some of the quantities that need to be considered. The appearance of the liquid phase in the spray flamelets introduces additional variables related to the size, the velocity and the amount of the droplets increasing the degrees of freedom

of the calculation. For that reason, a variety of different spray flamelets for various droplets' boundary conditions need to be taken into account.

1.6. Outline

Chapter 2 introduces the theory about all the fundamental aspects that are related to the fluid motion, the combustion and how the one interacts with the other. An analysis about the liquid phase follows in which the dispersion and the evaporation models of the droplets are described. In the following section the characteristics of turbulence and the different approaches on how to resolve it are analyzed from a numerical analysis point of view. Finally, the difficulties that exist regarding the closure of the chemical source terms in the filtered/averaged transport equations give the space for the introduction of the flamelet-based methods.

Chapter 3 presents the working procedure that is followed in this thesis in order to achieve the final results. This includes the description of the solvers that are used and the basic steps that need to be followed in order to accomplish a single simulation in the programming environment of OpenFOAM. Also, the boundary conditions for all the cases considered in this thesis are given and the procedure needed to post-process the results is described.

Chapter 4 shows the final results that were obtained from the simulations. Firstly, the solver and the set-up of a case is validated using as a reference the CHEM1D code [11]. Following, the results for the gaseous and spray flamelets are presented and discussed highlighting the main differences that come out.

Chapter 5 summarizes the conclusions that were derived during the calculations and proposes certain recommendations to be studied in a future work.

2

Theory

2.1. Fluid flow and Combustion

The topic of the current project concerns the spray combustion, and so the medium of interest can be either the liquid or the gas phase, then in a general way of speaking the medium can be called fluid in the following paragraphs. The conceptual study of combustion involves the theoretical multidisciplinary understanding of different aspects such as fluid mechanics, chemistry and thermodynamics.

In order to understand the above mentioned topics one should have a good feeling about four very commonly used variables that characterize the flow field and its properties at any instant: pressure, density, temperature and flow velocity.

If we conceptually think of a free surface immersed on a fluid, ***pressure*** is the normal force per unit area exerted on that surface due to the momentum of the fluid molecules impacting on that surface. Similarly, to define ***density*** we can say that it is the ratio of mass divided by the unit of volume. In addition, ***temperature*** is a property directly related and proportional to the average kinetic energy of the molecules of the fluid. Finally, we can define an infinitesimal small element of mass in the fluid, called fluid element and both its speed and direction can vary as it moves in space. Then, the ***flow velocity*** can be seen as the velocity of the fluid element as it passes through a fixed point in space at a specific time moment. According to the description of these four variables we state that pressure, temperature, density and flow velocity are point variables and can vary from point to point in the fluid [1].

2.2. Types of Flow

In order to understand the physical phenomena underlying combustion, one needs to have a clue about the distinction of the different types of flows [1] as shown in Figure 2.1.

In general, for the specific fluid dynamics problem of interest (e.g. combustion, aerodynamics etc.) we can assign a characteristic length (L) respective to the geometry of the problem and a mean-free path λ defined as the mean distance that a molecule travels between collisions with neighbouring molecules. If the mean-free path λ is of the same order of magnitude as the characteristic length L then the type of flow of the problem falls under the category of

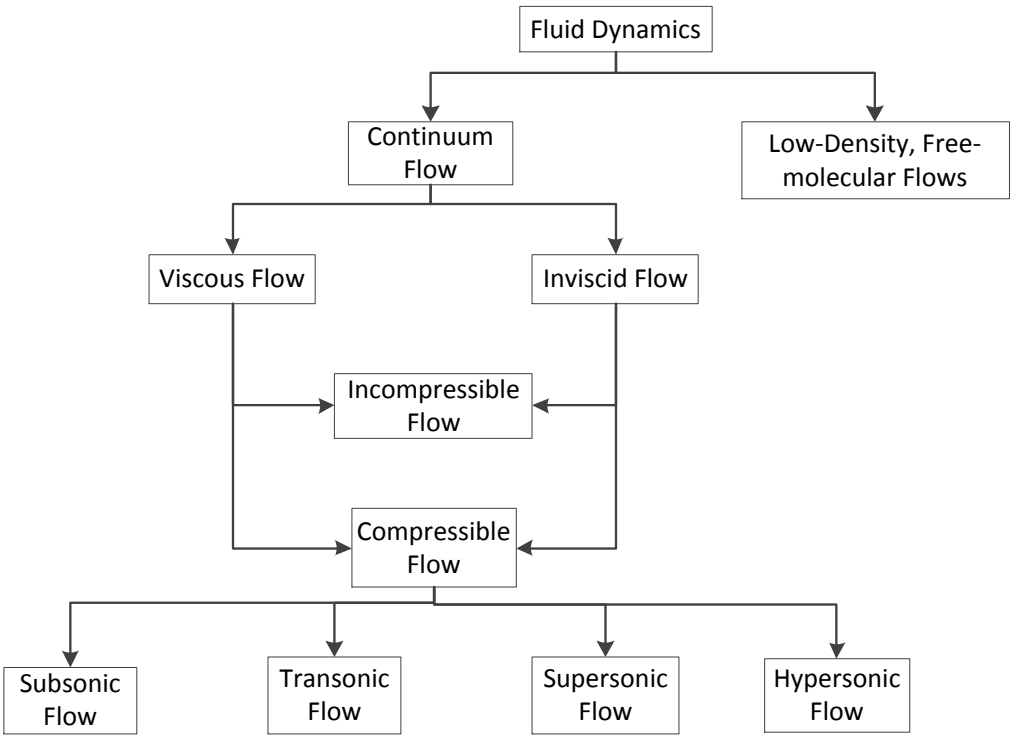

Figure 2.1: Diagram showing the types of flows [1]

Free-molecular flows and two consequent molecules passing through a certain point of the domain present a totally different impact and as a result one has to address to molecular statistics in order to deal with these kind of flows. On the other hand if $\lambda << L$, then the flow resembles a continuous medium and we call these flows ***Continuum flows***. For continuum flows one has to resolve the analytical equations that are produced from physical laws (as will be described in the following sections) for continuous medium. Free-molecular flows can become significant in regions of very low pressure or very small size (molecular level), so for our case of the spray combustion we will focus exclusively to continuum flows.

At a molecular scale, when the molecules move from one point to another and possibly interact, obviously they transfer their mass, momentum and energy. This molecular transport gives rise to viscous (molecular transport) phenomena such as mass diffusion, viscosity (friction), and thermal conduction. If the influence of these molecular transport phenomena is significant to the physics of the problem of interest then this flow is called as ***viscous flow***, while if it is orders of magnitude lower than the advection effects it can be omitted and the flow is called as ***inviscid flow***. Usually in a complex problem, it is profitable to apply the aspects of viscous flows inside the boundary layer where the gradients of velocity, temperature and concentration can be significant, while far away from the boundary layer where advection (free stream flow) dominates, the aspects of a inviscid flows can be used simplifying so the continuum equations and reducing the computational cost.

An important distinction between the flows can be made regarding whether or not the density of a flow remains constant across the domain. According to [12], the ***compressibility*** can be defined as *the ability for changes in volume of a fixed mass of fluid*. When a fixed mass of a fluid undergoes changes in volume, its density also changes. Thus the capacity for changes in the density of a mass element of a fluid is also known as compressibility. And similarly, an ***incompressible fluid*** *is one whose elements undergo no change in volume or density*. The main causes for changes in the volume of a fluid are pressure, stresses and the non-uniform heating of the fluid. As it will be shown later, for an incompressible flow, the physics are simpler, and the primary independent variables to be resolved are pressure and velocity and as a result the solution of the mass conservation equation and of momentum equation are sufficient to solve the problem. However, for combustion we expect that due to chemical heat release, the density across a pathline of a fluid element will not remain constant and as a result the nature of the flow is characterised as compressible. Thus, for a compressible flow, density is an additional variable and therefore we need to solve also the energy equation. The energy equation in turn is linked with temperature and for that reason the equation of state also need to be considered in order to close the system.

The last distinction regarding compressible flows, as shown in Figure 2.1 is based on the Mach (M) number, defined as the ratio of the local velocity of the fluid divided by the local speed of sound and we observe the following flow regimes:

- ***Subsonic flow*** is the type of flow where $M < 1$, especially when $M < 0.3$ the compressibility effects due to local fluid field are reduced and the flow can be seen as incompressible.
- ***Transonic flow***, is a transition region where the flow is almost sonic (M=1) and the local Mach number may take values less than 1 or higher than 1.
- ***Supersonic flow*** is the type of flow where $M > 1$ everywhere and is characterized by the the presence of shock waves across which the flow properties change discontinuously (in contrast to the smooth variations in subsonic flows).
- ***Hypersonic flow*** refers to very high supersonic speeds ($M >> 1$). In that region the shock waves become stronger and come closer to the body surface (shock layer) interacting with the viscous boundary layer and leading to local temperature peaks.

In the current report we focus only on subsonic flows. For more details on the distinction and the characteristics of the acoustic flows, one may refer to [1]. To finalize the characterization of a flow dynamics problem one last distinction should be done at this stage. And this distinction arises depending on whether the flow is laminar or turbulent. Very shortly, we can define:

- ***Laminar flow***, in which the streamlines are smooth and regular and a fluid element moves smoothly along a streamline.
- ***Turbulent flow***, in which the streamlines become irregular and chaotic and a fluid element moves in a random, irregular and tortuous fashion. Schlichting in his boundary layer theory [13] defines turbulence as *a motion in which an irregular fluctuation (mixing or eddying motion) is superimposed on the main stream*.

Turbulence calculations are not in the scope of this project, so the mode of the spray combustion is laminar. Addressing the distinctions for all the types of flows and the reasons mentioned

already to the physics of the current project, we can characterize the flow of the current spray combustion project as continuous, viscous, compressible, subsonic and laminar.

2.3. Specification of Flow field

The calculation of spray flamelets dictates the need of knowledge of the flow properties for each and every point of the domain. The main flow properties that need specification are pressure (p), density (ρ), temperature (T) and velocity (V) [1]. For our special case where the dominating phenomena are the evaporation of the spray and the subsequent chemical reactions we also need to have information regarding the distribution of the different chemical species over the domain and the best way to do so is by calculating the species mass fractions (Y_k), which is defined at a local point as the mass of the *-kth* species divided by the total mass of the gas. Thus, we can say that the equations

$$p = p(x, y, z, t) \tag{2.1}$$

$$\rho = \rho(x, y, z, t) \tag{2.2}$$

$$T = T(x, y, z, t) \tag{2.3}$$

$$V = ui + vj + wk \tag{2.4}$$

where,

$$u = u(x, y, z, t) \tag{2.4.a}$$

$$v = v(x, y, z, t) \tag{2.4.b}$$

$$w = w(x, y, z, t) \tag{2.4.c}$$

are the scalar components of the vector velocity V, and

$$Y_k = Y_k(x, y, z, t) \tag{2.5}$$

represent the flow field. The equations are written for the general case where the flow is three dimensional and unsteady.

2.4. Governing Equations

Now, in order to get the information for those flow properties (Equations 2.1 to 2.5) for a compressible flow, one has to resolve the continuity equation, the momentum equation, the energy equation, the equation of state and the transport mass fraction equation. In the following sections the derivation for those sections is described based on the approach followed in [1].

2.4.1. Continuity Equation

Initially, we may consider a fixed finite control volume (Figure 2.2) in space with the flow passing through it. Its volume and surface is constant with time, while the mass of fluid contained in this volume can change with time due to unsteady fluctuations.

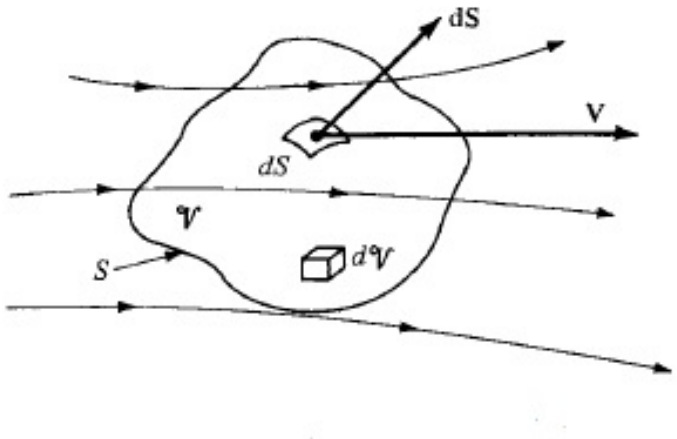

Figure 2.2: Fixed control volume in space [1]

In Figure 2.2 are indicated the surface area S and the volume $\mathcal{V}$. Also, locally we can define an elemental surface area dS with a normal vector to it as $d\mathcal{S}$, which always points in a direction out of the control volume and its magnitude equals the magnitude of the elemental surface area dS. Moreover, we define an elemental control volume $d\mathcal{V}$ and at a certain point on the control surface we can point the flow velocity V. To clarify, from the above mentioned quantities $\mathcal{V}$, S, $d\mathcal{V}$, dS are scalars, while $d\mathcal{S}$ and V are vectors.

To this control volume we can now apply the famous principle that *mass can be neither destroyed nor created*. In other words we can say for this control volume that:

The net mass flow out of the control volume through surface S equals the time rate of decrease of mass inside the control volume $\mathcal{V}$.

If we interpret this last statement into a mathematical expression, we can say that an elemental mass flow across the surface area dS can be given by:

$$\rho V \cdot d\mathcal{S} \tag{2.6}$$

Note here that the velocity vector V is at an arbitrary direction as shown in the Figure 2.2 and $d\mathcal{S}$ is a vector normal to the elemental surface area dS. Thus, the dot product $(V \cdot d\mathcal{S})$ is a scalar and gives the volumetric flow normal to the elemental surface area dS. Also note that $d\mathcal{S}$ always points out of the control volume and if V also points out then the expression (2.6) is positive and gives an outflow (mass flow leaves the control volume). Contrary, if V points in the control volume the expression (2.6) becomes negative and we have an inflow (mass flow enters the control volume).

If we integrate the expression (2.6) for the whole control volume $\mathcal{V}$ over its surface S we get

a surface integral (2.7) which represents the summation of the elemental mass flows over the surface S and equals the net mass flow out of the entire control surface S.

$$\oiint_S \rho V \cdot d\mathcal{S} \tag{2.7}$$

According to the physical principle we stated for the control volume this last expression (2.7) should necessarily equal the time rate of decrease of the mass inside the control volume, which mathematically can be written as:

$$-\frac{\partial}{\partial t} \oiiint_{\mathcal{V}} \rho d\mathcal{V} \tag{2.8}$$

In (2.8), the product $(\rho d\mathcal{V})$ declares the mass enclosed inside the elemental volume $d\mathcal{V}$, the triple integral declares the calculation of the total mass enclosed in the whole closed control volume $\mathcal{V}$, the time derivative defines the time rate of change of the mass inside the volume $\mathcal{V}$ and the negative sign stands for the decrease of the mass inside the volume $\mathcal{V}$.

Equalizing the expressions (2.7) and (2.8) we conclude to the first fundamental equation the so-called continuity equation:

$$\frac{\partial}{\partial t} \oiiint_{\mathcal{V}} \rho d\mathcal{V} + \oiint_S \rho V \cdot d\mathcal{S} = 0 \tag{2.9}$$

The equation (2.9) is substantially the application of the conservation of mass over a control volume fixed in space.

This integral form of the continuity equation gives information for a finite region in space. However, in our case it is more practical to attain information for every single point of the flow, so we need to convert equation (2.9) into a differential form as a final step.

In equation (2.9) the time derivative can enter the volume integral since the volume is fixed, and also we can apply the divergence theorem in the surface integral, obtaining the expression:

$$\oiiint_{\mathcal{V}} \frac{\partial \rho}{\partial t} d\mathcal{V} + \oiiint_{\mathcal{V}} \nabla \cdot (\rho V) d\mathcal{V} = 0 \tag{2.10}$$

or

$$\oiiint_{\mathcal{V}} \left[\frac{\partial \rho}{\partial t} + \nabla \cdot (\rho V) \right] d\mathcal{V} = 0 \tag{2.11}$$

From equation (2.11) we can see that the integral gives always a zero value as result. This means that the integrand should be a constant value. If it is a finite number (other than zero), then this would require that the integral over part of the control volume would be equal and opposite to the integral over the rest of the control volume, so that the total integration over the whole control volume would be zero as equation (2.11) demands. However, since the choice of the control volume in space was arbitrarily made, we can consider an infinitesimal small control volume for which by definition there is no substructure and no cancellation of

one region from the other and as a result the integrand should be zero for any infinitesimal volume, leading us to :

$$\frac{\partial \rho}{\partial t} + \nabla \cdot (\rho V) = 0 \tag{2.12}$$

Equation (2.12) is the continuity equation in a partial differential form which can be applied at any point of the flow.

2.4.2. Momentum Equation

At this section the second fundamental equation, the momentum equation, which gives information about the flow field will be developed. Also in that case the derivation of that equation is based on a physical principle. This principle is generated by Newton's second law which states that *the net force applied in a body equals the product of its mass and its acceleration*:

$$F = ma \tag{2.13}$$

Equation (2.13) is a vector equation and in three dimensional cartesian coordinates it has three components. For convenience we can analyse the x-component (2.14) and the other two can be produced similarly. Thus the x-component is:

$$F_x = ma_x \tag{2.14}$$

In (2.14), F_x is the net of the body and surface forces that are exerted in a fluid element of fixed mass in the x direction. Let as denote as f_x the net body force in the x direction acting on the fluid element per unit mass. However, more correctly for the case of multi-component mixtures where a distinction between the different species can be done, the net body force per unit mass should be given as the sum of the body forces applied on each and every species in the volume of the fluid element [14]. Thus, the net body force per unit mass can be written as $\sum_{k=1}^{N} Y_k f_{k,x}$, where in a mixture of N species $f_{k,x}$ is the body (volume) force acting on species k and Y_k is the mass fraction of species k in the mixture inside the fluid element. The sum of the surface forces (pressure and viscous stresses) acting on a moving fluid element in the x direction are shown in Figure 2.3.

Summing all the forces together we obtain F_x as:

$$F_x = \left(-\frac{\partial p}{\partial x} + \frac{\partial \tau_{xx}}{\partial x} + \frac{\partial \tau_{yx}}{\partial y} + \frac{\partial \tau_{zx}}{\partial z} + \rho \sum_{k=1}^{N} Y_k f_{k,x} \right) dxdydz \tag{2.15}$$

The mass of the fluid element is fixed an can be noted as:

$$m = \rho dxdydz \tag{2.16}$$

If we follow this fluid element in space, its time rate of change of velocity is not only because of the pass of time but also due to passing from one point to another (where the flow characteristics are different) at this time interval. Thus the fluid element's acceleration in the x direction should be given by the material derivative as :

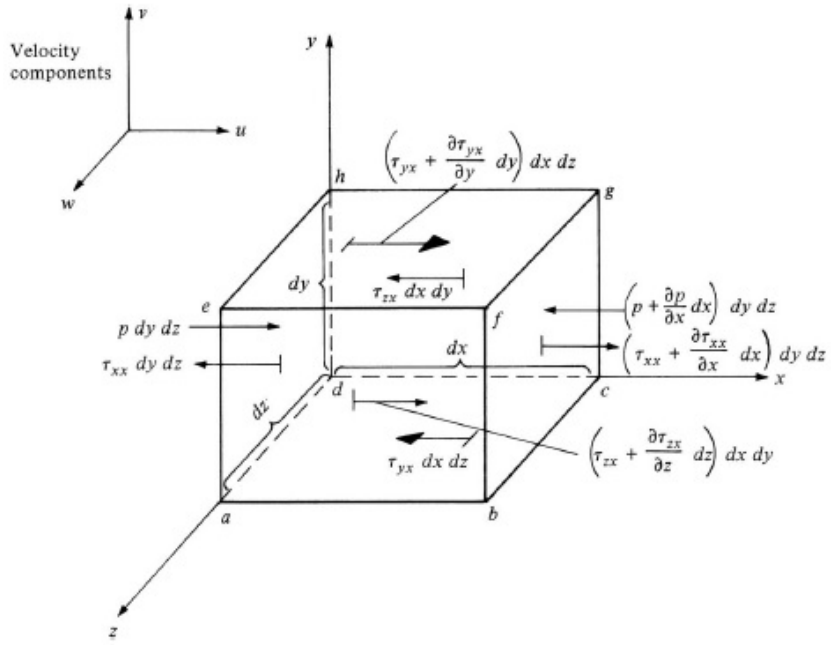

Figure 2.3: Surface forces in the x direction of a fluid element of fixed mass [1]

$$a_x = \frac{Du}{Dt} \tag{2.17}$$

Combining the equations (2.15), (2.16) and (2.17) into (2.14) we obtain the momentum equation in the x direction as:

$$\rho \frac{Du}{Dt} = -\frac{\partial p}{\partial x} + \frac{\partial \tau_{xx}}{\partial x} + \frac{\partial \tau_{yx}}{\partial y} + \frac{\partial \tau_{zx}}{\partial z} + \rho \sum_{k=1}^{N} Y_k f_{k,x} \tag{2.18}$$

Recalling the definition of material derivative and the relations of viscous stresses for Newtonian fluid:

$$\frac{D}{Dt} = \frac{\partial}{\partial t} + (V \cdot \nabla) \tag{2.19}$$

$$\tau_{xx} = \lambda \nabla \cdot V + 2\mu \frac{\partial u}{\partial x} \tag{2.20}$$

$$\tau_{yx} = \mu \left(\frac{\partial v}{\partial x} + \frac{\partial u}{\partial y} \right) \tag{2.21}$$

$$\tau_{zx} = \mu \left(\frac{\partial w}{\partial x} + \frac{\partial u}{\partial z} \right) \tag{2.22}$$

where λ is the bulk viscosity and to very good approximation equals $-2/3\mu$ [1]. We can obtain the analytical momentum equation in the x direction as:

$$\rho\left(\frac{\partial u}{\partial t}+u\frac{\partial u}{\partial x}+v\frac{\partial u}{\partial y}+w\frac{\partial u}{\partial z}\right)=-\frac{\partial p}{\partial x}+\frac{\partial}{\partial x}\left[\lambda\nabla\cdot V+2\mu\frac{\partial u}{\partial x}\right]+\frac{\partial}{\partial y}\left[\mu\left(\frac{\partial v}{\partial x}+\frac{\partial u}{\partial y}\right)\right]+\frac{\partial}{\partial z}\left[\mu\left(\frac{\partial w}{\partial x}+\frac{\partial u}{\partial z}\right)\right]+\rho\sum_{k=1}^{N}Y_k f_{k,x} \tag{2.23}$$

similarly for the y direction we obtain:

$$\rho\frac{Dv}{Dt}=-\frac{\partial p}{\partial y}+\frac{\partial\tau_{xy}}{\partial x}+\frac{\partial\tau_{yy}}{\partial y}+\frac{\partial\tau_{zy}}{\partial z}+\rho\sum_{k=1}^{N}Y_k f_{k,y} \tag{2.24}$$

$$\rho\left(\frac{\partial v}{\partial t}+u\frac{\partial v}{\partial x}+v\frac{\partial v}{\partial y}+w\frac{\partial v}{\partial z}\right)=-\frac{\partial p}{\partial y}+\frac{\partial}{\partial y}\left[\lambda\nabla\cdot V+2\mu\frac{\partial v}{\partial y}\right]+\frac{\partial}{\partial x}\left[\mu\left(\frac{\partial u}{\partial y}+\frac{\partial v}{\partial x}\right)\right]+\frac{\partial}{\partial z}\left[\mu\left(\frac{\partial w}{\partial y}+\frac{\partial v}{\partial z}\right)\right]+\rho\sum_{k=1}^{N}Y_k f_{k,y} \tag{2.25}$$

and for the z direction we obtain:

$$\rho\frac{Dw}{Dt}=-\frac{\partial p}{\partial z}+\frac{\partial\tau_{xz}}{\partial x}+\frac{\partial\tau_{yz}}{\partial y}+\frac{\partial\tau_{zz}}{\partial z}+\rho\sum_{k=1}^{N}Y_k f_{k,z} \tag{2.26}$$

$$\rho\left(\frac{\partial w}{\partial t}+u\frac{\partial w}{\partial x}+v\frac{\partial w}{\partial y}+w\frac{\partial w}{\partial z}\right)=-\frac{\partial p}{\partial z}+\frac{\partial}{\partial z}\left[\lambda\nabla\cdot V+2\mu\frac{\partial w}{\partial z}\right]+\frac{\partial}{\partial x}\left[\mu\left(\frac{\partial u}{\partial z}+\frac{\partial w}{\partial x}\right)\right]+\frac{\partial}{\partial y}\left[\mu\left(\frac{\partial v}{\partial z}+\frac{\partial w}{\partial z}\right)\right]+\rho\sum_{k=1}^{N}Y_k f_{k,z} \tag{2.27}$$

2.4.3. Energy Equation

As already has been discussed, combustion links to compressible flows where apart from the calculation of pressure (p) and velocity (V) (using the tools of continuity and momentum equations) one has to solve also for the density (ρ), which depends on temperature pressure and composition, and as a result more equations are needed to close the system. Thus, at this section we will develop the third fundamental equation which is the energy equation and is based on the physical principle which states that *energy can be neither destroyed nor created, it can only change in form*.

For a fluid element of fixed mass moving in space as it is shown in Figure 2.3 we can apply the first thermodynamic law saying that the rate of change of energy inside the fluid element equals the net flux of heat into the fluid element plus the rate of work done on the element's surface by the surface forces (pressure and stresses forces) plus the work done in the volume of the fluid element by the body forces.

First let us consider the work done by the body and surface forces in the fluid element. When talking about the rate of work we literally refer to the power which has units of J/s or Watt. Thus, in a general way we can write the work rate of a force exerted in a body (or surface) as the product of that force multiplied by the body's velocity ($F \cdot V$).

Regarding the work rate of the body forces, as it is already mentioned for multi-component mixtures, it can be discretized for each and every species. So we can write for the three directions:

$$\begin{aligned} &\sum_{k=1}^{N} Y_k f_{k,x}(u + \mathrm{u}_k) \\ &\sum_{k=1}^{N} Y_k f_{k,y}(v + \mathrm{v}_k) \\ &\sum_{k=1}^{N} Y_k f_{k,w}(w + \mathrm{w}_k) \end{aligned} \tag{2.28}$$

where for the x,y,z directions we have respectively the body forces per unit mass $f_{k,x}$, $f_{k,y}$, $f_{k,z}$, the flow velocity scalar components u, v, w of the vector V and the diffusion velocity scalar components of species-k u, v, w of the vector V [14].

In Figure 2.4 the work rate of the forces acting on the surface of a fluid element in the x direction of a three dimensional cartesian system are shown. Similarly, the corresponding terms for the other two directions can be deduced.

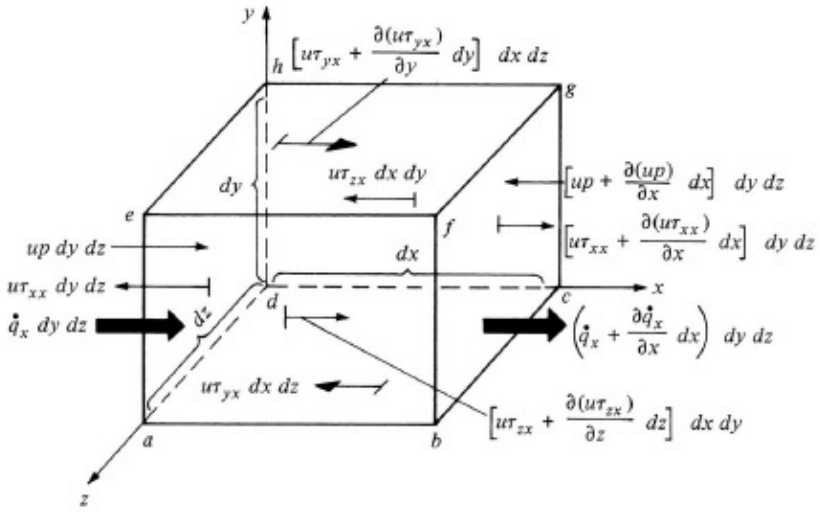

Figure 2.4: Energy fluxes in the x direction of a fluid element of fixed mass [1]

Summing all the work rates shown in Figure 2.4 and adding to them the work rate done by the body forces in the x direction we get:

$$\left[-\frac{\partial(up)}{\partial x}+\frac{\partial(u\tau_{xx})}{\partial x}+\frac{\partial(u\tau_{xy})}{\partial y}+\frac{\partial(u\tau_{xz})}{\partial z}+\rho\sum_{k=1}^{N}Y_k f_{k,x}(u+\mathrm{u}_k)\right]dxdydz \tag{2.29}$$

If in equation (2.29) we also include the corresponding terms for the other two directions y and z we get the more general form:

$$\begin{aligned}\text{Work rate of forces} = \Bigg[&-\frac{\partial(up)}{\partial x}+\frac{\partial(u\tau_{xx})}{\partial x}+\frac{\partial(u\tau_{yx})}{\partial y}+\frac{\partial(u\tau_{zx})}{\partial z}+\rho\sum_{k=1}^{N}Y_k f_{k,x}(u+\mathrm{u}_k)\\ &-\frac{\partial(vp)}{\partial y}+\frac{\partial(v\tau_{xy})}{\partial x}+\frac{\partial(v\tau_{yy})}{\partial y}+\frac{\partial(v\tau_{zy})}{\partial z}+\rho\sum_{k=1}^{N}Y_k f_{k,y}(v+\mathrm{v}_k)\\ &-\frac{\partial(wp)}{\partial z}+\frac{\partial(w\tau_{xz})}{\partial x}+\frac{\partial(w\tau_{yz})}{\partial y}+\frac{\partial(w\tau_{zz})}{\partial z}+\rho\sum_{k=1}^{N}Y_k f_{k,w}(w+\mathrm{w}_k)\Bigg]dxdydz\end{aligned} \tag{2.30}$$

Then we can consider the heat addition to the fluid element. Two sources are responsible for this heat flux: a) the volumetric heating of the fluid element due to radiation, electric spark, laser etc. and b) the heat transfer across the surface due to thermal conduction and due to mass diffusion of species with different enthalpies which is a characteristic of multi-component fluid flows. We can define as $\dot{q}_v$ the rate of volumetric heat per unit mass and by using the equation (2.16) for the mass of the element we can identify the volumetric heating as:

$$\text{Volumetric heating} = \rho\dot{q}_v dxdydz \tag{2.31}$$

The surface heat fluxes of the fluid element are also shown in the Figure 2.4 and summing them all together along the x direction we find the following expression:

$$-\frac{\partial\dot{q}_x}{\partial x}dxdydz \tag{2.32}$$

Adding similarly the contributions of the y and z directions we obtain:

$$-\left[\frac{\partial\dot{q}_x}{\partial x}+\frac{\partial\dot{q}_y}{\partial y}+\frac{\partial\dot{q}_z}{\partial z}\right]dxdydz \tag{2.33}$$

The surface heat fluxes that were simply denoted as $\dot{q}_x, \dot{q}_y, \dot{q}_z$, $(J/m^2 s)$ contain the contribution of thermal conduction and mass diffusion as already mentioned. The thermal conduction contribution term can be described by the Fourier's law $(-k\frac{\partial T}{\partial x_i})$. And the mass diffusion term is associated with the diffusion of species with different enthalpies which is a characteristic of multi-component mixtures. Thus, we can write an expression for $\dot{q}_x, \dot{q}_y, \dot{q}_z$ as:

$$\dot{q}_x = -k\frac{\partial T}{\partial x} + \rho \sum_{k=1}^{N} h_k Y_k \mathrm{u}_k$$
$$\dot{q}_y = -k\frac{\partial T}{\partial y} + \rho \sum_{k=1}^{N} h_k Y_k \mathrm{v}_k \tag{2.34}$$
$$\dot{q}_z = -k\frac{\partial T}{\partial z} + \rho \sum_{k=1}^{N} h_k Y_k \mathrm{w}_k$$

where h_k, Y_k are the enthalpy, mass fraction of the species k respectively and u_k, v_k, w_k are the scalar components of the diffusion vector velocity V_k of species k [14]. The three scalar components $\dot{q}_x, \dot{q}_y, \dot{q}_z$ consist a surface heat flux vector written as:

$$\dot{q} = \dot{q}_x i + \dot{q}_y j + \dot{q}_z k = -k\nabla T + \rho \sum_{k=1}^{N} h_k Y_k \mathrm{V}_k \tag{2.35}$$

Now putting all the heat fluxes together by combining the equations (2.31) and (2.33) we obtain:

$$\text{Net heat flux} = \left[\rho \dot{q}_v - \frac{\partial \dot{q}_x}{\partial x} - \frac{\partial \dot{q}_y}{\partial y} - \frac{\partial \dot{q}_z}{\partial z}\right] dxdydz = \left[\rho \dot{q}_v - \nabla \cdot \dot{q}\right] dxdydz \tag{2.36}$$

The equations (2.30) and (2.36) give the expressions for the work rate and the heat flux applied in a fluid element. As it is already discussed due to the first thermodynamic law the sum of those two expressions should be equal to the time rate of change of energy inside the fluid element. Since this fluid element is moving continuously with the local flow velocity V, it has a consequent kinetic energy per unit mass $V^2/2$. Thus, its total energy per unit mass should be the sum of its internal energy plus its kinetic energy, $e + V^2/2$.

If we follow this fluid element in space, its time rate of change of energy is not only because of the pass of time but also due to passing from one point to another (where the flow characteristics are different) at this time interval. Thus the fluid element's rate of energy should be given by the material derivative as:

$$\rho \frac{D}{Dt}\left(e + \frac{V^2}{2}\right) dxdydz \tag{2.37}$$

Now we are in a position to express the energy equation by combining the equations (2.37), (2.36) and (2.30):

$$\begin{aligned}
\rho\frac{D}{Dt}\left(e+\frac{V^2}{2}\right) &= \rho\dot{q}_v - \frac{\partial\dot{q}_x}{\partial x} - \frac{\partial\dot{q}_y}{\partial y} - \frac{\partial\dot{q}_z}{\partial z} \\
-\frac{\partial(up)}{\partial x} + \frac{\partial(u\tau_{xx})}{\partial x} + \frac{\partial(u\tau_{yx})}{\partial y} + \frac{\partial(u\tau_{zx})}{\partial z} &+ \rho\sum_{k=1}^{N} Y_k f_{k,x}(u+\mathrm{u}_k) \\
-\frac{\partial(vp)}{\partial y} + \frac{\partial(v\tau_{xy})}{\partial x} + \frac{\partial(v\tau_{yy})}{\partial y} + \frac{\partial(v\tau_{zy})}{\partial z} &+ \rho\sum_{k=1}^{N} Y_k f_{k,y}(v+\mathrm{v}_k) \\
-\frac{\partial(wp)}{\partial z} + \frac{\partial(w\tau_{xz})}{\partial x} + \frac{\partial(w\tau_{yz})}{\partial y} + \frac{\partial(w\tau_{zz})}{\partial z} &+ \rho\sum_{k=1}^{N} Y_k f_{k,w}(w+\mathrm{w}_k)
\end{aligned} \tag{2.38}$$

An alternative form for energy equation can be derived in terms of enthalpy (h), recalling that $h = e + p/\rho$. Then we can develop an expression for $\rho\frac{D}{Dt}(p/\rho)$ as:

$$\rho\frac{D}{Dt}(p/\rho) = \rho\frac{\frac{Dp}{Dt} - p\frac{D\rho}{Dt}}{\rho^2} = \frac{Dp}{Dt} - \frac{p}{\rho}\frac{D\rho}{Dt} = \frac{\partial p}{\partial t} + V\cdot\nabla p + p\nabla\cdot V = \frac{\partial p}{\partial t} + \nabla\cdot(pV) \tag{2.39}$$

Note that in equation (2.38) the pressure terms can be rewritten as:

$$-\frac{\partial(up)}{\partial x} - \frac{\partial(vp)}{\partial y} - \frac{\partial(wp)}{\partial z} = -\nabla\cdot(pV) \tag{2.40}$$

Then by adding equation (2.39) into (2.38) we obtain:

$$\begin{aligned}
\rho\frac{D}{Dt}\left(h+\frac{V^2}{2}\right) &= \frac{\partial p}{\partial t} + \rho\dot{q}_v - \frac{\partial\dot{q}_x}{\partial x} - \frac{\partial\dot{q}_y}{\partial y} - \frac{\partial\dot{q}_z}{\partial z} \\
+\frac{\partial(u\tau_{xx})}{\partial x} + \frac{\partial(u\tau_{yx})}{\partial y} + \frac{\partial(u\tau_{zx})}{\partial z} &+ \rho\sum_{k=1}^{N} Y_k f_{k,x}(u+\mathrm{u}_k) \\
+\frac{\partial(v\tau_{xy})}{\partial x} + \frac{\partial(v\tau_{yy})}{\partial y} + \frac{\partial(v\tau_{zy})}{\partial z} &+ \rho\sum_{k=1}^{N} Y_k f_{k,y}(v+\mathrm{v}_k) \\
+\frac{\partial(w\tau_{xz})}{\partial x} + \frac{\partial(w\tau_{yz})}{\partial y} + \frac{\partial(w\tau_{zz})}{\partial z} &+ \rho\sum_{k=1}^{N} Y_k f_{k,w}(w+\mathrm{w}_k)
\end{aligned} \tag{2.41}$$

We notice that the term $\rho\frac{D}{Dt}\left(\frac{V^2}{2}\right)$ in the left hand side of equation (2.41) is equal to the momentum equation multiplied by V. We can show this by multiplying by u, v, w the respective momentum equations (2.18), (2.24), (2.26) and we get:

$$\rho u\frac{Du}{Dt}=\rho\frac{D}{Dt}\left(\frac{1}{2}u^2\right)=-u\frac{\partial p}{\partial x}+u\frac{\partial \tau_{xx}}{\partial x}+u\frac{\partial \tau_{yx}}{\partial y}+u\frac{\partial \tau_{zx}}{\partial z}+u\rho\sum_{k=1}^{N}Y_k f_{k,x}$$
$$\rho v\frac{Dv}{Dt}=\rho\frac{D}{Dt}\left(\frac{1}{2}v^2\right)=-v\frac{\partial p}{\partial y}+v\frac{\partial \tau_{xy}}{\partial x}+v\frac{\partial \tau_{yy}}{\partial y}+v\frac{\partial \tau_{zy}}{\partial z}+v\rho\sum_{k=1}^{N}Y_k f_{k,y} \quad (2.42)$$
$$\rho w\frac{Dw}{Dt}=\rho\frac{D}{Dt}\left(\frac{1}{2}w^2\right)=-w\frac{\partial p}{\partial z}+w\frac{\partial \tau_{xz}}{\partial x}+w\frac{\partial \tau_{yz}}{\partial y}+w\frac{\partial \tau_{zz}}{\partial z}+w\rho\sum_{k=1}^{N}Y_k f_{k,z}$$

Then we can subtract equation (2.42) from (2.41) to obtain:

$$\rho\frac{Dh}{Dt}=\frac{Dp}{Dt}+\rho\dot{q}_v-\frac{\partial \dot{q}_x}{\partial x}-\frac{\partial \dot{q}_y}{\partial y}-\frac{\partial \dot{q}_z}{\partial z}+\tau_{xx}\frac{\partial u}{\partial x}+\tau_{yx}\frac{\partial u}{\partial y}+\tau_{zx}\frac{\partial u}{\partial z}+\rho\sum_{k=1}^{N}Y_k f_{k,x}\mathrm{u}_k$$
$$+\tau_{xy}\frac{\partial v}{\partial x}+\tau_{yy}\frac{\partial v}{\partial y}+\tau_{zy}\frac{\partial v}{\partial z}+\rho\sum_{k=1}^{N}Y_k f_{k,y}\mathrm{v}_k \quad (2.43)$$
$$+\tau_{xz}\frac{\partial w}{\partial x}+\tau_{yz}\frac{\partial w}{\partial y}+\tau_{zz}\frac{\partial w}{\partial z}+\rho\sum_{k=1}^{N}Y_k f_{k,w}\mathrm{w}_k$$

We can say that equation (2.43) is the energy equation and the third fundamental equation after continuity and momentum equation and can be used for compressible flows to calculate the variable density. However, equation (2.43) introduces a new flow variable the enthalpy. Thus, we have the three fundamental equations which involve four variables to be calculated: p, V, ρ, h.

We should mention here that the enthalpy (h) corresponds to the sum of the sensible and chemical enthalpy. If we make the assumption that the fluid behaves as a perfect gas, then the sensible enthalpy can be seen as a function of temperature only $h_s = h_s(T)$. And in differential form can be written as $dh_s = C_p dT$, where C_p is the specific heat at constant pressure and it is also a function of temperature. The integration of sensible enthalpy can be easily done by using empirical polynomial relations for the specific heat. For the enthalpy (h) we can write:

$$h = h_s + h_{chem} = \int_{T_o}^{T} C_p dT + \sum_{k=1}^{N}\Delta h^o_{f,k} Y_k \quad (2.44)$$

where $\Delta h^o_{f,k}$ is the enthalpy of formation, meaning the enthalpy needed to form 1 Kg of species k at the reference temperature 298.15 K.

As a result we see that the calculation of enthalpy introduces another variable, the temperature T. Finally, we can make use of the perfect gas equation (2.45) to calculate the temperature and close the system of equations.

$$p = \rho R T \tag{2.45}$$

where R is the specific gas constant.

2.4.4. Mass Fraction Equation

For one component fluids in compressible flows the equations presented so far should be sufficient to solve the flow field (p, ρ, V, T). However, since our topic is focused specifically on spray combustion, the evaporation and the chemical reactions that take place involve the consumption or the production of chemical species. As a result the fluid that is under consideration is consisted of numerous components (chemical species) and its composition changes continuously. And since we want to study the different mechanisms under which pollutants and emissions of products are created, the specification of the flow field needs to have information about the chemical species distribution in the flow. To do so, in this section we derive the transport equation for the mass fractions of the species.

If we see this multi-component fluid flow as the superposition of the flows of the different chemical species that is consisted of, then for any single species k we can write the mass conservation principle as it passes through a control volume like the one presented in Figure 2.2 as:

The time rate of decrease of the mass of species k inside the control volume $\mathcal{V}$ equals the net mass flow of species k out of the control volume through surface S due to advection and diffusion plus the rate of consumption of species k due to a chemical process inside the control volume $\mathcal{V}$.

From a mathematical point of view this principle can be written as:

$$-\frac{\partial}{\partial t}\oiiint_{\mathcal{V}} \rho_k d\mathcal{V} = \oiint_{S} \rho_k (V + \mathrm{V}_k)\cdot d\mathcal{S} - \oiiint_{\mathcal{V}} \dot{\omega}_k d\mathcal{V} \tag{2.46}$$

where ρ_k is the density of species k, $\dot{\omega}_k$ is the rate of production of mass of species k per unit volume and so the negative sign in front of it declares consumption and V_k is the vector diffusion velocity of species k.

For the reasons explained in the derivation of the continuity equation, the integral form of equation (2.46) for a control volume can be equivalently rewritten in a differential form for any point in space as:

$$\begin{gathered}\frac{\partial \rho Y_k}{\partial t} + \nabla\cdot\left[\rho\left(V + \mathrm{V}_k\right) Y_k\right] = \dot{\omega}_k, \quad k = 1, N \\ \text{or} \\ \frac{\partial \rho Y_k}{\partial t} + \nabla\cdot\left(\rho V Y_k\right) = -\nabla\cdot\left(\rho \mathrm{V}_k Y_k\right) + \dot{\omega}_k\end{gathered} \tag{2.47}$$

where the formula $\rho_k = \rho Y_k$ is used and Y_k is the mass fraction of species k in the mixture.

On this latest form of equation (2.47), one has to model the diffusion velocity of species k, V_k. According to [14] two main approaches are distinguished: the Fick's law and the

Hirschfelder and Curtiss approximation. The Fick's law is based on equal binary diffusion coefficients and the gradient of the logarithmic of the mass fractions and it is proved not to be a good approximation for detailed analysis and complex kinetics. As a result, the Hirschfelder and Curtiss approximation is commonly proposed using a correction velocity, to ensure mass conservation ($\sum_{k=1}^{N} Y_k \mathrm{V}_k = 0$), then the species diffusion velocity can be approximated as:

$$\begin{aligned} \mathrm{V}_k &= -D_k \frac{\nabla Y_k}{Y_k}, \quad or \\ \mathrm{V}_k Y_k &= -D_k \nabla Y_k \end{aligned} \tag{2.48}$$

Replacing equation (2.48) into (2.47) we find:

$$\frac{\partial \rho Y_k}{\partial t} + \nabla \cdot (\rho V Y_k) = \nabla \cdot (\rho D_k \nabla Y_k) + \dot{\omega}_k \tag{2.49}$$

Equation (2.49) is a convenient formula since the diffusion coefficient D_k can be easily linked to the thermal diffusivities D_{th}, which is a property of the fluid, through the Lewis number, $Le_k = D_{th}/D_k$. The most simple approach is to assume Lewis numbers of unity, which leads to the conclusion that $D_{th} = D_k$ and we end up to the final form of the species equation:

$$\frac{\partial \rho Y_k}{\partial t} + \nabla \cdot (\rho V Y_k) = \nabla \cdot (\rho D_{th} \nabla Y_k) + \dot{\omega}_k \tag{2.50}$$

The thermal diffusivity is found from:

$$D_{th} = \frac{k}{\rho C_p} \tag{2.51}$$

where k is the thermal conductivity and C_p is the specific heat capacity.

The chemical source term $\dot{\omega}_k$ is calculated by the following expression:

$$\dot{\omega}_k = W_k \sum_{j=1}^{M} (v''_{kj} - v'_{kj}) \mathcal{Q}_j \tag{2.52}$$

where W_k is the molecular weight of species k, v''_{kj} and v'_{kj} are the molar stoichiometric coefficients of species k in the reverse and forward reaction j respectively. In a detailed chemistry mechanism hundreds of chemical reactions take place and a single species k may participate in a number M out of them. That is the use of the sum operator over M number of reactions to reflect the overall mass production (or consumption) of a species k. $\mathcal{Q}_j$ is the rate of progress of reaction j and is defined as:

$$\mathcal{Q}_j = K_{fj} \prod_{s=1}^{N} [X_s]^{v'_{sj}} - K_{rj} \prod_{s=1}^{N} [X_s]^{v''_{sj}} \tag{2.53}$$

where $[X_s]$ is the molar concentration of species s. The reaction rate source term can be easily related to the species mass fractions using the relation $[X_s] = \rho Y_s / W_s$:

$$\dot{\omega}_k = W_k \sum_{j=1}^{M} (v''_{kj} - v'_{kj}) \left[K_{fj} \prod_{s=1}^{N} \left(\frac{\rho Y_s}{W_s} \right)^{v'_{sj}} - K_{rj} \prod_{s=1}^{N} \left(\frac{\rho Y_s}{W_s} \right)^{v''_{sj}} \right] \tag{2.54}$$

By K_{fj} and K_{rj} we denote the forward and reverse rates of reaction j. The forward coefficient can be modeled by the Arrhenius law:

$$K_{fj} = A_{fj} T^{\beta_j} exp\left(-\frac{E_j}{R_u T} \right) \tag{2.55}$$

where A_{fj} is a preexponential constant, β_j is the temperature exponent and E_j is the activation energy. The reverse coefficient can be computed from the forward one through equilibrium constants:

$$K_{rj} = \frac{K_{fj}}{\left(\frac{p_a}{R_u T} \right)^{\sum_{k=1}^{N} v_{kj}} exp\left(\frac{\Delta S_j^0}{R_u} - \frac{\Delta H_j^0}{R_u T} \right)} \tag{2.56}$$

where $p_a = 1$ bar, ΔS_j^0 and ΔH_j^0 are respectively the entropy and enthalpy changes for reaction j.

2.4.5. Summary of the system of equations

In the previous sections an effort was done to derive the fundamental transport equations that describe the flow field and one has to resolve in a typical combustion problem. An emphasis was given to the physics governing those equations (application of mass conservation, Newton's law, energy conservation). The equations were given in an extended form so that the reader can have a direct contact with underlying physical aspects. In this section these equations will be written in a more compact form using index notation.

The Einstein summation convention is used which means that repeated indices imply summation, for example

$$\frac{\partial}{\partial x_i} \rho u_i u_j = \frac{\partial}{\partial x_1} \rho u_1 u_j + \frac{\partial}{\partial x_2} \rho u_2 u_j + \frac{\partial}{\partial x_3} \rho u_3 u_j$$

Continuity Equation:

$$\frac{\partial \rho}{\partial t} + \frac{\partial \rho u_i}{\partial x_i} = 0 \tag{2.57}$$

Momentum Equation:

$$\frac{\partial \rho u_j}{\partial t} + \frac{\partial \left(\rho u_i u_j \right)}{\partial x_i} = -\frac{\partial p}{\partial x_i} + \frac{\partial \tau_{ij}}{\partial x_i} + \rho \sum_{k=1}^{N} Y_k f_{k,j} \tag{2.58}$$

Energy Equation:

$$\frac{\partial \rho h}{\partial t} + \frac{\partial (\rho u_i h)}{\partial x_i} = \frac{Dp}{Dt} - \frac{\partial \dot{q}_i}{\partial x_i} + \tau_{ij}\frac{\partial u_j}{\partial x_i} + \rho \dot{q}_v + \rho \sum_{k=1}^{N} Y_k f_{k,i} \mathrm{V}_{k,i} \tag{2.59}$$

Species Equation:

$$\frac{\partial \rho Y_k}{\partial t} + \frac{\partial (\rho u_i Y_k)}{\partial x_i} = \frac{\partial}{\partial x_i}\left(\rho D_{th}\frac{\partial Y_k}{\partial x_i}\right) + \dot{\omega}_k \tag{2.60}$$

Enthalpy Equation:

$$h = h_s + h_{chem} = \int_{T_o}^{T} C_p dT + \sum_{k=1}^{N} \Delta h^o_{f,k} Y_k \tag{2.61}$$

Equation of State:

$$p = \rho R T \tag{2.62}$$

The derivation and significance of each and every term on equations (2.57)-(2.62) was explained in detail in the previous sections. The gas constant R is related to the universal gas constant R_u via $R = R_u/W$, where $W = \sum_{k=1}^{N} X_k W_k$ is the mean molecular weight and X_k is the mole fraction. As a note, the subscript k refers to the different species, is not an index for tensor notation and so the Einstein summation does not apply on it.

2.4.6. The system of equations for spray combustion

The equations (2.57)-(2.62) presented above apply to a single continuous phase flow (e.g. gas phase) in combustion. The nature of spray combustion, which is the study of this project, entails two phase flows. The fuel is provided on liquid phase (spray), then it is heated up and its evaporation begins leading to generation of fuel vapor which in consequence burns. As a result, the system of the gas equations as it was presented in the previous section needs to be modified accordingly in order to take into consideration the influence of the generated fuel vapor due to the evaporation. For that reason additional evaporation source terms needs to be included on the set of gas equations as it is shown below:

Continuity Equation:

$$\frac{\partial \rho}{\partial t} + \frac{\partial \rho u_i}{\partial x_i} = S^v_\rho \tag{2.63}$$

Momentum Equation:

$$\frac{\partial \rho u_j}{\partial t} + \frac{\partial (\rho u_i u_j)}{\partial x_i} = -\frac{\partial p}{\partial x_i} + \frac{\partial \tau_{ij}}{\partial x_i} + \rho \sum_{k=1}^{N} Y_k f_{k,j} + S^v_{u_j} \tag{2.64}$$

Energy Equation:

$$\frac{\partial \rho h}{\partial t} + \frac{\partial (\rho u_i h)}{\partial x_i} = \frac{Dp}{Dt} - \frac{\partial \dot{q}_i}{\partial x_i} + \tau_{ij}\frac{\partial u_j}{\partial x_i} + \rho \dot{q}_v + \rho \sum_{k=1}^{N} Y_k f_{k,i} \mathrm{V}_{k,i} + S_h^v \tag{2.65}$$

Species Equation:

$$\frac{\partial \rho Y_k}{\partial t} + \frac{\partial (\rho u_i Y_k)}{\partial x_i} = \frac{\partial}{\partial x_i}\left(\rho D_{th}\frac{\partial Y_k}{\partial x_i}\right) + \dot{\omega}_k + S_{Y_k}^v \tag{2.66}$$

Enthalpy Equation:

$$h = h_s + h_{chem} = \int_{T_o}^{T} C_p dT + \sum_{k=1}^{N} \Delta h_{f,k}^o Y_k \tag{2.67}$$

Equation of State:

$$p = \rho R T \tag{2.68}$$

Soret and Dufour effects will be ignored. Soret effect describes the species diffusion caused by a temperature gradient (thermal diffusion), while Dufour effect describes the heat diffusion caused by concentration gradients [15]. The S^v terms in each equation represent the source terms due to spray evaporation. We should mention here that in principle the source terms are non-zero only on the interface between the liquid and the gas phase. The liquid phase or the spray in most of the cases and also in this report is treated as a batch of spherical droplets and due to this assumption specific expressions for those source terms can be derived as it is shown in the following section.

2.5. Liquid phase analysis

2.5.1. Introduction

In spray combustion problems the analysis and the modeling of the liquid phase is determinant. The injection of the liquid fuel, its disintegration into fuel droplets, the motion of the droplets, the droplets evaporation, the mixing and how this is related to the chemical reaction and the interaction of the droplets with: the flow field of the gas phase, the flame, other droplets [16], walls, are key issues.

The essential processes to be understood in a spray flame are the injection of the liquid fuel, its atomization into droplets, droplet evaporation, the determination of the flow field of both the gas and the dispersed flow and the coupling between them [17].

Initially, the bulk liquid fuel is injected in the form of a liquid jet or sheet and then directly begins its disintegration into ligaments and big droplets. This mechanism is known as primary atomization [18]. In sequence the secondary atomization follows where a further disintegration of these ligaments and big droplets into smaller fragments occurs. The reason for the secondary atomization is due to the aerodynamic forces that arise because of the relative

inter-phase velocities causing instabilities [19]. Enhanced breakup of the bulk liquid creates a larger fuel surface and helps for a faster evaporation.

Two different approaches can be used to treat the discrete phase, depending on the dispersed phase volume fraction [19]. If the volume fraction is above 10^{-3} the regime is referred as dense and the Eulerian framework is preferred. In that case the dispersed phase is modeled as a continuum medium and transport equations for continuum properties are solved, using the volume fraction (the fraction of space occupied by the liquid on a grid cell) [20]. This method has the disadvantage that the shape of the droplets and more generally the shape of the interface between the phases is lost and the description of evaporation becomes more difficult. In the other case where the volume fraction is less than 10^{-3} the regime is referred as dilute and the Lagrangian framework is selected. In that case the droplets according to their initial diameter, velocity, temperature etc. are grouped into parcels and equations that describe their motion are solved. In this report the liquid fuel is dilute and the Lagrangian framework will be used for the dispersed phase. In the lagrangian approach the liquid phase is also called discrete or dispersed or particle phase. In any case the gas phase can be called as continuous or carrier phase.

To sum up, three main processes can be identified regarding the dispersed phase: a) atomization which is the disintegration of the liquid fuel into droplets due to instabilities caused by aerodynamic forces, b) dispersion which refers to the motion of the droplets meaning the change of their position and velocity in time and c) evaporation which involves the heat and mass transfer between the two phases.

Atomization is out of the scope of the current project, however it was discussed briefly for the sake of clarity and to give some insight to the readers, analytical description can be found in [17–19]. The following sections are devoted to description of dispersion and evaporation.

2.5.2. Dispersion model

For a single droplet (or a parcel which is a group of droplets with same characteristics and adding a droplet number density) we can apply the principle of the mass conservation which states that *the time rate of the fuel vapor mass leaving the volume of the droplet equals the time rate of decrease of liquid mass inside the droplet*. This can be simply written as:

$$-\frac{dm_p}{dt} = \dot{m}_v \tag{2.69}$$

where the index notation p refers to droplet and v to the vapor.

The velocity of a particle droplet can be expressed as:

$$\frac{dx_p}{dt} = V_p \tag{2.70}$$

where x_p is the position vector of the droplet and V_p is its velocity vector. According to [21] if we assume spherical droplets, high liquid to vapor density ratio and no vortical flow for the droplet we can write for the acceleration of the droplet:

$$\frac{dV_p}{dt} = \frac{V_{seen} - V_p}{\tau_p} + g \tag{2.71}$$

where V_{seen} is the gas phase velocity "seen" (bulk gas velocity away from droplet) by the droplet. The relative velocity of the droplet to the local velocity of the gas phase ($V_p - V_{seen}$) is commonly named as the slip velocity. The term $(V_{seen} - V_p)/\tau_p$ expresses the drag force per unit mass acting on the droplet. To clarify, all the continuous (gas) phase quantities found in the lagrangian (particle) governing equations are evaluated at the particle's location. Thus, if V is the velocity vector of the gas phase then the gas phase velocity "seen" by the droplet, V_{seen}, is found as $V_{seen} = V(x_p(t), t)$. τ_p is the particle relaxation time scale defined [22] as the rate of response of particle's acceleration to the relative velocity between the particle and the carrier fluid and is given by:

$$\tau_p = \frac{4}{3}\frac{\rho_p}{\rho_g}\frac{D_p}{C_D|V_{seen} - V_p|} \tag{2.72}$$

where C_D is the drag coefficient, D_p and ρ_p are the particle's diameter and density respectively and ρ_g is the local carrier gas phase density.

The drag coefficient C_D is proposed by L. Schiller and A. Naumann [23] as:

$$C_D = \left\{ \begin{array}{ll} \frac{24}{Re_p}(1 + 0.15Re_p^{0.687}), & Re_p \leq 1000 \\ 0.44, & Re_p > 1000 \end{array} \right\} \tag{2.73}$$

the particle's Reynolds number (Re_p) is based on the slip velocity and is defined as:

$$Re_p = \frac{\rho_g|V_{seen} - V_p|D_p}{\mu_{film}} \tag{2.74}$$

where and μ_{film} is the dynamic viscosity of the mixture in the film layer around the particle. In the following section the film theory for the heat and mass transfer around a particle will be discussed.

In literature, first M.C.Yuen et al. [24] reported that the reduction of mass of the droplet due to evaporation can lead to reduction of the drag coefficient, C_D, the same was reported by Abramzon et al. [25] and finally a correction for the drag coefficient was given by Sazhin et al. [26] to include the effect of evaporation:

$$C_{D,evap} = \frac{C_D}{(1 + B_M)^a}, \quad a = \left\{ \begin{array}{ll} 1, & B_M < 0.78 \\ 0.75, & B_M \geq 0.78 \end{array} \right\} \tag{2.75}$$

where B_M is the Spalding mass transfer number and is described in the following section.

The droplet velocity model describes the dispersion of droplets in gaseous surroundings and it should not be confused with the turbulent dispersion modeling. As mentioned previously the velocity of the gas phase experienced by the droplet is given as $V_{seen} = V(x_p(t), t)$. However when the flow is turbulent, it can be decomposed into a mean flow and its fluctuations. Thus, when a droplet is exposed in a turbulent environment it experiences, "sees" a velocity from the gas phase as:

$$V_{seen} = \widetilde{V}(x_p(t), t) + u''_{seen} \tag{2.76}$$

The process of determining the fluctuating component, u''_{seen}, is called turbulent dispersion modeling [21, 22].

2.5.3. Evaporation model

In this section the models that describe the heat and mass transfer between the dispersed phase and the carrier phase are analysed. For a single droplet we can apply the film theory. According to that, we assume a film (of gas) that surrounds the droplet and across that film the heat and mass transfer between the liquid and the bulk gas phase occur. This film is a useful tool to overcome the discontinuities between the liquid and the bulk gas phase properties. If we apply the film theory around the droplet, we can simply identify four different regions and models as shown in Figure 2.5. The first refers to the volume of the droplet and the representative model is called the Liquid Phase Model (LPD), the second region refers to the surface of the droplet where the Droplet Surface Properties model (DSP) is used, the third region is related to the film between the liquid and the bulk gas phase where the heat and mass transfer take place and we use the gas side Heat and Mass Transfer model (HMT) and finally the fourth region which refers to the properties of the gas that are experienced ”seen” from the droplet using the ”seen” Gas Properties model (SGP) [2].

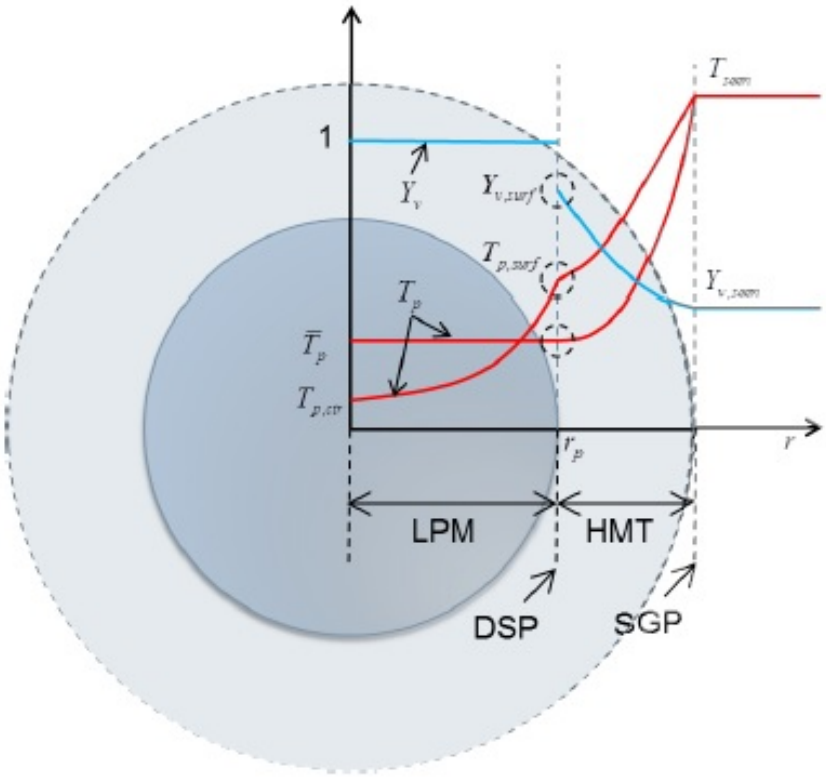

Figure 2.5: Application of the film theory in a droplet [2]

Regarding the volume of the droplet, Liquid Phase Model (LPD), there are a few approaches for the temperature evolution inside the droplet. To name a few there are models based on the assumption that the droplet's temperature is constant in time, others that are unsteady but present no temperature gradient inside the droplet (infinite conductivity models) and others that assume a finite conductivity and thus temperature gradients inside the droplet [27]. In

this report we are focusing on the infinite conductivity model [28] due to its computational efficiency and easiness to implement. For more information about other models the readers are referred to [25] and [15].

The temperature evolution of a single droplet described by the infinite conductivity model, assuming that the thermal energy exchange between the two phases occurs only due to convective heat transfer, is given as:

$$\frac{dT_p}{dt} = \frac{\pi D_p \lambda_{film} Nu}{m_p C_{p,liq}} \left(T_{seen} - T_p\right) + \frac{1}{C_{p,liq}} \frac{L_v(T_p)}{m_p} \dot{m}_p \tag{2.77}$$

where T_p, D_p, are the droplet's temperature and diameter respectively, λ_{film} is the gas phase thermal conductivity inside the film, Nu is the Nusselt number, $C_{p,liq}$ is the specific heat capacity for the liquid phase and $L_v(T_p)$ is the latent heat of evaporation for the corresponding T_p temperature of the droplet. Note that this equation does not include the Stefan flow effects, and some corrections are proposed in the following. The temperature evolution as it is described by equation (2.77) corresponds to Figure 2.5 for the case of uniform temperature inside the droplet's volume. Also the case of finite conductivity model, where a temperature gradient exists inside the droplet, is shown in Figure 2.5.

The time rate of change of the mass of the droplet is given by:

$$\frac{dm_p}{dt} = \pi D_p Sh D_{vap} \rho_g ln(1 + B_M) \tag{2.78}$$

where Sh is the Sherwood number, D_{vap} is the vapour diffusion coefficient and B_M is the Spalding mass transfer number. We can see that the temperature time rate equation (2.77) is dependent on $\dot{m}_p$, thus it is coupled to the droplet's mass time rate equation (2.78).

The Nusselt and Sherwood numbers that were used in equations (2.77) and (2.78) are indicators of the importance of convection in the flow in terms of heat and mass respectively. Following the Ranz-Marshall correlation we obtain for these two characteristic numbers:

$$Nu = 2 + 0.552 Re_p^{1/2} Pr_{film}^{1/3} \tag{2.79}$$

$$Sh = 2 + 0.552 Re_p^{1/2} Sc_{film}^{1/3} \tag{2.80}$$

In equations (2.79) and (2.80) the Prandtl and Schmidt numbers depend on properties in the film (Pr_{film}, Sc_{film}). The former one is an indicator of the proportion between momentum and heat diffusion and the latter one compares the momentum over the mass diffusion and both can be specified for the properties of the gas phase inside the film as:

$$Pr_{film} = \frac{\mu_{film} C_{p,film}}{\lambda_{film}} \tag{2.81}$$

$$Sc_{film} = \frac{\mu_{film}}{\rho_g D_{film}} \tag{2.82}$$

where D_{film} is the diffusivity at the film. In equation (2.78) the Spalding mass transfer (B_M) is introduced and is indicative of the evaporation rate. It is a non-dimensional number which relates the fuel vapor mole fraction at the surface of the droplet (before the film) and the fuel vapor mole fraction experienced, "seen", by the droplet (after the film) and is given by:

$$B_M = \frac{X_{v,surf} - X_{v,seen}}{1 - X_{v,surf}} \tag{2.83}$$

To obtain $X_{v,surf}$ we can make use of Dalton's law under equilibrium conditions which states that the vapor mole fraction at the surface of the droplet equals to the ratio of the partial pressure of fuel vapor to the total pressure of the gas. In some CFD codes (e.g. OpenFoam) this law is used, whereas other codes calculate the vapor mole fraction at the surface using a Clausius-Clapeyron equation [28]. The surrounding film around the droplet may be disturbed due to Stefan's flow effects meaning the blowing velocity (the velocity with which the vapour is leaving away from the droplet) can thicken the layer around the droplet affecting the heat and mass transfer processes. To account for these effects different corrections have been proposed in literature. Miller et al. [28] proposed a correction in the calculation of the mole fraction by using the Knudsen layer thickness and the evaporation parameter β. Alternatively, Abramzon and Sirignano [25] proposed an iterative method that corrects the Nusselt and Sherwood numbers using the Spalding heat transfer number. Finally a third option, which is adopted in the current report, is the Bird's correction [29] which uses the evaporation parameter β to correct the Nusselt number as shown below:

$$Nu' = Nu\frac{\beta}{e^{\beta} - 1} \tag{2.84}$$

As shown earlier, the equations that describe the heat and mass transfer across the droplet's surface depend on the properties of the gas in the film that surrounds the droplet (μ_{film}, $C_{p,film}$, etc.). The properties of the gas between the surface of the droplet and the bulk gas away from the droplet change fast. So, in order to find the properties of the gas inside this film, literature proposes the use of weighted averages between the gas at the surface and the bulk gas away from the droplet [2, 30]:

$$T_{v,film} = (1 - \alpha)T_{v,surf} + \alpha T_{v,seen} \tag{2.85}$$

$$Y_{v,film} = (1 - \alpha)Y_{v,surf} + \alpha Y_{v,seen} \tag{2.86}$$

Possible values for α are $1/3$ [31], $1/2$ [32] or 1. In the current report $\alpha = 1/3$ is used which is the so-called "$1/3 \quad rule$". Then the needed gas properties in the film can be found as:

$$\begin{aligned} \mu_{film} &= \mu(T_{v,film}, Y_{v,film}), \quad C_{p,film} = C_p(T_{v,film}, Y_{v,film}), \\ \lambda_{film} &= \lambda(T_{v,film}, Y_{v,film}), \quad D_{film} = D(T_{v,film}, Y_{v,film}) \end{aligned} \tag{2.87}$$

2.6. Turbulence

2.6.1. Introduction

As it is already mentioned in the first chapter, the computational study of this thesis is limited to the area of laminar flow calculations. However, as it will be described in the following sections, these laminar spray combustion calculations are done to contribute in an extension to two-phase flows of the Flamelet Generated Manifold (FGM) technique, which is a method to calculate turbulent combustion. Therefore, it is considered here appropriate to quote a brief description of the different methods that are available for the calculation of turbulent combustion.

Turbulent combustion is the result of the mutual interaction between turbulence and chemistry. When a flame interacts with a turbulent flow, the turbulence is affected by combustion because of the strong flow accelerations through the flame front induced by heat release and because of the large changes in kinematic viscosity associated with temperature changes. On the other hand, turbulence affects the flame structure which may enhance the chemical reaction but also in extreme cases inhibit it leading to flame quenching [14].

In a turbulent flow, the streamlines become irregular and chaotic and the fluid elements move in a random, irregular and tortuous fashion creating eddies. These eddies have the tendency to break into smaller eddies due to vortex stretching. The mechanical energy provided by the main flow is transferred to the eddies in the form of kinetic energy and as the big eddies break into smaller eddies the kinetic energy cascades to the smaller eddies. This happens till the breakage leads to the smallest scale of eddies (Kolmogorov scale) where the kinetic energy transforms into heat due to viscosity. This important process is called energy cascade. The convective term $\frac{\partial(\rho u_i u_j)}{\partial x_i}$ appearing in the Left-Hand Side of equation (2.64) is quadratic and non-linear and is the determinant factor for the transition from laminar to turbulent flow. Especially when this term becomes much larger than the diffusive term $\frac{\partial \tau_{ij}}{\partial x_i}$ found in the Right-Hand Side of equation (2.64), the flow becomes unstable and breaks into eddies. This comparison between the convective and diffusive term can be indicated through the Reynolds number which is the ratio of inertia to viscous forces [33].

In the previous sections when we derived the transport equations (2.63-2.66) we stated that their solution can give the information of the properties (ρ, P, V, h, Y_k) that describe the flow field. To be more precise this statement is completely true only if initial and boundary conditions are given. The boundary conditions determine how the flow on the volume boundaries should look like and the initial condition gives the complete flow of the domain at an initial moment [34]. At this point it is important to make a distinction between the applicability of the transport equations (2.63-2.66) on laminar and turbulent flows. Referring to laminar flows, in the momentum equation the non-linear convective term is not dominant and as a result the direct solution of the equations (2.63-2.66) together with initial/boundary conditions can predict the flow field accurately in a deterministic manner. On the other hand if the convective term of the momentum equation becomes orders of magnitude larger than the diffusive term, the nature of the momentum equation becomes unstable, highly non-linear and chaotic, we have creation of turbulence, there is sensitive dependence of the flow on the initial and boundary conditions and a direct analytical solution of the momentum equation is not possible.

2.6.2. Methods for calculation of turbulence

In order to calculate turbulent flows numerically, three main approaches are indicated [14]:

DNS

The first, as in the case of a laminar flow, refers to the direct resolution of the transport equations, requiring that a very fine grid is used during a numerical simulation and this method is called DNS (Direct Numerical Simulation). In that case the size of a single grid cell should be smaller than the smaller eddy scale (Kolmogorov scale) of the flow, so that the momentum equation from a grid point to another adjacent point becomes stable (as for the case of laminar flow). The number of the grid points needed for a DNS are proportional to $\mathcal{O}(Re^{9/4})$ [34] $\sim$ $\mathcal{O}(Re^{3})$ [33], where Re is the Reynolds number. Furthermore, the simulation domain should be sufficiently large to contain all the large-scale motions. It is clear that the computational power needed for the calculation of such a big and fine mesh makes the choice of DNS often prohibitive. However, the use of the DNS approach can be feasible for cases of low turbulence level and simple geometries with the help of supercomputers. Despite the expensive computational cost, direct numerical simulations offer very high accuracy, they don't require the use of any turbulence model and they determine all turbulence scales capturing so their effects on combustion.

RANS

The second approach is the RANS (Reynolds Averaged Navier Stokes) and was created in order to overcome the barrier of obtaining the instantaneous flow field in a turbulent flow by calculating the mean values of all quantities. These averaged quantities are obtained by averaging the instantaneous transport equations. For a stabilized flame, any value predicted with RANS (e.g. temperature) at a specific point is constant in time and corresponds to the mean (time average) quantity at this point. The calculation is a lot faster than a DNS, but it is far less accurate since it provides information only about the averaged quantities and also it requires closure models: a) a turbulence model to deal with the flow dynamics and b) a turbulent combustion model to describe the chemical species conversion and heat release.

LES

In between the DNS and RANS approaches, in terms of accuracy and computational cost, there is the third method called as LES (Large Eddy Simulation). The LES calculation directly solves the turbulent large scales (the DNS solves all sizes of turbulent scales), while the effects of the smaller scales are modeled using subgrid closure rules (the RANS requires closure models for all the scales). To do so, the transport equations are filtered in spectral space (Fourier transformed fields) or in physical space, using a filter function (e.g cut-off filter, Gaussian filter). In that way, eddies of larger wave numbers (spectral space) or of smaller scale (physical space) than the filter length are removed (to be modeled), and eddies of smaller wave numbers and of larger scale are solved explicitly. The grid for a LES calculation should be sufficiently fine and locally a single grid cell should be smaller than the eddy scale allowed by the filter (to avoid high non-linearities and instabilities). LES method should be highly preferred over RANS method for cases of fully unsteady flames or to calculate the unsteady parts of a steady flame (ignition, quenching, etc.).

It should be highlighted here that RANS and LES approaches have no affinity and are com-

pletely different methods. The former one relies on a statistical description of the flow and its operation is based on an averaging procedure, while the later one relies on a scale separation between the larger and the smaller-energy containing eddies of the flow and its operation is based on a low-pass filter in the wave numbers space.

2.6.3. RANS and LES equations

In this section we will apply averaging in the instantaneous transport equations to identify the modeling issues that are linked to turbulence and combustion from a mathematical point of view. For constant density flows, Reynolds averaging starts from the observation that any property f can be split into its mean $\overline{f}$ and its fluctuation f' :

$$f = \overline{f} + f' \tag{2.88}$$

To obtain the mean value of a property an ensemble average is needed (average of a large number of realizations at the same instant of the same flow field). However, for steady state flows, the time average is used over a sufficiently long period t:

$$\overline{f} = \frac{1}{t}\int_0^t f(t')dt' \tag{2.89}$$

here, t declares a finite time period and is constant and t' is the independent variable of integration. For variable density flows, Reynolds averaging introduces many unclosed terms between any quantity f and density fluctuations, $\overline{\rho' f'}$. To avoid this obstacle Favre averages (mass-weighted averages) are preferred. Then any property f can be written as a composition of its mean and its fluctuation:

$$f = \widetilde{f} + f'' \tag{2.90}$$

applying the Favre average, the mean value is written:

$$\widetilde{f} = \frac{\overline{\rho f}}{\overline{\rho}} \quad or \quad \overline{\rho f} = \overline{\rho}\widetilde{f} \tag{2.91}$$

Analogously to the averaged and Favre-averaged quantities that we defined for the RANS approach, for LES we can set the filtered and Favre-filtered quantities of the flow field. In literature several notations have been used to describe the application of filtering and Favre-filtering. However, for simplicity we choose here to use the same notation that was used for the averaging and Favre-averaging. Thus, for any quantity f, the $\overline{f}$, $\widetilde{f}$ and f'' stand for the time average (or ensemble average), the Favre-average and the fluctuation due to the influence of all the turbulent scales in the mean flow respectively in the RANS approach, while they stand for the filtered (resolved) large turbulent scales, the Favre-filtered values and the influence of the small turbulent scales (sub-grid scale, to be modeled) in the resolved large scales respectively for the LES approach.

Now we can apply averaging/filtering on the continuity, momentum, energy and species mass fractions equations (2.63-2.66):

Continuity Equation:

$$\frac{\partial \overline{\rho}}{\partial t} + \frac{\partial \overline{\rho}\widetilde{u}_i}{\partial x_i} = \overline{S}_{\rho}^{v} \tag{2.92}$$

Momentum Equation:

$$\frac{\partial \overline{\rho}\widetilde{u}_j}{\partial t} + \frac{\partial \left(\overline{\rho}\widetilde{u}_i\widetilde{u}_j\right)}{\partial x_i} = -\frac{\partial \overline{p}}{\partial x_i} + \frac{\partial \overline{\tau}_{ij}}{\partial x_i} - \frac{\partial \left(\overline{\rho}\widetilde{u_i'' u_j''}\right)}{\partial x_i} + \overline{\rho}\sum_{k=1}^{N}\widetilde{Y_k f_{k,j}} + \overline{S}_{u_j}^{v} \tag{2.93}$$

Energy Equation:

$$\frac{\partial \overline{\rho}\widetilde{h}}{\partial t} + \frac{\partial \left(\overline{\rho}\widetilde{u}_i\widetilde{h}\right)}{\partial x_i} = \frac{D\overline{p}}{Dt} - \frac{\partial \overline{\dot{q}}_i}{\partial x_i} - \frac{\partial \left(\overline{\rho}\widetilde{u_i'' h''}\right)}{\partial x_i} + \overline{\tau_{ij}\frac{\partial u_j}{\partial x_i}} + \overline{\rho}\widetilde{\dot{q}} + \overline{\rho}\sum_{k=1}^{N}\widetilde{Y_k f_{k,i} \mathrm{V}_{k,i}} + \overline{S}_{h}^{v} \tag{2.94}$$

Species Equation:

$$\frac{\partial \overline{\rho}\widetilde{Y}_k}{\partial t} + \frac{\partial \left(\overline{\rho}\widetilde{u}_i\widetilde{Y}_k\right)}{\partial x_i} = \frac{\partial}{\partial x_i}\left(\overline{\rho D_{th}\frac{\partial Y_k}{\partial x_i}}\right) - \frac{\partial \left(\overline{\rho}\widetilde{u_i'' Y_k''}\right)}{\partial x_i} + \overline{\dot{\omega}_k} + \overline{S}_{Y_k}^{v} \tag{2.95}$$

In the above equations (2.92-2.95) there are unclosed terms that do not allow for the direct solution of the averaged/filtered equations and need to be modeled first, this is known as the closure problem.

Reynolds stresses (RANS) / Sub-grid scale stresses (LES)

In the momentum equation (2.93), the term $\overline{\rho}\widetilde{u_i'' u_j''}$ is unclosed and needs to be modeled in either RANS or LES approach. It is a tensor (nine components) and its units are Newton per squared meters, so it has the dimensions of stress. Thus, it is seen that the superposition of the fluctuations on the resolved motion gives rise to additional stresses acting on the surface of a moving fluid element of the flow. As in the case of a laminar flow where the stresses have their source in viscosity (which is a molecular fluid property), similarly according to [13] we can claim that the stresses provoked by turbulent scales are caused by an eddy viscosity, which in that case is a macroscopic flow property. The eddy viscosity can be higher orders of magnitude than the laminar flow viscosity and in most cases the turbulent stresses outweigh the viscous stresses. To close the turbulent stresses in the RANS approach, the Turbulent Eddy Viscosity Hypothesis (also called Boussinesq eddy viscosity assumption) is commonly used for isotropic turbulence [35]. This relationship introduces the eddy viscosity (μ_t) which also needs to be closed. This can be done, by using two transport equations for turbulent kinetic energy (k) and its dissipation rate (ε) respectively, the so-called turbulence $k-\varepsilon$ model [14]. For anisotropic turbulence, Algebraic Stress Models (ASM) are proposed where Reynolds stresses are dependent on k, ε through algebraic expressions, or Reynolds Stresses Models (RSM) can be used where the Reynolds stresses are expressed through differential transport equations [36]. Similarly for LES a turbulent viscosity hypothesis is urged where a sub-grid scale eddy viscosity is introduced and needs to be closed in turn for example via Smagorinsky model [36].

The smaller scales that have to be modeled in LES are more isotropic than the bigger scales, and so the eddy viscosity hypothesis can be applied with more safety in that case.

RANS turbulent / LES sub-grid scale scalar fluxes

In equations (2.94) and (2.95) we observe respectively the terms $\widetilde{u_i'' h''}$ and $\widetilde{u_i'' Y_k''}$ that represent second moments of enthalpy and species mass fractions and need to be modeled. Similarly these two terms represent the influence of the unresolved turbulence in the resolved transport of enthalpy and species mass fractions (mean flow for RANS, large turbulent scales for LES). These fluxes are generally closed using gradient assumptions combined with a turbulent diffusivity which is consisted of the eddy viscosity and turbulent Prandtl, Schmidt numbers respectively which are properties of the flow [14], [35].

Mean / Filtered reaction rates

In the averaged/filtered species transport equation (2.95) the term $\overline{\dot{\omega}_k}$, appearing as the averaged/filtered reaction rate source, is under question. If we refer back to equation (2.54), we can see that the relation between the instantaneous reaction rate and the scalars of temperature and species mass fractions is non-linear. This means that even small fluctuations of those two scalars can change the instantaneous reaction rate dramatically. If we also keep in mind that combustion predominantly happens at small scales that are numerically not resolved in both RANS and LES approaches, we can reach to the conclusion that a hypothetical use of the mean or filtered value of temperature and species mass fractions to predict the mean/filtered reaction rate would lead to false results. Thus, higher moments of those scalars are needed to model the mean/filtered reaction rate. Models that deal with the closure of this term are called as combustion models. The choice of the most suitable combustion model is critical for an accurate prediction of the reaction rate. According to D.J.E.M. Roekaerts in [37], there is an increasing variety of different combustion models and so there is need of distinguishing between these models which are more suitable for premixed and which predict better non-premixed combustion systems. Accordingly, premixed flames should be based on combustion models that describe and predict flame propagation as a function of the flame speed. On the other hand, the viability of a non-premixed flame is associated to the local mixing between the fuel and oxidizer and thus the consideration of a mixing and non-reacting scalar (mixture fraction) is essential. The most common models that apply for both modes of combustion (premixed, non-premixed) among others are Probability/Filtered Density Function based models, Eddy Break model, Eddy dissipation Concept model [38], Linear Eddy model. Especially for premixed combustion models such as Bray Moss Libby (RANS), Progress variable model (RANS), Turbulent flame speed closure (LES), Flamelet models based on flame surface density method are used mostly. Finally for non-premixed combustion suitable models are Flamelet models based on mixture fraction, Conditional moment closure models. For more details on combustion models we refer to [37], [14].

2.7. Flamelet-Based Methods

We saw so far that we have to deal with a set of differential equations for the specification of the species mass fractions. Each of those equations encloses a chemical source term which represents the net mass production of a species k out of j consecutive chemical reactions that take place. Each chemical reaction is characterized by its own activation energy and is highly non-linear to temperature and species concentrations. Thus, for the calculation of the chemical

source term of a single species, a set of non-linear equations has to be solved. For the case of a detailed chemical scheme where many different intermediate species and chemical reactions are involved, this set of equations becomes very stiff. This means that each reaction presents its own chemical time scale or response in a numerical calculation. As a consequence, the fastest reactions demand for a smaller time step in order their solution to become stable. Then we realise that detailed chemical schemes increase highly the computational cost and if we add to this the interaction with turbulence, this cost becomes even higher.

Many studies have been made to reduce the size of this problem and the stiffness in the equations. One way is by introducing steady-state and partial equilibrium approximation according to which a species that has a net chemical source term (the net production of this species out of a number of reactions) close to zero and its individual reactions are fast, can be assumed to be in steady-state and is eliminated from the chemical scheme. In that way the number of species is reduced and only species of slower individual reactions are taken into account, reducing also the stiffness of the problem [39], [40]. This method is the so-called conventional reduction technique. However, the major drawback of this approach is that these reduced chemistry models can be used only for the combustion system that is under consideration and do not have a universal character. Last but not least, one needs to have good experience and deep insight into the reaction mechanisms to be able to apply these reduction techniques. Later, this method was further improved from a mathematical scope using an Intrinsic Low Dimensional Manifold by taking into account only the largest time scales [41]. Nevertheless, the main disadvantage of this approach is that the reduced chemistry model might work well in a certain temperature/composition range and be completely wrong for the rest [37]. Especially on regions of low temperature, the reactions become slower and their time scales are comparable with those of convection and diffusion and these two processes are not captured in the local chemical equilibrium methods.

To overcome the limits of the reduction techniques, Peters [42] proposed an alternative method in which the chemical reaction calculations are decoupled from the flow field calculation based on assumptions on the local flame structure. To do so, the species mass fraction equations are solved beforehand for simple one dimensional laminar flames, which are simply called as flamelets, using detailed chemistry schemes. The results of these laminar simulations are filed into look-up tables (pre-computed databases) as functions of a limited set of coordinates. Then, for these coordinates, appropriate transport equations have to be formed and in turn they have to be solved together with the flow field transport equations in the turbulence simulations. Having resolved the field of those coordinates, one can retrieve the corresponding values of the species mass fractions from the look-up tables. Finally, appropriate probability density functions have to be formed accordingly, to calculate the mean/filtered values of the mass fractions since there is statistical dependence due to the influence of turbulence. The main advantages of this tabulated chemistry method are the removal of the stiffness of equations in the turbulence simulation by decoupling the chemical reactions from the flow field, allowing for bigger numerical time steps and coarser grids and the avoidance of modeling mean/filtered chemical source terms and also there is no need to eliminate species in contrast to the other reduction techniques. Also, the number of the equations to be solved during a RANS or LES calculation is significantly reduced, decreasing further the computational cost.

Using this algorithm, different Flamelet-based methods were developed and are based on the assumption that in a multi-dimensional flame, chemical reactions that take place at high temperatures are nearly always fast compared to all turbulent time scales and they concentrate

in thin layers of a width that is typically smaller than the Kolmogorov scale [35]. Considering flows of scale smaller than the Kolmogorov scale as quasi-laminar flows, then these reactive thin layers (of scale smaller than the Kolmogorov scale) are embedded within the quasi-laminar flow field of such an eddy. As a result, the turbulent structures are unable to penetrate into the reaction zone, cannot destroy the flame structure and the effects of turbulence only result in a deformation and straining of the flame sheet [43]. Under that assumption these thin reactive layers are represented by the laminar flamelets which are in turn embedded within the turbulent flow field. Violation of this laminar flamelet structure assumption can occur on cases where either the chemical reactions are too slow due to very low surrounding temperature e.g ignition, extinction, extreme heat losses, etc. and as a result the layer of the reaction zone thickens leading to a width larger of the Kolmogorov scale, or on cases where the turbulence itself is so intense that the Kolmogorov eddies are smaller than the reaction layer and can penetrate into it destroying its structure.

Under the assumption of fast chemistry, the reactions concentrate on the thin layers whose location can be identified as an iso-surface of a non-reacting scalar quantity, namely the mixture fraction z for non-premixed combustion. The flame structure of this thin layer is resolved if we have the information about the species mass fractions and the temperature that we can name as reactive scalars. Then each thin layer (also called as flame front or flame surface) is parametrized by a value of the mixture fraction and its flame structure is associated with the local reactive scalars. It is clear then that each flame structure depends on the local mixture fraction and the reactive scalars can be written as a function of it, $Y_k = Y_k(z)$, $T = T(z)$. We come up with the conclusion that the reactive scalars depend on a single variable, which means that the flame structure is reduced to one dimension only. Thus, only changes perpendicular to the thin layer (as a function of varying z) are important and changes to the other two dimensions parallel to the layer are negligible. Reminding that under the fast chemistry assumption these thin layers occur in a quasi-laminar flow, then the flame structures of these layers can be represented by the flamelets which are one-dimensional laminar flames.

In the following, the derivation of the mixture fraction and its transport equation is given. For simplicity we assume here a single-chemistry-step where only fuel (F), oxidizer (O) and products are involved. Then we can rewrite the species equation (2.49) for the fuel as:

$$\frac{\partial \rho Y_F}{\partial t} + \nabla \cdot (\rho V Y_F) = \nabla \cdot (\rho D \nabla Y_F) + \dot{\omega}_F \tag{2.96}$$

For a single-step, irreversible reaction under stoichiometric conditions, the reaction rate of the fuel can be written as $\dot{\omega}_F = -W_F \nu'_F Q$ (from equation 2.52). If we define the stoichiometric ratio as $s = \frac{\nu'_O W_O}{\nu'_F W_F}$, then the oxidizer's reaction rate equals $\dot{\omega}_O = -W_O \nu'_O Q = s\dot{\omega}_F$, and the species equation for the oxidizer can be written as:

$$\frac{\partial \rho Y_O}{\partial t} + \nabla \cdot (\rho V Y_O) = \nabla \cdot (\rho D \nabla Y_O) + s\dot{\omega}_F \tag{2.97}$$

Combining equations (2.96) and (2.97) we obtain the following expression:

$$\frac{\partial \rho Z}{\partial t} + \nabla \cdot (\rho V Z) = \nabla \cdot (\rho D \nabla Z) \tag{2.98}$$

where, $Z = sY_F - Y_O$ and can be normalized as:

$$z = \frac{Z - Z^O}{Z^F - Z^O} \tag{2.99}$$

where $Z^O = -Y_O^0$, $Z^F = sY_F^0$ and represent the boundary conditions in a counterflow diffusion non-premixed flame where from one side we have the oxidizer (O) stream and from the other the fuel (F) stream. The zero-index (0) refers to the pure oxidizer and fuel streams in the boundaries respectively. We call z as mixture fraction and it is a measure of the local fuel/oxidizer ratio or in other words is the fraction of the mass present locally, which originally is coming from the fuel stream. The mixture fraction has the boundary conditions $z = 1$ in the fuel stream boundary and $z = 0$ in the oxidizer stream boundary where there is no presence of fuel. This normalized value z follows the same convection/diffusion balance equation as Z:

$$\frac{\partial \rho z}{\partial t} + \nabla \cdot (\rho V z) = \nabla \cdot (\rho D \nabla z) \tag{2.100}$$

We should mention here that this derivation for mixture fraction was based on a single-step mechanism and is not valid with multi-step mechanisms where intermediate species and reactions are involved. For such cases, a variation of the formula of mixture fraction based on elemental fractions is needed and is described in detail in the next chapter as part of the calculation procedure of spray flamelets. Nevertheless, we will show that even the elemental-mass-fraction-based mixture fraction can satisfy the mixture fraction transport equation (2.100), so we can claim at this point that equation (2.100) has a universal validity.

The introduction of the mixture fraction variable is very useful since it is independent of any chemical reaction, it gives a measure of the local presence of fuel (mixing) and especially for infinitely fast chemistry the species mass fractions and temperature can be calculated as a function of the mixture fraction and time (for unsteady phenomena), $Y_k = Y_k(z,t)$, $T = T(z,t)$ reducing the number of the independent variables. If we take the general equation (2.49) for species equations and imply that $Y_k = Y_k(z,t)$ we find:

$$\rho \frac{\partial Y_k}{\partial t} = \frac{1}{2}\rho\chi \frac{\partial^2 Y_k}{\partial z^2} + \dot{\omega}_k \tag{2.101}$$

where,

$$\chi = 2D\left(\frac{\partial z}{\partial x_i}\frac{\partial z}{\partial x_i}\right) \tag{2.102}$$

which is called as scalar dissipation rate. Similarly, we can obtain an equation for temperature (neglecting terms that are of lower order than the combustion heat release such as viscous heating, volumetric heating, work of body forces):

$$\rho \frac{\partial T}{\partial t} = \frac{1}{2}\rho\chi \frac{\partial^2 T}{\partial z^2} + \dot{\omega}_T \tag{2.103}$$

where $\dot{\omega}_T$ is the combustion heat release:

$$\dot{\omega}_T = -\frac{1}{C_p}\sum_{k=1}^{N} \Delta h_{f,k}^o \dot{\omega}_k \tag{2.104}$$

Apart from the scalar dissipation rate (χ) that depends on the spatial variables (x_i), we can see that the species and temperature equations (2.101), (2.103) can be solved entirely in the mixture fraction space and are called as flamelet equations. Thus, we can address the whole combustion problem into two separate problems. The solution of a mixing problem by resolving the mixture fraction field in space and the solution of a flame structure problem where the flamelet equations for temperature and species are solved as a function of the mixture fraction.

So far we considered only the case of infinitely fast chemistry, according to which the chemical time scales are orders of magnitude smaller than the flow time scales and thus the Damkohler number defined as:

$$Da = \frac{\tau_f}{\tau_c} \tag{2.105}$$

goes to infinity, where τ_f corresponds to flow time scales and τ_c to chemical time scales respectively. The flamelets generated according to this assumption are unstrained and there is no local mixing point at which fuel and oxidizer coexist, which means that as soon as they meet they burn. The flamelets are strain-free and as we described above the flame structure can be defined uniquely from a single parameter, the mixture fraction (and time for unsteady effects). When this assumption is no longer valid, the flame structure becomes more complex and is expected to depend on flow times, thus the Damkohler number turns to be finite. In that case, in a single flamelet, fuel and oxidizer are pushed to each other, they do not burn instantly and there is a local mixing between them, affecting the reaction zone. These flamelets are strained and the strain rate appears to be an additional parameter that characterises the flame structure. According to Poinsot and Veynante [14] the strain rate (a) and the scalar dissipation rate (χ) to a good approximation can be related in the following formula:

$$\chi = \frac{a}{\pi} exp\left(-2[erf^{-1}(1-2z)]^2\right) \tag{2.106}$$

The scalar dissipation rate as well as strain rate have the same units, $1/s$. They are both non-reacting variables and locally the former one is linked to the mixture fraction gradients, while the later one to the local velocity gradients.

In practice, chemistry effects are only important in the vicinity of the flame front, $z \approx z_{st}$, where reaction takes place and outside this region combustion is zero and all concepts developed for infinitely fast chemistry apply. Thus, it appears that the zone of $z \approx z_{st}$ is characteristic for each and every flamelet. As a consequence, any flamelet can be distinguished from one another by the local value of the scalar dissipation rate χ_{st} at the reaction zone, $z = z_{st}$, and we can create the lookup table as a variety of different flamelets that are characterised from different stoichiometric scalar dissipation rates. Alternatively, a flamelet can also be parametrized by a global strain rate as we will see in the next chapter. Then the reactive scalars temperature and species mass fractions, in the general case of unsteady and finite chemistry effects, are found as $Y_k = Y_k(z, \chi_{st}, t)$, $T = T(z, \chi_{st}, t)$.

We should mention here that the strain is a crucial parameter and is responsible for the sustainability as well as the quenching of the flame. From the one hand, if we assume a completely unstrained flame, the reaction is going to slow down because of the accumulation of the combustion products near the flame front and after a while the flame will extinguish, choked in its own products. A finite value of the strain rate is vital for the flame, because it will

support the reaction zone with fresh reactants sustaining the reaction. However, higher values of strain rate will promote non-equilibrium effects since it will not allow for fuel and oxidizer to relax, mix and react completely, the chemical time becomes comparable to the flow time and eventually chemistry becomes to slow to burn the incoming reactants and quenching occurs, since the heat transferred to the fresh reactants cannot be balanced by the heat released from the combustion. As a matter of completeness and to be specific when previously we referred to unstrained flamelets in infinitely fast chemistry, we assume very low strain rates and not completely zero.

It becomes clear that in flamelet-based-methods, equations of mixture fraction and scalar dissipation rate have to be solved together with the flow field. Under turbulence conditions, the mean/filtered mixture fraction can be found by applying averaging or filtering operation in equation (2.100):

$$\frac{\partial \overline{\rho}\tilde{z}}{\partial t} + \frac{\partial(\overline{\rho}\tilde{u}_i\tilde{z})}{\partial x_i} = \frac{\partial}{\partial x_i}\left(\overline{\rho D \frac{\partial z}{\partial x_i}}\right) - \frac{\partial\left(\overline{\rho}\widetilde{u_i'' z''}\right)}{\partial x_i} \tag{2.107}$$

The term $\widetilde{u_i'' z''}$ is unclosed and needs to be modeled through a gradient assumption using a turbulent diffusivity. According to Peters [35] and Poinsot et al. [14], the mean scalar dissipation rate can be either modeled by the algebraic expression:

$$\tilde{\chi} = \frac{c_\chi}{\tau_t}\widetilde{z''^2} = c_\chi \frac{\varepsilon}{k}\widetilde{z''^2} \tag{2.108}$$

or by a transport equation [35]. c_χ is a constant, τ_t is the turbulent time scale, $\widetilde{z''^2}$ is the variance of mixture fraction and k, ε are the turbulent kinetic energy and its dissipation rate which are calculated by the Reynolds stress model. The variance of mixture fraction is solved also by a transport equation. Then a relation $\tilde{\chi} = \tilde{\chi}_{st} F(\tilde{z}, \widetilde{z''^2})$ [14] is used to find the respective stoichiometric scalar dissipation rate $\tilde{\chi}_{st}$.

The determination of the different scalar variables (species mass fractions, temperature, reaction rates etc) at any point in the turbulent flame can be extracted from the lookup table (neglecting any time dependence), from a certain flamelet of given stoichiometric scalar dissipation rate as a function of the mixture fraction in combination with the use of a joint probability density function (pdf) between the mixture fraction and scalar dissipation rate to account for the influence of turbulence (turbulence/chemistry interaction). For example the averaged species mass fraction $\tilde{Y}_k$ can be calculated from:

$$\tilde{Y}_k = \int_0^{+\infty} \int_0^1 Y_k(z, \chi_{st}) \tilde{p}(z, \chi_{st}) dz d\chi_{st} \tag{2.109}$$

and if z, χ_{st} are assumed statistically independent their joint probability simplifies to:

$$\tilde{p}(z, \chi_{st}) = \tilde{p}(z)\tilde{p}(\chi_{st}) \tag{2.110}$$

The value of $Y_k(z, \chi_{st})$ is retrieved from the look-up table for given values of z and χ_{st}. To calculate the pdf for mixture fraction two ways are proposed by Pope [44]: a) to solve a balance equation for the pdf (e.g. Monte-Carlo simulations [37]) or b) to presume the pdf

shape. The most common choice for combustion problems is to use a presumed β-function shape to construct the pdf of mixture fraction. It requires only two moments of the variable that is under consideration, so here we only need the mean value $\tilde{z}$ and the variance $\widetilde{z''^2}$. The pdf of χ_{st} is usually calculated by log normal distributions [14]. As we can see the statistical considerations in the flamelet concept focus on the location of the flame surface (pdf of z, χ_{st}) and not on the reactive scalars themselves. These reactive scalars profiles are attached to the flame surface and are convected with it in the turbulent flow field.

To conclude, the turbulent flame calculation based on flamelet methods can be divided in two parts: a) the construction of a pre-computed database which is filled with flamelet data (reactive scalars) as a function of a limited set of coordinates using one dimensional laminar counterflow flames and b) the use of multi-dimensinal codes that resolve or model turbulence in order to solve the flow equations together with equations for the set of coordinates used in the look-up table and the use of probability density functions to link the flamelet data with the flow.

Flamelet Generated Manifolds (FGM)

We saw the procedure that the flamelet-based methods follow in order to calculate complex turbulent flows, firstly by calculating the turbulent flow field separately from the chemistry, then calculating the chemistry alone in a simplified laminar flow manner and finally making a link between them using a probability density function to calculate the different reactive scalars. The outcome of this concept is reflected mathematically in equation (2.109). According to this equation any scalar property is calculated as a function of the stoichiometric scalar dissipation rate and the mixture fraction. Nevertheless, this choice of coordinates as independent variables encloses two limitations which are being addressed in the Figure 2.6.

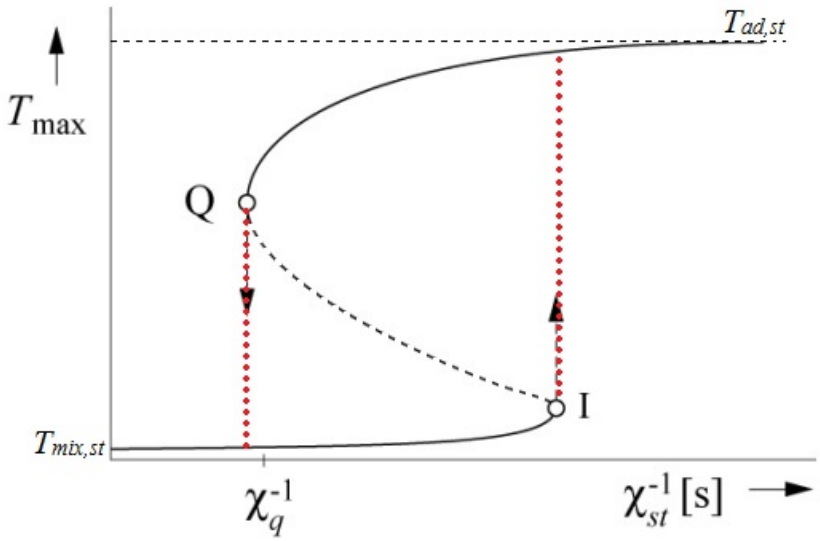

Figure 2.6: The S-shaped curve showing the maximum temperature of of flamelets of varying scalar dissipation rate

Asymptotic analysis of the temperature flamelet equation (2.103), neglecting the temporal term, provides two stable equilibrium curves, which are shown as two continuous black curves in Figure 2.6. They are formed by mapping the peak temperature of each and every flamelet at stoichiometric conditions. Thus, we have the upper continuous branch curve which tends

to reach the adiabatic temperature, $T_{ad,st}$, as $\chi_{st} \rightarrow 0$ (or $\chi_{st}^{-1} \rightarrow \infty$) and the lower branch curve which tends to reach the mixing temperature, $T_{mix,st}$, between fuel and oxidizer at stoichiometric conditions without reaction taking place as $\frac{\partial^2 T}{\partial z^2} \rightarrow 0 \Rightarrow T_{mix,st} = (T_F^0 - T_O^0) z_{st} + T_O^0$.

We should remark that in order to reach adiabatic temperature, ideally this can happen for one-step irreversible mechanisms neglecting heat losses. The lower stable branch represents the family of flamelets that either do not burn at all for infinite χ_{st} or they react very slow for finite large χ_{st}. This branch ends at the ignition point I where the χ_{st} is sufficiently low to create a thermal runaway and a rapid unsteady transition to the upper stable branch. Similarly, starting from close-to-zero χ_{st} values in the upper stable branch, fast reactions take place under large residence times leading to close-to adiabatic temperatures. As the χ_{st} increases, non-equilibrium effects appear until we reach the quenching point Q where the heat loss convected by the fresh reactants cannot be recovered from the heat release of the reaction and quenching of the flame occurs, leading to unsteady rapid transition to the lower non-reacting stable branch.

The stability of the two branches implies that, for any value of χ_{st} outside the I-Q area, no matter the initial conditions we give to the flamelet equations, their final solutions will converge stably to the lower branch for $\chi_{st} > \chi_q$ or to the upper branch for $\chi_{st} < \chi_i$. In contrast, the middle branch which is between the points I-Q is unstable and, for a single value of χ_{st}, the final solution will converge either to the upper branch if the initial conditions are closer to it, or to the lower branch for the opposite case. We realise at this point that the χ_{st} inside the middle branch looses its uniqueness to represent one-to-one flamelets and a single value of the χ_{st} can lead to various flamelets depending on the initial conditions. This brings us to the first limitation of the classical flamelet-based methods where the coordinates of the look-up table are set to be the χ_{st} and z alone.

The second limitation arises from the fact that the time should be an additional variable in the set of coordinates of the look-up table in order to capture unsteady phenomena in real flames. In fact, according to Peters [35], unsteady evolutions of the flamelets in their whole range (from pure mixing till full equilibrium conditions) rarely occur in real flames and so the use of steady state flamelet equations should be sufficient to close the look-up table. However, as he points out, exceptions are the two points indicated by I and Q, the ignition and quenching points. As discussed earlier, these two points are characterized by unsteady transitions due to thermal runways or huge heat losses respectively. Starting from the point I or Q and until reaching the upper or lower branch, the intermediate unsteady flamelets (indicated by red dots in Figure 2.6) carry all the information and the characteristics about the thermal runaway and the extinction processes. These information/characteristics of the thermal runaway and the extinction process at ”microscopic” or flamelet level are essential and deterministic for the accurate prediction of those two marginal processes at the ”macroscopic” level of the real flame and that is why these particular unsteady flamelets should be included in the look-up table. As a conclusion, we can claim that the exclusive use of steady flamelet libraries cannot predict or over-predicts the extinction, ignition and lift-off flame phenomena, since they are based on rapid unsteady transitions in real complex flames and this is reported by many researchers so far [2], [43], [45] and [46] to name a few.

To overcome those two limitations, Oijen [9] developed a new flamelet method, the Flamelet Generated Manifolds (FGM), by introducing a new variable to work as a coordinate in the look-up table. It is called the progress variable and it characterizes the evolution or progress of the reactions from the unburnt or pure mixing state ($C = 0$) to the fully burnt state ($C = 1$). In

general, the progress variable can be defined as:

$$Y_c = \sum_{k=1}^{N} w_k Y_k \tag{2.111}$$

where w_k is a weight factor and Y_k is the mass fraction of a number of selected reaction-product species. As a rule, species that present a monotonic behavior from the mixing until the equilibrium point are selected, such as H_2O and CO_2. In turn, this progress variable is normalized, in order to obtain statistical independence from mixture fraction, as:

$$C = \frac{Y_c - Y_c^u}{Y_c^b - Y_c^u} \tag{2.112}$$

where the superscripts u, b refer to the unburnt and burnt states respectively. The appearing terms Y_c^u, Y_c^b coincide with the minimum and maximum of Y_c respectively. The introduction of the progress variable allows for the unique identification of the flamelets in the table incorporating also the unsteady effects.

Then the working procedure to create the look-up table and to link it in the turbulence flow is as follows: 1) the steady flamelet equations are solved for a range of scalar dissipation rate starting from very low (only mixing) values until extinguishing is reached, 2) the ignition and quenching points then can be identified, for which the unsteady flamelet equations are solved to capture the rapid transitions that dominate in those phenomena, 3) then the progress variable is introduced by selecting appropriate species and the solutions of the flamelets (both steady and unsteady) are mapped into the (z, C) space, 4) to account for the turbulence interaction, the table is pdf-integrated and extended into the ($\tilde{z}$, $\widetilde{z''^2}$, $\tilde{C}$, $\widetilde{C''^2}$) space, 5) appropriate transport equations for mean and variance of z, C have to be solved along with the flow field in the RANS or LES calculation and 6) finally the resolved field of ($\tilde{z}$, $\widetilde{z''^2}$, $\tilde{C}$, $\widetilde{C''^2}$) is used to retrieve the corresponding properties from the look-up table.

3

Working Procedure

3.1. Introduction

In the previous chapter, it was made clear that the closure of the mean/filtered chemical source term in the species mass fraction transport equations is a key point in order to calculate numerically turbulent flames accurately and computationally efficiently. To do so, we referred briefly to different combustion models and different chemical reduction techniques as well. The flamelet-based methods and especially the Flamelet Generated Manifolds (FGM) have attracted the interest of the majority of the combustion research community. This method is based on the decoupling of chemistry from the flow field, based on assumptions on the flame front. The calculation of the chemistry is accomplished by using laminar flamelets and creating look-up tables. The flow field in turn is calculated by resolving or modeling the turbulence in a CFD code. Finally, the flame structure can be linked to the flow field by retrieving the necessary reactive scalars (species mass fractions, temperature) from the look-up tables (see chapter 2 for details). This method is preferable since it allows for detailed chemical schemes, reduces the computational cost by resolving the chemistry in a laminar manner and it is more accurate since it does not require the modeling of the chemical source terms.

The study of a turbulent spray flame is challenging, since it involves the interaction of a multi-phase fluid flow together with heat and mass transfer phenomena originating from the evaporation process and the chemical reactions. The spray or liquid phase for dilute proportions is called as discrete or dispersed phase and requires descriptive differential equations regarding its mass, momentum and energy transfer in a Lagrangian framework. There is a continuous exchange of these three quantities between the discrete phase and the gas phase which is also called as carrier gas and for that reason the two phases need to be coupled by imposing additional source terms in the continuous gas transport equations (2.63-2.66).

Both sets of equations, the Eulerian one for the gas phase and the Lagrangian one for the liquid phase have to be solved simultaneously in the CFD code. In the way to calculate a turbulent spray flame, the question that arises is whether the fuel should be provided in a liquid or gaseous phase form in the flamelet calculations and the creation of the look-up table. The introduction of spray in the flamelet approach, automatically increases the number of independent coordinates of the table in an attempt of solving the spray flamelet equations. Even though, in their recent work [47], H. Olguin and E. Gutheil have reported the development of spray flamelets however, due to the high dimensionality of the table, it has not reported so far a complete and compact creation of a spray flamelet library that could be potentially used

for the calculation of a turbulent spray flame. For that reason, many researchers (e.g Likun Ma [2]) so far are calculating turbulent spray flames with the use of a gaseous flamelet library ignoring there the spray effect.

The aim of this report is to investigate the significance of ignoring the spray effect on the flame structure. Thus, for a specific range of coordinates both ethanol gas and spray flamelets are developed, so that useful conclusions can be created. For that purpose, the open source CFD framework OpenFOAM and the version 2.3.x is used where two different solvers, one for each case, are developed having the names ”le1ReactingFoam” and ”sprayCFoam”.

3.2. OpenFoam

In the current report, we make use of OpenFoam [48] that is a C++ library [49] and can be used as a CFD (Computational Fluid Dynamics) tool in which the fundamental equations that characterize the physical problem can be discretized in a generated mesh and then solved using appropriate numerical schemes. For that purpose, OpenFoam's environment is consisting of three discrete levels [50]: a) the Pre-Processing level where the generation of the mesh is obtained using appropriate utilities (e.g blockMeshDict), b) the Solving level, in which depending on the needs of the physical problem that is under consideration, a combination of suitable solvers (set of corresponding equations and solution algorithms) together with selected utilities (designed to perform tasks that involve data manipulation) are used during the computational process to solve the problem numerically and c) the Post-Processing level where the user is addressed as soon as the computation is over and refers to those utilities (e.g sampleDict) or softwares (e.g Paraview) that allow the user to collect the data/results from the computational environment (mesh), store them into tables and even visualize them showing line graphs on color contour plots for the trends of the different variables.

The variety of the different solvers and utilities to be used in any of the three OpenFOAM's discrete levels is found as precompiled executable files under the directory ”OpenFOAM-2.3.x/applications” [51] and can be called/run directly by the user. Nevertheless, OpenFOAM gives also the freedom to the users to create their own solvers and utilities or to modify existing ones according to their own needs. A solver is actually a set of transport equations that combined together can solve a particular problem. Under the directory ”OpenFOAM-2.3.x/applications/solvers” [51], the user can find a variety of different solvers that cover a wide range of physical problems such as compressible or incompressible flows, heat transfer problems, combustion, lagrangian approaches and more. The utilities as already told, perform pre/post/parallel-processing tasks that involve data manipulation and can be found under the directory ”OpenFOAM-2.3.x/applications/utilities”.

Models that deal with heat transfer phenomena, injection of particles, calculation of forces (e.g drag force etc.), the mass transfer between different phases, atomization or break-up models, turbulence models, combustion models and so many others that basically cover a huge range of physical phenomena can be found under the directory ”OpenFOAM-2.3.x/src” [51]. The range of models found there is such that is not limited only to physics, but the user can find codes that solve ODE systems of equations, calculate matrices or work as meshing and post-processing tools. As we will see later on this chapter, in order to start the calculation of a single case we will have to call many of these models in the case's directories.

3.3. Solvers

As it was mentioned before two libraries of flamelets of varying boundary conditions has to be created. One that includes exclusively gaseous streams and we will refer to these flamelets as the gaseous flamelets and the other that the fuel is provided in a liquid form and we will simply call them as the spray flamelets. The case of the spray flamelets is more complex since it involves the flow of two phases that interact with each other and the equations that describe each phase need to be coupled with the equations of the other phase with the use of source terms.

As it was analysed in the previous chapter, equations that refer to a continuous medium as in the case of gas phase can be solved in the Eulerian framework while those that refer to the discrete phase are solved in the Lagrangian framework. It becomes evident that two different solvers have to be used, one for each library. From the one hand, the precompiled solver "reactingFoam" located in the directory "OpenFOAM-2.3.x/applications/solvers/combustion/ reactingFoam/" [51] was modified into the solver "le1reactingFoam" for the case of the gaseous flamelets and for the case of the spray flamelets the solver "sprayFoam" located in "OpenFOAM-2.3.x/applications/solvers/lagrangian/sprayFoam/" [51] was also modified into the solver "sprayCFoam".

The directory of both solvers should contain the header files: "rhoEqn.H", "pEqn.H", "UEqn.H", "YEqn.H" and "EEqn.H" that represent all the necessary differential equation that need to be solved. The additional "pEqn.H" is a pressure correction equation that is embedded in a PIMPLE loop as it is explained in the following sections. Regarding the species mass fraction equation "YEqn.H", the original solver in OpenFOAM, approximates the mass diffusion coefficient by a unit Schmidt number and replaces the coefficient ρD by the dynamic viscosity (μ) and for that reason a change in the code is made to implement the unit Lewis number assumption by using the thermal diffusivity instead (see equations (2.50), (2.51)). In addition, the energy equation in "EEqn.H" is written in a total energy form including the specific kinetic energy field K for which the momentum equation has to be solved also. The code, as it is originally made, gives the opportunity to the user to choose whether the energy equation should be solved as a function of the enthalpy (h) or of the internal energy (e). Depending on the choice of the user, the pressure term applies as a temporal derivative for the first case according to equation (2.41) or as a divergence convective term for the second case as it is indicated in equation (2.38). Here, we have selected the equation to be solved for the internal energy (e).

All these header files derive the sum of the characteristic equations and consist of functions that need to be called by a source code file, found also under solver's directory and is called as "le1reactingFoam.C" and "sprayCFoam.C" for the gaseous and spray solver respectively. These source code files create a time loop in which for a time moment, the density equation is solved first using the command "#include "rhoEqn.H"". Then, inside the time loop, the pressure velocity PIMPLE corrector loop starts by solving the momentum, species and energy equations, followed by the pressure corrector loop where the pressure correction equation is solved.

3.4. Running a Case

In OpenFOAM environment, when we refer to a single calculation or simulation of given boundary conditions we refer to this as a ”case” and so for the rest of this text we simply call any simulations as cases. The goal of this project is to calculate two sets of cases for varying boundary conditions. The first set refers to the spray flamelets, where fuel is provided in a liquid discrete phase form and the second one to the gaseous flamelets where the fuel is in a gaseous form. Both are evaluated under a counterflow configuration and potential flow conditions where as a convention we name the left side of the configuration as ”fuel” side and the right one as ”air” side as it is shown in the following figure 3.1. In the ”air” side of the configuration, a pure oxidizer is introduced for any case. On the other hand, in the ”fuel” side pure gaseous ethanol enters for the gaseous flamelets, while spray ethanol surrounded by oxidizer (carrier gas) enters for the spray flamelets.

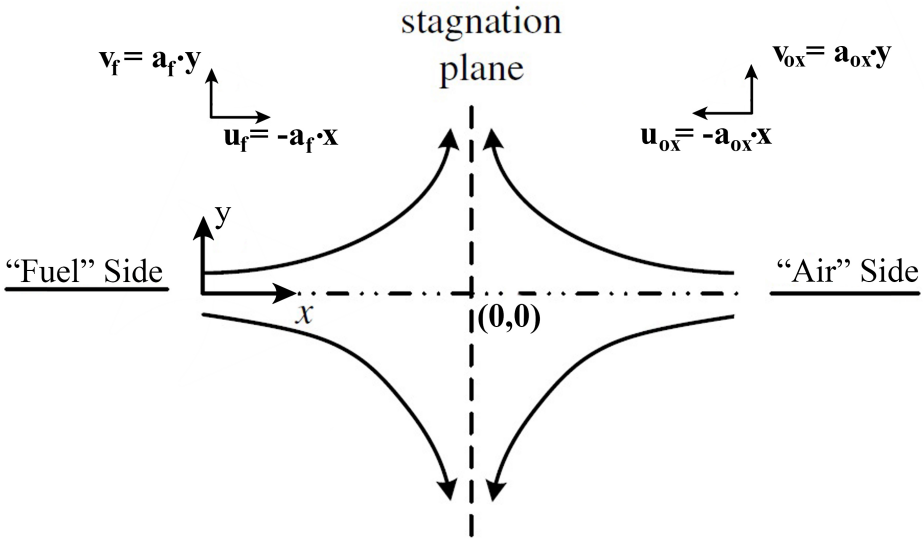

Figure 3.1: Counterflow configuration between fuel and oxidizer streams

The oxidizer that is used in any case is a hot coflow of combustion products that contains low oxygen level and its composition is obtained from the Delft Spray-in-Hot-Coflow (DSHC) dataset. The DSHC burner has been designed in the University of Technology of Delft to study the fundamental aspects of MILD combustion of light oils [10]. In brief, the DSHC burner is consisting of two burners, where the primary one refers to the combustion of ethanol spray while the secondary one refers to the creation of hot-diluted coflow combustion products to be used as oxidizer in the primary burner. The secondary burner operates on premixed air and Dutch Natural Gas (DNG). By varying the air/DNG ration, different coflow temperatures and compositions can be obtained. In the PhD-thesis work of Likun Ma [2] different coflow compositions are described, but for this report only one is considered indicated as Hii and its temperature/composition is shown in the table 3.1.

In order to execute a single simulation, the user has to build a corresponding case for which three main directories have to be created: a) a ”system” directory in which the user controls the duration of the simulation and also selects the numerical schemes for the calculation of the discretization process, b) a ”constant” directory where properties of the fluids regarding

Table 3.1: Temperature and mass fraction composition of the oxidizer stream (hot coflow) [2]

Case	T [K]	Y_{O_2}[-]	Y_{N_2}[-]	Y_{H_2O}[-]	Y_{CO_2}[-]
Hii	1400	0.1	0.74	0.07	0.09

thermodynamics, chemistry, turbulence and others are set and also under the sub-directory ”polyMesh” instructions for the generation of the mesh are given and finally c) the time directory, which is simply named as ”0” if the simulation starts at a time 0 sec, where the essential initial and boundary conditions need to be specified for selected variables. The structure of the directories of a case is indicated in the figure 3.2 and the directories are explained in more detail in the following paragraphs.

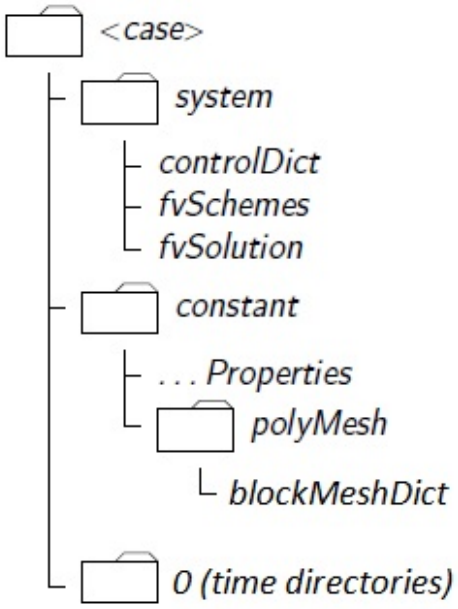

Figure 3.2: Structure of the case’s directories

3.4.1. Mesh Generation

To begin a numerical calculation of a case, the first step is to generate an appropriate mesh. Under the directory ”constant/polyMesh/blockMeshDict” (figure 3.2), the user can specify the entries required to generate a mesh. OpenFOAM always operates in a three dimensional Cartesian coordinate system and all geometries are generated in three dimensions. Here, the geometric domain in which the mesh will be generated will be of the cubic shape, where its vertices coordinates are set so that its edges along the x and y direction expand from -0.02m to +0.02m while the corresponding edges to the z direction expand from -0.01m to +0.01m. The number of cells along each of the three directions (x,y,z) is set as (100,100,1).

For the next step, the boundary surfaces of the cube are defined by giving them characteristic names in a way that they reflect physically a counterflow flame where on the left and right side, the fuel and oxidizer stream are located respectively and the combustion products leave the domain from the top and the bottom in a potential flow manner. As a result, the left

surface of the cube that is normal to negative x-axis is named as ”fuel”, the opposite one and normal to the positive x-axis as ”air”, the upper and the lower one both fall under the boundary name ”outlet” and the last two cubic surfaces found normal to the z-axis are both set as ”frontAndBack”.

For this kind of counterflow problem, a two-dimensional calculation is the aim, but by default OpenFOAM solves any case in three dimensions. For that reason, by specifying the ”frontAndBack” boundary with the condition ”empty;”, any calculation normal to it (along the z-axis) will be omitted. In that way the solver is instructed to solve in two directions, the x-y plane. If no mistake has been done by the user, the mesh will be generated by typing the keyword ”blockMesh” in the terminal.

3.4.2. Boundary and initial conditions

The solver that is used in this project is transient (unsteady) and has to deal with the set of the continuity, momentum, energy and species mass fraction transport equations numerically. To do so, it requires a set of boundary conditions (Dirichlet, Neumann) in space and an initial condition (”initial guess”) for the internal field for a set of variables (pressure, velocity, temperature, species). All these conditions should be given in the directory ”0” of the case (figure 3.2).

The following tables 3.2 and 3.3 present all the initial and boundary conditions that need to be applied in a set of characteristic variables so that the solver can start performing iterations. In every case these conditions refer exclusively to the gas phase and the boundary conditions for the spray phase are set in a separate directory which will be discussed later.

Table 3.2: Spray flamelets, Initial and Boundary conditions (for the gas phase)

Spray Flamelets (only the gas phase)					
Variables/Surfaces	fuel	air	outlet	internalField	frontAndBack
P [Pa]	zeroGradient	zeroGradient	totalPressure	10^5	empty
T [K]	1400	1400	inletOutlet	300	empty
Y_{O_2} [-]	0.099045	0.099045	inletOutlet	0	empty
Y_{N_2} [-]	0.744357	0.744357	inletOutlet	1	empty
Y_{H_2O} [-]	0.069977	0.069977	inletOutlet	0	empty
Y_{CO_2} [-]	0.086622	0.086622	inletOutlet	0	empty
$Y_{C_2H_5OH}$ [-]	0	0	inletOutlet	0	empty
U [m/s]	$(-a_{ox} \cdot x, a_{ox} \cdot y, 0)$	$(-a_{ox} \cdot x, a_{ox} \cdot y, 0)$	pressureInletOutletVelocity	(0, 0, 0)	empty

For both the spray and the gaseous flamelets cases the front and back surfaces are imposed as ”empty” to instruct the solver for a two-dimensional calculation. Except for the conditions in the ”fuel” side the two cases elsewhere have identical conditions. The keywords ”inletOutlet”, ”totalPressure” and ”pressureInletOutletVelocity” are applied in the boundary ”outlet” and for an outflow they imply a zero gradient condition, a fixed value condition (the value of internal field) and a zero gradient condition respectively.

For the spray cases, ethanol in liquid form is carried by hot coflow in the ”fuel” side and since we specify only the gaseous conditions at this point, this is the reason why ”fuel” and ”air”

Table 3.3: Gaseous flamelets, Initial and Boundary conditions

Gaseous Flamelets					
Variables/Surfaces	fuel	air	outlet	internalField	frontAndBack
P [Pa]	zeroGradient	zeroGradient	totalPressure	10^5	empty
T [K]	352	1400	inletOutlet	300	empty
Y_{O_2} [-]	0	0.099045	inletOutlet	0	empty
Y_{N_2} [-]	0	0.744357	inletOutlet	1	empty
Y_{H_2O} [-]	0	0.069977	inletOutlet	0	empty
Y_{CO_2} [-]	0	0.086622	inletOutlet	0	empty
$Y_{C_2H_5OH}$ [-]	1	0	inletOutlet	0	empty
U [m/s]	$(-a_f \cdot x, a_f \cdot y, 0)$	$(-a_{ox} \cdot x, a_{ox} \cdot y, 0)$	pressureInletOutletVelocity	(0, 0, 0)	empty

side have the same boundary conditions in table 3.2. Gaseous flamelets on the other hand resemble a typical counterflow diffusion flame. Hence, pure ethanol vapor (boiling temperature ≈ 351.52K) is introduced in the ”fuel” side for that case. Finally, concerning the velocity, for the counterflow configuration (see figure 3.1) and the formation of a stagnation point approximately in the middle of the domain, posing the two inlets ”fuel” and ”air” side sufficiently away (streamlines should be parallel close to the center line of the domain), a potential flow boundary condition can be applied since the flow is irrotational. Thus, the two components of velocity in the ”air” side are set as:

$$u_{ox} = -a_{ox}x, \quad v_{ox} = a_{ox}y \tag{3.1}$$

where a_{ox} denotes the strain rate acting on the oxidizer flow and needs to be specified by the user as a boundary condition. Then the respective strain rate on the ”fuel” side a_f can be found as $a_f = a_{ox}\sqrt{\rho_{ox}/\rho_f}$, derived by a straight application of Bernoulli’s equation between the ”air” and the ”fuel” side for an inviscid, incompressible flow with no body forces (the flow can be considered as such, by posing the inlets far from the the stagnation point and the reaction zone). We remark here that for dilute spray conditions, the contribution of the incoming droplets to the dynamic pressure can be neglected.

3.4.3. Spray Boundary Conditions

The boundary conditions for the discrete phase, the spray, are set exclusively in a separate directory located in ”constant/sprayCloudProperties” (figure 3.2). Thus, under the block ”sprayCloudProperties/constantProperties” the initial temperature of the ethanol spray is given as 300K, lower than its atmospheric boiling temperature which is 351.52K. This means that heat should be provided first, so that the ethanol droplets reach a saturation condition at which ethanol vapor fuel is released. Setting also in the same code-block the boolean variable ”constantVolume” as ”false;”, we declare that the volume of each and every droplet is time variable.

Following, under the block ”sprayCloudProperties/subModels/particleForces” we can specify the nature of the forces that any droplet will experience. Hence, we add the entry ”sphereDrag;” which indicates that the drag force is under consideration (see equation (2.71)). This specific keyword automatically calls the code that is located in the source code of the solver ”sprayCFoam” and under the directory path ”sprayCFoam/src/lagrangian/intermediate/ submodels/Kinematic/ParticleForces/Drag/SphereDrag” (since the solver ”sprayCFoam” is a refor-

mation of the original precompiled ”sprayFoam” the code paths are the same for both solvers and as a consequence the reader can also refer to [51], where the original code is located, in order to have a direct inspection of the code).

In the same directory and under the block ”injectionModels”, the user specifies the type of the injection and its different aspects as shown in the following table:

Table 3.4: Injection Model

type	patchInjection;
SOI	0.0;
massTotal	0.0005;
patchName	fuel;
U0	(10 0 0);
massFlowRate	0.00025;
duration	2;
parcelsPerSecond	3100000;

The first entry in the table 3.4, ”patchInjection;” refers to the type of injection and calls for the code that is located in ”sprayCFoam/src/lagrangian/intermediate/submodels/Kinematic/InjectionModel/PatchInjection” [51]. The start-up of the injection is declared in the ”SOI” field and the total mass of the spray to be injected in kg is specified under the ”massTotal”. In turn, in order to define the location of the injector, the user specifies in which boundary or patch of the domain it should be placed. We want the injector to be on the fuel side of the domain, so the field ”patchName” is set to ”fuel;”. We should mention here that this type of injection distributes the droplets randomly along the patch. Subsequently, an initial axial velocity is given to droplets and as well the mass flow rate (kg/s) and the duration (sec) are specified. Finally, the number of the parcels to be injected per second must be set. Usually, in a spray injection the droplets initially have different characteristics (droplet size, velocity) and so the meaning of parcel is that it represents groups of droplets with identical characteristics (initial droplet and velocity). In this project, all the droplets in a single simulation are calculated, having same characteristics initially, and we can say that simply a parcel is equivalent to a droplet and thus we can set the number of droplets per parcel as one. To calculate the number of parcels per second we make the following derivation:

A = number of droplets per parcel
B = mass per parcel
C = mass per droplet
D = mass flow rate
E = number of parcels per second

$$A = \frac{B}{C} = \frac{\frac{D}{E}}{\rho_p \frac{4}{3}\pi r^3} = \frac{3D}{\rho_p 4\pi r^3 E} \tag{3.2}$$

Then solving for the number of parcels per second (E) and posing A=1 in the above equation we end up with:

$$E = \frac{3D}{\rho_p 4\pi r^3} \tag{3.3}$$

The implementation of the settings for the injector proceeds via the definition of the diameter of the droplets. To do so, under the block ”sizeDistribution” we enter for example the command ”value 100e-6;” to refer to droplets of initial diameter 100μm. Finally, we need to declare the models that will be used for the heat transfer and the phase change of the discrete phase. Thus, the solver is instructed accordingly by posing the following commands ”heatTransferModel RanzMarshall; ” and ”phaseChangeModel liquidEvaporationBoil;”. In those commands, the left part consists a keyword and the right part an entry. In turn, the entries direct the solver to the source code located at ”sprayCFoam/src/lagrangian/intermediate/submodels/ Thermodynamic/HeatTransferModel/RanzMarshall” and ”sprayCFoam/src/lagrangian/intermediate/ submodels/Reacting/PhaseChangeModel/LiquidEvaporationBoil” [51] respectively. In the ”RanzMarshall” model, the equation for the Nusselt number (2.79) is implemented. In addition, in the ”LiquidEvaporationBoil” model, first the formation of the Sherwood number equation (2.80) is given and subsequently the time rate of change of the mass of the droplet (2.78) is provided. Finally, as it was described in the previous chapter and from equation (2.84) a correction for the Nusselt number has to be applied to account for the change in the heat and mass transfer processes due to the Stefan’s flow effects and the increase of the boundary layer of the droplet. Therefore, the boolean variable ”BirdCorrection” is set to ”true;” and the source code for this correction can be found under ”sprayCFoam/src/lagrangian/intermediate/submodels/ Thermodynamic/HeatTransferModel/HeatTransferModel” [51].

3.4.4. Physical Properties

The physical properties that concern the chemistry, thermodynamics, combustion and the turbulence of a case are stored in directories with representative names under the directory ”constant” (figure 3.2).

Table 3.5: thermophysicalProperties

mixture	reactingMixture;
transport	sutherland;
thermo	janaf;
energy	sensibleEnthalpy;
equationOfState	perfectGas;

Firstly, in the directory ”constant/thermophysicalProperties”, a thermophysical model is constructed in OpenFOAM as a pressure-temperature (p−T) system from which other properties are computed [50]. Under the sub-directory ”thermoType”, the package of thermophysical modelling that is used in the simulation is specified and is shown in the table 3.5. The entries followed by semicolon refer to models that come as a large set of pre-compiled C++ codes. During simulation, reactions take place and the composition of the mixture is not constant and this is specified in the directory as ”mixture reactingMixture;”.

Information about the different species that consist the mixture and their reactions are listed in a separate directory ”constant/chemkin” and are being called respectively in the ”thermophysicalProperties” directory by the commands: «$CHEMKINThermoFile ”FOAM_CASE/chemkin/therm_C2H5OH.dat”;» and «CHEMKINFile ”$FOAM_CASE/chemkin/chem_C2H5OH_Marinov.inp”;».

The next entry, ”sutherland;”, regards the transport modelling which concerns the evaluation of the dynamic viscosity [50]. Thus, the dynamic viscosity is calculated by a Sutherland type equation as a function of temperature. In order to calculate the specific heat C_p, the enthalpy and the entropy we choose the ”janaf;” model in which these properties are calculated from polynomials as a function of temperature and a set of coefficients taken from NASA thermodynamic files. These coefficients are stored for every case in ”chemkin/therm_C2H5OH.dat”. For each species, two sets of seven coefficients are stored, where the first set corresponds to the temperature range 1000K-3500K and the second one to the range 200K-1000K. As a next step, the user has to select the form of energy to be used for the calculation of the properties of the mixture, either in the form of internal energy or enthalpy and even with the enthalpy of formation to be included or not. This choice is specified through the ”energy” keyword. We refer to absolute energy when heat of formation is included, and sensible energy when it is not (equation (2.44)). We have selected here to deal with the sensible enthalpy. Finally, an equation of state has to be chosen and as we mentioned in the previous chapter we will make use of the perfect gas equation (2.45) and this corresponds to the ”perfectGas;” entry.

The chemkin/therm.dat files refer only to gaseous properties. For the spray flamelets where we have presence of liquid ethanol, an additional block under the directory ”thermophysicalProperties” should be present with the name ”liquids” in which the liquid components that are present in our simulations should be declared, so for our case we simply type there ”C2H5OH”. This declaration will make a connection to the header and source code files ”C2H5OH.H” and ”C2H5OH.C” located at ”OpenFOAM-2.3.x/src/thermophysicalModels/properties/ liquidProperties/C2H5OH/” [51]. The properties of the liquid component (density, specific heat, viscosity etc.) are calculated from polynomials correlations whose constants-coefficients are found in ”C2H5OH.C”. The file ”C2H5OH.H” calls for each and every property the corresponding NSRDS (National Standard Reference Data Series) functions that are stored in ”OpenFOAM-2.3.x/src/thermophysicalModels/thermophysicalFunctions/NSRDSfunctions/” [51], where those polynomial correlations are implemented. Finally, as we mentioned earlier, the reactions between species are stored in the directory ”chemkin/chem_C2H5OH_Marinov.inp” for every case. Briefly, we can say that this file contains a detailed chemical kinetic model (including 57 species and 383 intermediate chemical reactions) for ethanol oxidation that has been developed and validated by Nick M. Marinov [52]. This file provides for each reaction the three coefficients (A_{fj}, β_j, E_j) that are essential to implement the forward coefficient according to the Arrhenius law (2.55).

The way or the algorithm to be followed in order to calculate the chemical source terms $\dot{\omega}_k$ in equation (2.52) is defined under the directory ”constant/chemistryProperties”. Here, we instruct the solver to follow for that purpose an Euler-implicit scheme with the command ”chemistrySolver EulerImplicit;”. The equation (2.52) can be written in an algebraic form as:

$$\dot{\omega}_k = S_{k1}Q_1 + S_{k2}Q_2 + S_{k3}Q_3 + \ldots + S_{kM}Q_M \tag{3.4}$$

where k refers to a single chemical species, M is the total number of chemical reactions and each term refers to one reaction. S_k is the stoichiometric coefficient of species k in a reaction

and Q is the rate of progress of a reaction. We can rewrite the final expression in a matrix transformation form:

$$\dot{\omega}_k = \begin{bmatrix} S_{k1} & S_{k2} & S_{k3} & . & . & . & S_{kM} \end{bmatrix} \begin{bmatrix} Q_1 \\ Q_2 \\ Q_3 \\ . \\ . \\ . \\ Q_M \end{bmatrix} \tag{3.5}$$

If we write all the chemical source terms for all the species N as a column vector, $\dot{\omega}$, we get:

$$\dot{\omega} = \begin{bmatrix} \dot{\omega}_1 \\ \dot{\omega}_2 \\ \dot{\omega}_3 \\ . \\ . \\ . \\ \dot{\omega}_N \end{bmatrix} = \begin{bmatrix} S_{11} & S_{12} & S_{13} & . & . & . & S_{1M} \\ S_{21} & S_{22} & S_{33} & . & . & . & S_{3M} \\ S_{31} & S_{32} & S_{33} & . & . & . & S_{3M} \\ . & & & & & & \\ . & & & & & & \\ . & & & & & & \\ S_{N1} & S_{N2} & S_{N3} & . & . & . & S_{NM} \end{bmatrix} \begin{bmatrix} Q_1 \\ Q_2 \\ Q_3 \\ . \\ . \\ . \\ Q_M \end{bmatrix} \tag{3.6}$$

Finally, $\dot{\omega}$ is discretized temporally and the vector $[Q]$ is kept in the new time moment to create the Euler-implicit scheme. Moreover, in the directory "constant/chemistryProperties" we need to specify an initial chemical time step and we do so with the command "initialChemicalTimeStep 1e-07;". The chemical time scales are shorter than those of the flow whose time step is of the order 1e-05 or 1e-06. We chose it as 1e-07. Also, the chemical time scale should be sufficiently low, since each reaction presents its own chemical time scale or response in a numerical calculation and hence we need to capture also the more retarded reactions, otherwise the calculation will blow up. The chemical time steps that will follow, are calculated in OpenFOAM by the formula $\delta t_c = cTauChem * \tau_c$, where $\tau_c = [X_k]/[X_k]'$ [53] and $[X_k]'$ is the time derivative of the molar concentration and the constant is set as "cTauChem 1;" by default. Lastly, since we are dealing with laminar calculations, under the directory "constant/turbulenceProperties" we instruct the solver accordingly by setting the command "simulationType laminar;".

3.4.5. Control

The user can control a case by formatting appropriately the directory "controlDict" which is located under the main directory "system" (see figure 3.2). There, the start and stop time and the time step as well can be set. For the cases here, any simulation starts at the instance of 0 sec, obtaining all the boundary/initial conditions from the "0" directory that we described before. Their end time is set as 2 sec, since it is observed that then all the cases have already reached a steady state condition.

As for the time step, it is set to be adjustable, provided that the Courant number is always below one in order to achieve temporal accuracy and numerical stability. The Courant number is defined as, $Co = \delta t|V|/\delta x$, where δt is the time step, δx is the size of the cell and $|V|$ is the magnitude of the velocity through the cell. Specifying a value for the Courant number in the keyword "$maxCo$" of the directory, the respective time step can be calculated explicitely as it

is shown in equation (3.7). Usually, lower values of the order of 0.6 are selected at the begin of the simulation where the calculation is highly transient and higher values approaching 0.9 can be used at a later time when the calculation is somewhat stabilized.

$$\Delta t^{(n+1)} = min\left(\frac{maxCo \cdot \Delta x(i)}{|V^{(n)}(i)|}\right) \tag{3.7}$$

As the simulation progresses we wish to record the results at certain intervals of time that we can later view with a post-processing package. Specifying the ”writeInterval” as 0.1, the results will be written every after 0.1 sec. OpenFOAM will create a time directory named by the current time step and including the results for all the fields.

3.4.6. Discretization and numerical schemes

All the spatial derivative terms in the fundamental partial differential equations need to be discretized. Most of the commercial and open CFD packages are based on the Finite Volume Method (FVM) and the same holds for OpenFOAM. Additionally, a temporal discretization needs to be applied for the unsteady terms.

The finite volume method transforms the set of partial differential equations into a system of linear algebraic equations [54–56]. According to this method the domain is subdivided into a number of finite volumes (FV) by generating appropriate mesh and the method is typically done in two basic steps: a) In the first step the partial differential equations (PDEs) that describe the combustion problem are integrated and transformed into integral balance equations over a FV of the mesh. Subsequently, the sum of surface and volume integrals terms is changed into discrete algebraic relations over a finite volume and its surfaces. Then, for a quantity φ its transport equation for a single cell and neglecting temporal terms can be simply written as:

$$\sum_{f=1}^{N} \left(\rho V \varphi - \Gamma_\varphi \nabla \varphi\right)_f \cdot \mathcal{S}_f = (Q_\varphi \mathcal{V})_C \tag{3.8}$$

where f refers to the faces of a cell, φ is the property that needs to be calculated, $\mathcal{S}$ is the vector normal to a surface, $\rho V \varphi$ is the convective term, $\Gamma_\varphi \nabla \varphi$ is the diffusive term and $(Q_\varphi \mathcal{V})_C$ is a volumetric source term over the cell C. b) In the second step, since values of the property φ are required at the faces of the cell in (3.8), interpolation profiles need to be chosen to approximate the variation of the property within the cell and relate the surface values of the property to its neighbouring cell-centred values and thus transform the algebraic relations into algebraic equations.

In the directory ”system/fvSchemes” (figure 3.2) of every case, the user can assign the type of finite volume discretisation schemes for each and every term contained into the partial differential equations. Thus, the temporal terms (”ddtSchemes”) are treated using the first order-implicit-forward-Euler scheme. The gradient terms (”gradSchemes”) are discretized by the ”Gauss linear” scheme. The ”Gauss” entry refers to the requirement for the interpolation of values from cell centres to face centres. The second entry ”linear” demands for a linear interpolation, where a quantity in the face is calculated from the nodes of the adjacent cells. The divergence terms (”divSchemes”) are treated similarly by a Gaussian integration. However, convective divergence terms are treated with a first-order upwind scheme,

while non-convective divergence terms with a second-order linear (central difference) scheme. Laplacian terms (”laplacianSchemes”) represent diffusion phenomena and they are discretized by the Gaussian linear (central difference) scheme.

As a conclusion we can say that for diffusive terms, central difference (linear profiles) is a good approximation since it is a second order scheme and hence very accurate. However, central difference is weak regarding boundedness and stability when it has to deal with convective terms and it is prone to oscillations. The advection process is a highly directional process transporting properties only in the direction of the flow. Therefore the linear profile approximation (central difference), which assigns equal weight to both the upwind and downwind nodes, cannot describe the directional preference of convection. Posing equal weights to the two nodes sharing the face of a cell with no directional preference is appropriate for non-directional phenomena such as the diffusion term. A scheme that is more compatible with the advection process is the upwind scheme. In regions where diffusion dominates the upwind scheme is not as accurate as central differencing, because the upwind profile is first order accurate while the linear profile is second order accurate. At highly convective flows, the central difference scheme is unstable as its solution is unbounded and physically incorrect, while the upwind scheme might not be particularly accurate, but it is physically correct since it introduces an extra diffusion term (numerical diffusion) making the scheme more stable. Thus, between the two schemes it appears to be a trade-off between accuracy and stability and it is recommended that central difference schemes to be used for diffusive terms, while upwind schemes to be used for convective terms [54].

Following the two before-mentioned steps of the discretization process for each and every cell of the grid , we obtain a system of linear equations of the form $A\varphi = b$. The property φ consists of a column vector and represents the values of the property that is under consideration in the centre of each and every cell, is unknown and needs to be calculated. In this system, the coefficients of the unknown variables constituting the matrix A are the result of the linearization procedure and the mesh geometry, while column vector b contains all sources, constants, boundary conditions, and non-linearizable components. Techniques for solving linear systems of equations are generally grouped into direct and iterative methods [54]. In fluid dynamics problems, the number of cells is usually vast leading to a proportional matrix A of high dimensionality. For these cases, the direct methods are prohibitive, since they require the calculation of the inverse of the matrix A and then use Gaussian elimination, a process that is computationally very expensive requiring large memory.

On the other hand, iterative methods are more appropriate for those applications. This category includes simple methods but of lower convergence rate such as the Jacobi and the Gauss-Seidel methods. In this project and under the directory ”system/fvSolution” the more complicated but of higher rate of convergence method, the Preconditioned Conjugate Gradient (PCG) method to calculate variables that form symmetric matrices of transformation like pressure is used and the Preconditioned Bi-Conjugate Gradient (PBiCG) method which is similar to the PCG method but additionally uses a dummy variable to deal with asymmetric matrices is used for the case of the velocity calculation [50, 54]. Solvers that are based on iterative methods, they focus on reducing the equation residual over successive solutions. The residual after the n-th iteration step is defined as $r^{(n)} = b - A\varphi^{(n)}$ and should not be confused with the error (e) which is defined as the difference of the solution at an iteration level with the actual solution and can be written as $e^{(n)} = \varphi^{(n)} - \varphi$. The residual can be seen as a measure of accuracy, meaning that the smaller it is the more accurate is the solution. For that reason in the ”system/fvsolution” directory the tolerance of the solver is specified as 10^{-6}, which means

that when the residual drops below the specified tolerance the solver will stop.

In the directory ”system/fvSolution”, the PIMPLE algorithm is called in order to couple the velocity and the pressure. This algorithm is a combination of the SIMPLE and the PISO algorithms. According to the SIMPLE algorithm [57], a guess value for the pressure is assigned to the gradient pressure term in order to solve the momentum equation. Nevertheless, the resolved velocity field does not satisfy the continuity equation and as a result a pressure correction needs to be considered. The velocity field that was found, together with the pressure correction are introduced into the continuity equation to form a Poisson equation for pressure. The density is provided by the equation of state and the continuity equation can be solved then to give the correct pressure. Finally, the corrected pressure is introduced to the momentum equation to obtain the new velocity field. This is the basic idea behind the SIMPLE algorithm and based on that the PISO algorithm [58] introduces an additional (or more) second pressure correction as an extra step, so that the Poisson and momentum equations are solved twice. PISO, in contrast to SIMPLE, is adopted by transient solvers and so instead of a guess value for the pressure that is assigned in the SIMPLE case, here the pressure found in the previous time step is used as an initial guess. Then the PIMPLE algorithm [50] comes as an extension of the PISO, giving the opportunity to the user to select the number of times that the PISO algorithm will be executed in a single time step. For this project and under the directory ”system/fvSolution/PIMPLE”, two pressure corrections are used by specifying ”nCorrectors 2;”, while the PISO algorithm is selected to be executed only once in a single time step by specifying ”nOuterCorrectors 1;”.

3.5. Overview of cases

After having described the necessary steps that need to be followed in order to start the calculation of a case, in this section we present the overview of the cases that are calculated in this project for a variation of selected variables. Having fixed the necessary boundary conditions in the way that they were described previously, for the calculation of the set of gaseous flamelets two variables are responsible for the determination of the local flame structure, the mixture fraction and the strain rate (or scalar dissipation rate). The discretization and the solution of the differential equations in this project is done in the physical space and so a transformation in the mixture fraction space remains to be done as a post-processing step and will be described in the following section. On the other hand, strain rate is related to the velocity components according to (3.1) for a potential flow and is a free variable, meaning that the user is allowed to give any value from very low reaching to-close-to adiabatic temperatures till very high leading to extinguishing or pure mixing flamelets. Finally, we are in a position to create the database where any variable (e.g mass fractions and temperature) can be stored as a function of the two indices, the mixture fraction and the strain rate. For that reason, we simply call this database a two dimensional library.

When it comes to deal with the spray flamelets though, the number of indices of the database is larger. Indeed, as it is also reported by H. Olguin et al. [47], apart from the mixture fraction and the strain rate also the initial droplet diameter d_p, the velocity of the droplets V_p and the equivalence ratio Φ on the ”fuel” side of the configuration can affect the flame structure of the flamelets. As a result, for the spray cases we end up with a five dimensional flamelet library. In the following table 3.6 the values of those variables that were kept for different simulations are shown:

Table 3.6: Variables range for different cases

Flamelets	z [-]	a_{ox} [1/s]	Φ [-]	d_p [μm]	V_p [m/s]
Gas	0 to 1	55, 300, 500, 800	-	-	-
Spray	0 to 1	55, 300, 500, 800	1, 3	40, 60, 80, 100	$V_p = V_{ox}$

As we can see from the table 3.6, four different values for the strain rate in the oxidizer side have been chosen and this means that we have four different cases for the gas flamelets library. On the other hand, for the spray flamelets, apart from the same four values for the strain rate, two values have been chosen for the equivalence ratio (Φ) and four different values for the initial diameter of the droplets. The variables for each case are changed alternatively in sequence and this gives us a total of 2x4x4=32 different spray flamelet cases. The equivalence ratio is set on the fuel side of the configuration and for the gaseous flamelets has no physical meaning. Regarding the droplets velocity, for this project, a non-slip condition between the carrier gas and the droplets is chosen and thus in the boundary of each case we pose $V_p = u_{ox}$ where u_{ox} is the axial boundary velocity of the oxidizer (see equation (3.1) and figure 3.1).

3.6. Post-processing

Having done all the necessary before-mentioned steps: generation of the mesh, setting the controls, selection of the numerical schemes and physical properties and adapting the solver of the differential equations, we can start running the simulation by letting the two opposing streams to develop, gradually mix with each other and eventually burn till they reach a steady state. At this point we can stop the simulation and move on to the post-processing part where we need to collect the results and manipulate them accordingly so that we get valuable graphs indicating the influence of the different parameters that vary from case to case.

The first step of post-processing usually is to reassemble the decomposed fields and mesh because the calculation most of the times occurs in a parallel processing computation. This is a common practice of decomposing the domain in which the geometry and associated fields are broken into pieces and allocated to separate processors for solution in order to reduce the computational time. The utilities for the decomposition and the restruction of the fields are respectively the ”decomposePar” and ”reconstructPar”. The user has the option to reconstruct the results for any time moment of the simulation. Usually, the latest time moment or few of the latest ones are reconstructed since the steady state solution is reached. Of course, if ignition or extinction phenomena are to be studied then also unsteady solutions are to be captured. Then, OpenFOAM will create in the case directory respective time sub-directories similar to ”0” one that will contain all the resolved variables for the whole domain. As a next step, the user can launch the case’s directories and data on Paraview, the post-processing tool supplied with OpenFOAM.

The launched data are of the two dimensional calculation and since we want to resemble the simulation of a one dimensional flamelet, as a next step, we need to extract the data of the calculation in the center line along the x-axis of the domain, by specifying two points (-0.02,0,0) and (0.02,0,0) that define a line. In Paraview, we use the utility ”Plot Over Line” that gives the graph of any variable along this line. Then, we also have the option of creating a ”Spreadsheet View” where the data are stored in a table and can be easily launched in a Matlab or Excel tool for further post-processing. For the gaseous flamelets the latest time

moment is chosen to be post-processed in Paraview, while for the spray flamelets the latest 10 time moments (after combustion is fully developed) are used and are post-processed by using a time average utility of Paraview ("Filters/Temporal/Temoral Statistics"). The reason for this choice is that the injector, as already mentioned, has the characteristic that it places the droplets at random positions along the "fuel" side surface at every time step, introducing so a sort of randomness in the boundary conditions. By averaging ten consecutive samples, we make sure that the final averaged solution is independent of this kind of randomness. Of course, the more samples one is averaging the more independent of the random distribution is the mean value. However, a trade-off between accuracy and allocation of memory and post-processing time should always be considered. As a remark, we can say that this randomness is damped as the equivalence ratio is increased and/or the initial droplet's size is decreased giving a denser cloud of droplets. The droplets' lagrangian properties are captured for the latest time step and since no droplets can be found at the exact location of the center-line axis, we capture the droplets that are located in a range of $\pm$ 0.001m away.

Loading all the Lagrangian and Eulerian fields in Matlab, we can easily plot the evolution of characteristic variables in the physical space along the x-axis. These graphs already can give us, as we will see in the following chapter, valuable results that can be further discussed and bring us to solid conclusions regarding the effects of the variation of those parameters in the flame structure. More importantly, we we will be in a position to understand the influence of the evaporation process and the motion of the droplets in the flame structure. As a further post-processing step and in order to implement the idea of the flamelet library, the results should be transferred from the 1D physical space to the 1D mixture fraction space.

As it is reported in [59], this can be done by using for the gas phase the local elemental mass fractions of hydrogen and carbon in the following formula:

$$z(i) = \frac{0.5(Y_H(i) - Y_{H_{ox}})/W_H + 2(Y_C(i) - Y_{C_{ox}})/W_C}{0.5(Y_{H_f} - Y_{H_{ox}})/W_H + 2(Y_{C_f} - Y_{C_{ox}})/W_C} \tag{3.9}$$

where the subscripts H, C refer respectively to the elements of hydrogen and carbon, whereas ox and f to the oxidizer and fuel side and W_H, W_C are the atomic mass of the two elements. The formula (3.9) calculates at every node (i) of the center line the local mixture fraction value. Thus, these values can be stored in a new table and used as a new coordinate replacing the (x,y,z) ones.

The formula (3.9) can be used for the gaseous flamelets where the minimum and maximum values of the elemental mass fractions Y_H and Y_C are located at the oxidizer and fuel side respectively to keep the monotonicity of mixture fraction (1 at the fuel side, 0 at the oxidizer side). However, for the spray flamelets where initially there is no fuel vapor, formula (3.9) is not applicable and a more general formula proposed by H. Olguin et al. [47] can be used instead:

$$z(i) = \frac{0.5(Y_H(i) - Y_{H,min})/W_H + 2(Y_C(i) - Y_{C,min})/W_C}{0.5(Y_{H,max} - Y_{H,min})/W_H + 2(Y_{C,max} - Y_{C,min})/W_C} \tag{3.10}$$

where max, min express the maximum and the minimum of the elemental mass fractions along the center line of the domain for which we take the samples. We note here, that for the gaseous flamelets, equations (3.9) and (3.10) give the same results. The local elemental mass fraction of an element (e) at a node (i) can be found from the following relation:

$$Y_e(i) = \sum_{j}^{k} Y_k(i) \frac{\alpha_{k,e} W_e}{W_k} \tag{3.11}$$

where e refers either to H or C, Y_k is the species k local mass fraction, $\alpha_{k,e}$ denotes the number of moles of element e in species k, and W_e and W_k denote the molar mass of element e and of species k, respectively.

3.7. Particle Tracking

The way of finding the position of a droplet is by writing equation (2.70) in a temporally explicit discretized form and solving for the position at the new time step:

$$x_p^{(t+\Delta t)} = \Delta t V_p^{(t)} + x_p^{(t)} \tag{3.12}$$

Moreover, we can find a droplet's velocity by applying the second Newton's law combined with the relation (2.71) and writing in a temporally dictretized form:

$$\Sigma F = m_p \frac{V_p^{(t+\Delta t)} - V_p^{(t)}}{\Delta t} = m_p \frac{V_{seen}^{(t)} - V_p^{(t+\Delta t)}}{\tau_p} + m_p g \tag{3.13}$$

rearranging accordingly the terms we obtain:

$$V_p^{(t+\Delta t)} = \frac{V_p^{(t)} + \frac{\Delta t}{\tau_p} V_{seen}^{(t)} + \Delta t g}{1 + \frac{\Delta t}{\tau_p}} \tag{3.14}$$

We should note here that Δt is the Lagrangian time step and refers to the motion of the droplet. Refering to the continuous phase, we name the Eulerian time step as dt. Here, we can distinguish two scenarios. In the first one, a droplet found in the position A and in the cell1 at the initial moment of the eulerian time step dt, moves, and at the end of the dt is still in the cell1 at a position B without hitting any of its faces. For this case, we take $\Delta t = dt$ (dt is known from equation (3.7)) and the new velocity and position of the droplet can be updated according to equations (3.14) and (3.12).

In the second scenario, we consider the case where a droplet at the end of the Eulerian time step dt, has crossed one of the faces of the cell1 and is found in an adjacent cell2. For this case, the moment that the droplet hits the face of the cell the Lagrangian time step is completed and the properties of the droplet have to be updated. We call this completed Lagrangian time step as stepfraction, since it consists only a fraction of the Eulerian time step. Thus, the Eulerian time step has to be divided into two Lagrangian time steps, where the first (Δt_a) covers the motion of the droplet from its position A in cell1 till the face (say position F) and the second one (Δt_b) that covers from the position F till the position B in the cell2. As a result, the properties of the droplet have to be updated twice in a single Eulerian time step. In practice, a droplet can cross many cells during a dt and so the Eulerian time step is divided into a set of Lagrangian time steps that is specific to each particle [60]. We recall at

this point that V_{seen} is the velocity of the gas phase of the Eulerian frame and is calculated at the position of the droplet using interpolation between the neighbouring cells.

Tracking accurately the droplets provides the information to calculate their contribution on the source terms that are present into the differential equations of the gaseous phase. Taking for example the contribution of the droplet mentioned in the first scenario into the momentum equation we can write it as:

$$\frac{1}{\mathcal{V}_{cell1}\Delta t}\left(m_{P_B}V_{P_B} - m_{P_A}V_{P_A}\right) \tag{3.15}$$

where $\mathcal{V}_{cell1}$ is the volume of the cell1 in which the droplet relaxes for the Lagrangian time step Δt and for this scenario equals the Eulerian one dt. The velocities at two different positions inside the cell1 are also shown for which a non-constant mass of droplet is indicated due to the mass transfer effects. Attempting to write a similar expression for the second scenario, we see that the droplet interacts with both the volume of fluid located at cell1 and cell2 during a single Eulerian time step so the two contributions are as:

$$\frac{1}{\mathcal{V}_{cell1}\Delta t_a}\left(m_{P_F}V_{P_F} - m_{P_A}V_{P_A}\right), \quad \frac{1}{\mathcal{V}_{cell2}\Delta t_b}\left(m_{P_B}V_{P_B} - m_{P_F}V_{P_F}\right) \tag{3.16}$$

where Δt_a and Δt_b are the two Lagrangian steps for which it holds that $dt = \Delta t_a + \Delta t_b$. Based on that idea, similar expressions for the sources of mass or enthalpy can be extracted. Summing the contributions of each and every droplet that passed through a cell during an Eulerian time step, we can obtain the total source term indicated by S^v in the transport equations (2.63-2.66).

4

Results and Discussion

4.1. Introduction

In the previous chapters we discussed all the physical phenomena and the concepts underlying the spray combustion. We also presented different combustion models and we highlighted the significance and the flexibility of the Flamelet Generated Manifolds (FGM) method. Then in the third chapter, we described analytically the working procedure of this project, and we pointed out the necessity for the development of a series of gaseous and spray flamelets.

In this chapter we are going to present the results that come out from the numerical calculations of a set of both gaseous and spray flamelets. The gaseous flamelets are developed under a non-premixed counterflow configuration, where the two opposing streams diffuse towards to each other, mix in a thin layer at a stagnation plane and instantaneously burn. For those cases, hot coflow products at 1400K of low oxygen level (oxidizer stream) are opposed against ethanol gas of 352K (fuel stream). The details for the boundary and initial conditions of the gaseous flamelets are shown in table 3.3. The imposed strain rate in the inlet streams appears as a limiting parameter for the flame structure of a flamelet, variations of which may lead to ignition, fully burnt or even extinguishing flamelets.

On the other hand, as it is already discussed in the previous chapters, for spray flamelets where the fuel is provided as a cloud of droplets, additional parameters appear to be crucial for the viability, the development and the characteristics of the flame structure. Thus, apart from the strain rate also the initial droplets' size, the equivalence ratio between the spray and its carrier gas and their relative velocity are important parameters. Hot coflow products as previous are driven against the spray of ethanol (300K) which is carried also by hot coflow products. The boundary and initial conditions for the spray flamelets are shown in table 3.2 and the injector settings in table 3.4.

In the following sections we evaluate the importance of those parameters by varying them according to the table 3.6 for different cases. The results are discussed in an attempt to point out the main differences between the gaseous and spray flamelets. The purpose is to show and highlight the influences of the presence of the liquid droplets in the flame structure. Not only the motion but also the evaporation of the droplets is expected to affect the flame structure.

4.2. Validation of the model

The geometric configuration, the selection of mesh and the functionality of the solver to be used for the simulations in this project need to be validated first in order for the final results to be reliable. To do so, we accomplished two different sets of calculations in a counterflow configuration where methane is released on the one side and air on the other under atmospheric conditions as it is shown in the table 4.1, where a refers to the strain rate, ρ to density and the subscripts f, ox to the fuel and air side respectively. The first set of calculations was conducted by our model in OpenFOAM using the solver "le1reactingFoam" and the second one using the CHEM1D code developed and validated at the Eindhoven University of Technology [11].

Table 4.1: Conditions for the validation calculation

Side	Composition (by moles)	Temperature (K)	Strain Rate (1/s)
Fuel	100% CH_4	300	$a_{ox}\sqrt{\rho_{ox}/\rho_f}$
Air	21% O_2+79% N_2	300	a_{ox}=10

For the OpenFOAM model two different meshes were used, a coarser one using 100x100 number of quadratic cells and a more refined one with 300x300 cells. The idea is to evaluate the results obtained from OpenFOAM by comparing them with the CHEM1D model and decide first of all whether the solver and secondly the type of mesh can predict well the methane-air diffusion flame. The CHEM1D code is made to conduct one dimensional calculations for diffusion flames between two opposing gaseous streams and for this simulation we selected 100 grid points. In the following figures of this section, the profiles of temperature and some important species (methane and oxygen) are plotted in the mixture fraction space for the cases of 100x100, 300x300 cells in OpenFOAM and for the case of 100 grid points in CHEM1D.

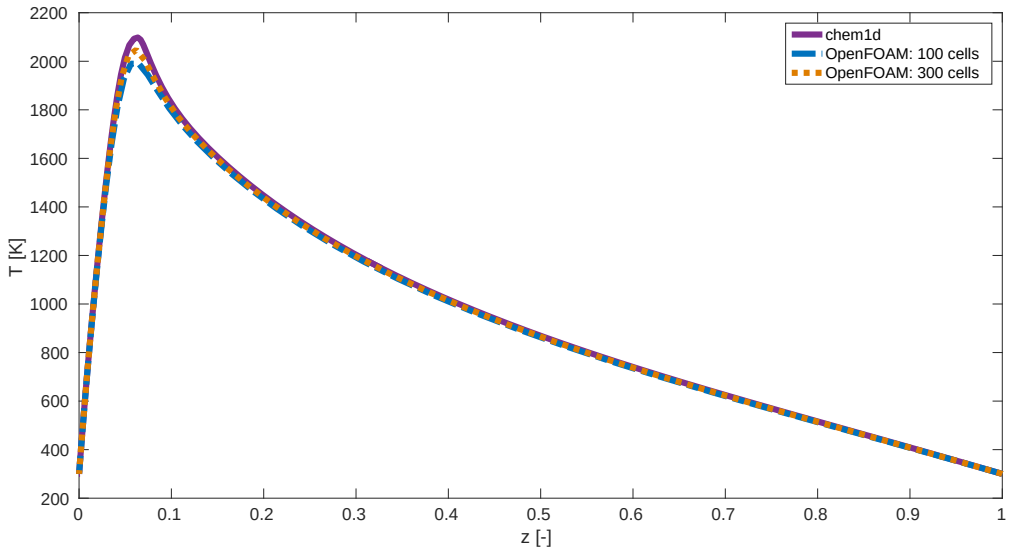

Figure 4.1: Temperature profile as a function of Mixture Fraction in CHEM1D and OpenFOAM

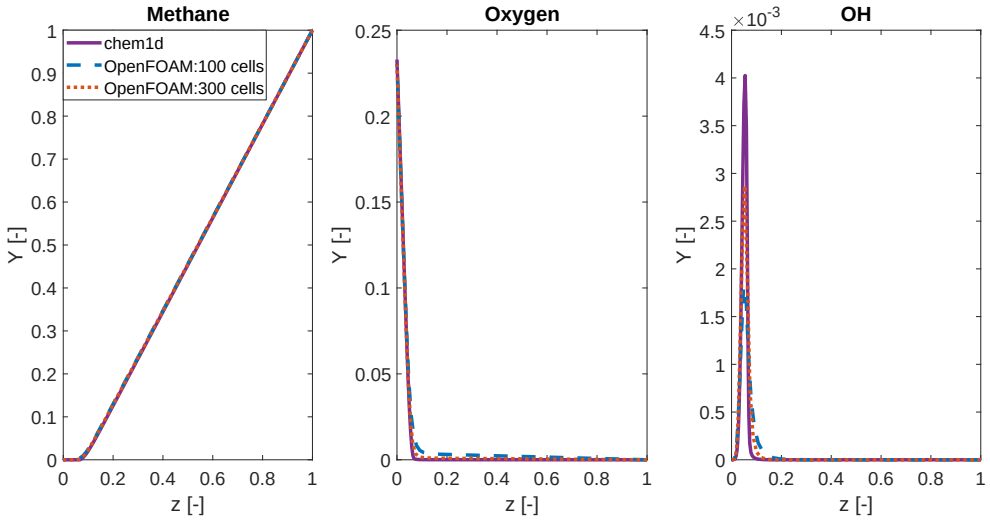

Figure 4.2: Methane, Oxygen and hydroxyl-OH mass fraction profiles in CHEM1D and OpenFOAM

The Figure 4.1 shows the temperature profile as a function of mixture fraction and it is evident that CHEM1D predicts a higher peak. However, OpenFOAM in both cases predicts the trend of temperature quite well and also the position of the reaction zone which is approximately at $z_{stoic} = 0.054$. In Figure 4.2, the evolution of methane, oxygen and hydroxyl-OH mass fraction profiles are shown for the three cases. The solutions for the methane and oxygen converge and there is no deviation for any of the cases. For the minor species hydroxyl-OH, the trend of the profile and the location of the peak are predicted well for all the cases and only the magnitude of the peak presents some under-prediction in OpenFOAM, since refinement of the mesh is needed close to the stoichiometric conditions. Overall, we can conclude that the solver le1reactingFoam and the set-up of the case in OpenFoam predicts the important variables accurately compared to those of the CHEM1D calculation assuring us that the model is reliable enough to continue with the calculations. Of course, it is clear that the finer mesh urges towards a solution closer to the CHEM1D's one, but in our case the more coarse mesh (100x100 cells) is preferred for the following calculations since it compensates in terms of computational time.

4.3. Gaseous Flamelets

In this section, the results regarding the gaseous flamelets are presented. As it is shown in table 3.6, four different cases are considered here for four different strain rates (55/s, 300/s, 500/s, 800/s) applied on the oxidizer side of the configuration. The boundary conditions are shown in the table 3.3 and the solver to be used is the le1reactingFoam.

The first Figure 4.3 includes the results regarding the temperature for the four gaseous flamelets, plotted in the physical space (along the x-axis). It is distinct for the lowest strain rate (55/s) that the region around the peak of the temperature or else the reaction zone is located closer to the oxidizer side (right side). For higher strain rates though, there is a shift of the reaction zone towards the stagnation plane with a simultaneous drop of the maximum of the temperature curve. This can be explained because the flames, closely to that region, are strained meaning that they present increased local velocity gradients due to the higher

imposed strain rates at the boundary conditions. This consequence leads to reduced residence time for the reactants in the reaction zone resulting in weaker and slower reactions. This remark can also be seen in the Figure 4.5 where the axial velocity for the four cases is plotted along the x-axis of the cartesian system. We can see there that starting from the position -0.02m the axial velocity decreases linearly till it reaches the stagnation plane (+0m) from where the slope of the velocity curve changes creating the source for the strain of the flame. This phenomenon is more apparent for the higher strain rate cases.

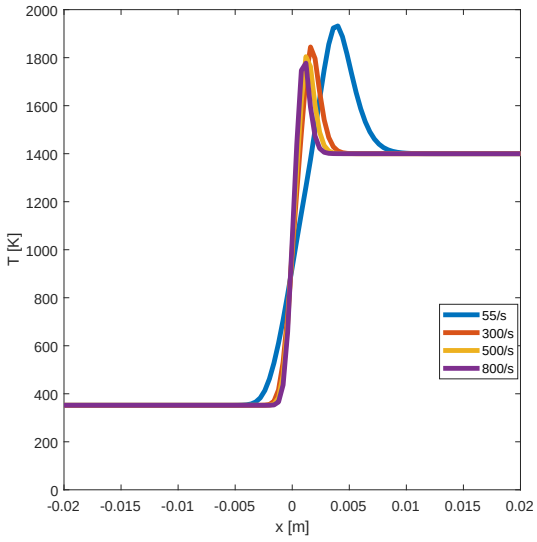

Figure 4.3: Temperature profile for varying strain rates in the physical space

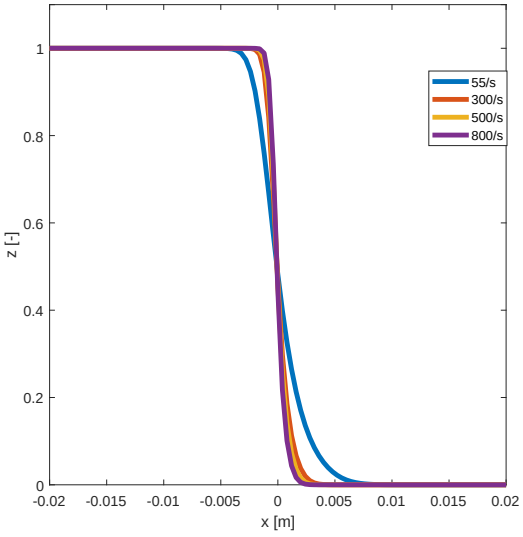

Figure 4.4: Evolution of mixture fraction in physical space for different strain rates

An interesting remark can be derived by looking at the Figure 4.6 where the axial velocity is plotted against the mixture fraction. We can notice there two jumps of the velocity at the positions z=0 (oxidizer side) and z=1 (fuel side), while the velocity is almost zero in between. The reason for this peculiar behavior is that for all the cases, the mixture fraction evolves in the physical space only around the stagnation plane, from -0.004m (z=1) to +0.006m (z=0), as it is shown in Figure 4.4. This region is the thin layer in which the two opposing streams mix and the flows are almost stagnant. The profile of mixture fraction in Figure 4.4 is monotonically decreasing and gives a measure of the local presence of fuel (z=0 means no presence of fuel and z=1 means all the fuel entered the domain is present).

The stagnation point can be seen more clearly in the 2D illustration, Figure 4.7, of the simulation using Paraview, the visualization tool of OpenFOAM. At the figure on the right side, +0.02m, we have the oxidizer stream (hot coflow products) inlet and on the left side, -0.02m, the inlet of the fuel stream (ethanol gas). The green arrows mark the trajectories that the fluid particles follow (streamlines). This snapshot refers to the case for strain rate equal to 55/s at a moment where the steady state solution is obtained. This strain rate is applied on the oxidizer side and applying the Bernoulli principle as explained in the previous chapter we find the respective strain rate for the fuel side and is used as a velocity boundary condition. We can see that the fluid streams in the middle of the domain are inert and the fluid particles that come from neighbouring regions accelerate around the stagnation point. In the background of the scheme the temperature evolution in the domain is shown. From this representation it

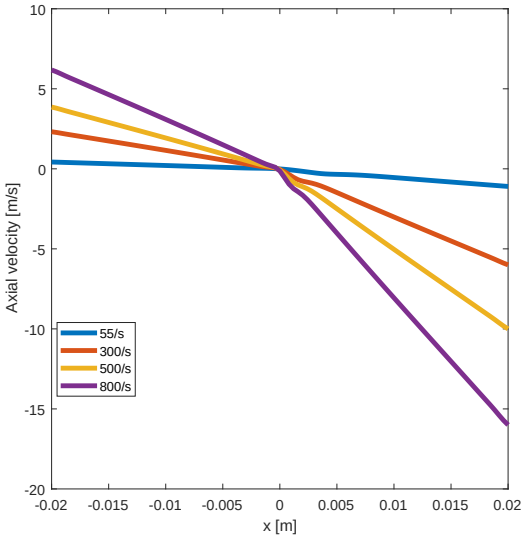

Figure 4.5: Axial velocity for varying strain rates in the physical space

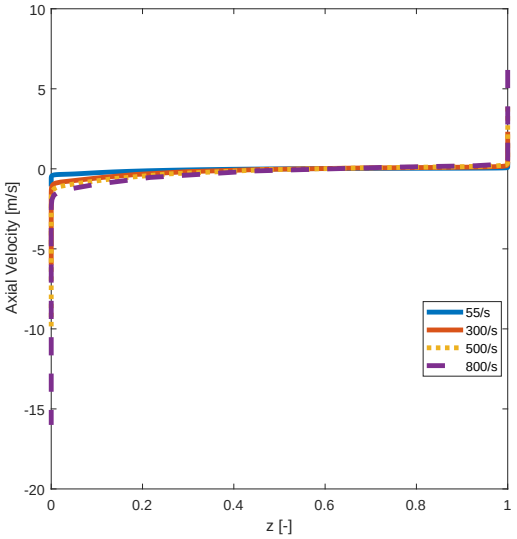

Figure 4.6: Axial velocity for varying strain rates in the mixture fraction space

is clear that the temperature (the same holds for the species mass fractions, not shown here) is uniform along the y-axis and no gradients are seen. This uniformity allows us to sample the data at the horizontal center-line of the domain and this is the approach we followed to transport the data from the 2D to 1D physical space. Thus, the x-axis along which all the interested variables are plotted in the following figures refers to such a center-line of a 2D configuration.

In Figure 4.8 the four gaseous flamelets are presented separately. The trends for the temperature and some important species are shown in the mixture fraction space reflecting the influences of the increasing strain rate from case to case. As already discussed, the temperature tends to present a lower peak as the strain rate increases. In addition, the mass fraction profiles indicate that the ethanol and the oxygen start diffusing in the domain far from each other (very rich conditions on fuel side and very lean in the oxidizer side) and only when they reach a favorable mixing, reaction takes place [14]. The favorable mixing relaxes under stoichiometric proportions. Ideally, for a single chemistry step between ethanol and oxygen, the stoichiometric conditions demand:

$$C_2H_5OH + 3O_2 \rightarrow 2CO_2 + 3H_2O \tag{4.1}$$

and the stoichiometric ratio for this case is found by:

$$s = \frac{v'_O W_O}{v'_F W_F} = \frac{3kmol * 2 * 16kg/kmol}{1kmol * 46kg/kmol} = 2.087 \tag{4.2}$$

then the stoichiometric conditions in the mixture fraction space can be located at the position [14]:

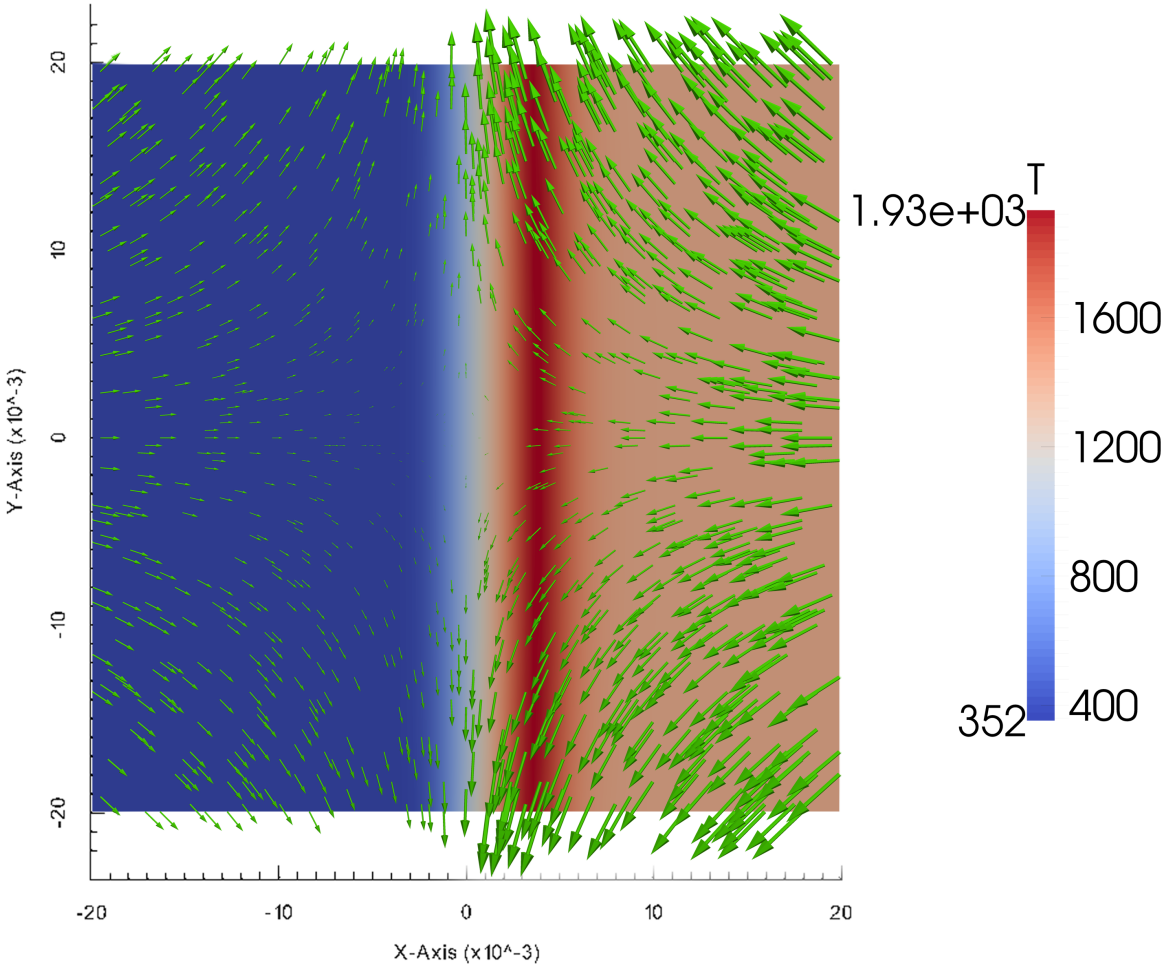

Figure 4.7: 2D illustration of the counterflow configuration showing the temperature and the velocity vectors in Paraview for a=55/s

$$z_{st} = \frac{1}{1+\Phi} = \frac{1}{1+\frac{sY_F^0}{Y_O^0}} = \frac{1}{1+\frac{2.087*1}{0.1}} = 0.0457 \tag{4.3}$$

where Φ is the equivalence ratio, $Y_F^0 = 1$ is the mass fraction of the fuel on the fuel side and $Y_O^0 = 0.1$ is the mass fraction of the oxygen on the oxidizer side. The stoichiometric mixture fraction ($z_{st} = 0.0457$) can be seen as the indicator for the position of the reaction zone and the location of the peak of the temperature profile. Indeed, as it can be seen from the plots of the Figure 4.8, this is approximately the case. However, this observation is not completely accurate for our current project since as we already described, the calculations are based on a multiple-step mechanism including intermediate species and reactions. Thus, ethanol is subjected to dissociation and cracking reactions and in reality not only ethanol but also secondary fuel by-products react finally with oxygen. Nevertheless, the idea of stoichiometric mixture fraction can always be applied to give us an approximate location of the reaction zone. An alternative marker of the reaction zone can be the formation of hydroxyl-OH, where its peak region is assumed to correspond to the flame front location [14]. As it is also reported by R. Gordon et al. [61] and L.Ma [2]. For these reasons the profile of OH is also plotted for

the four cases. We can conclude for those figures (4.8) that heat is diffused from the reaction zone to the fresh reactants and as soon as the activation energy demands for the reactions are fulfilled, auto-ignition occurs coinciding with the peak of OH formation.

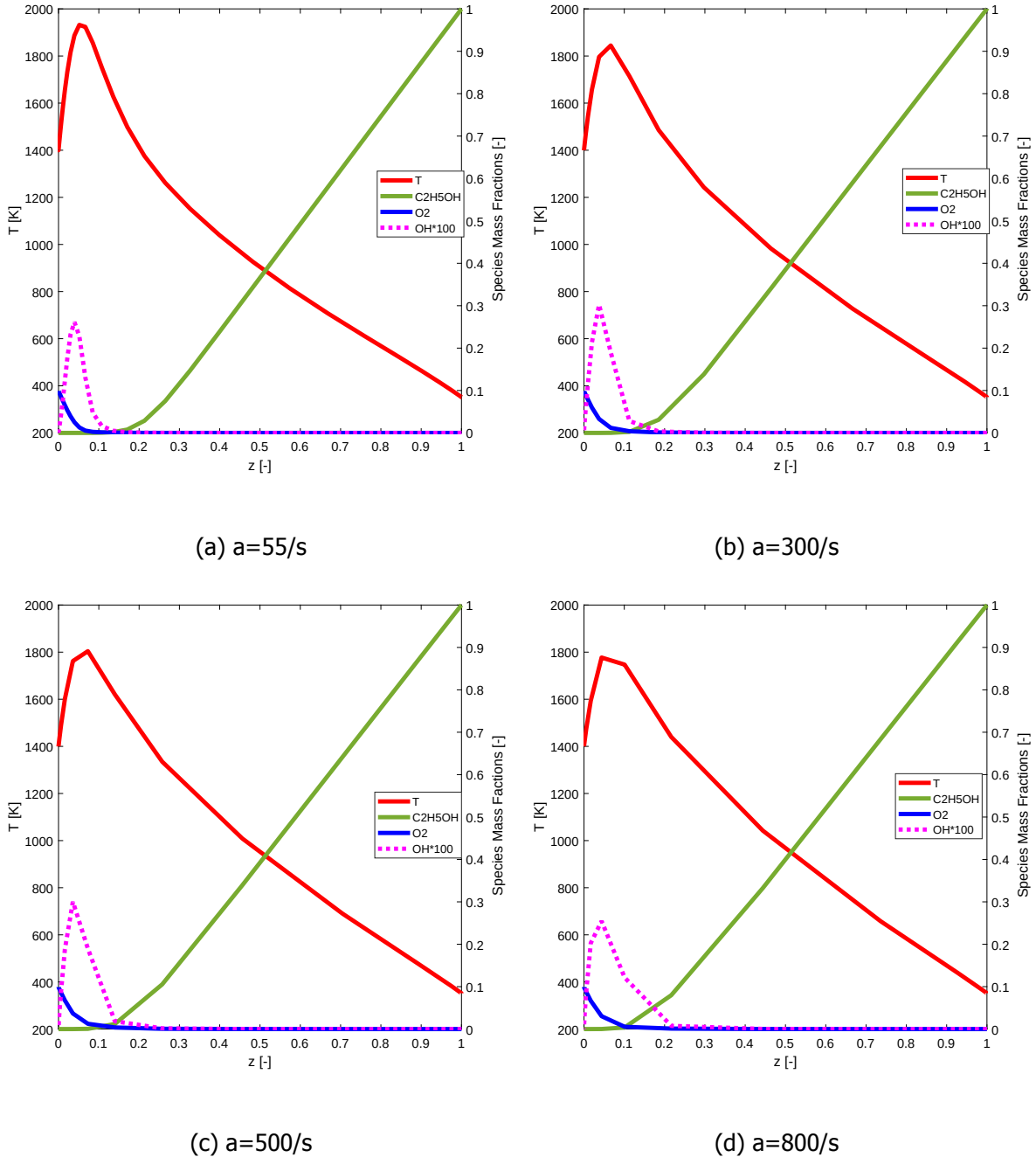

(a) a=55/s (b) a=300/s

(c) a=500/s (d) a=800/s

Figure 4.8: Temperature and Species Mass Fractions profiles for different strain rates in the mixture fraction space

In Figures 4.9 and 4.10, the chemical source terms (w_k) for the species of oxygen (w_{O2}) and ethanol (w_{eth}) are presented together with their respective mass fraction distributions. In these figures also the profiles of temperature (scaled down by a factor of 2000) and of heat release (or consumption), Qreact, due to reactions are shown. These curves are created in the physical space for the strain rates of 55/s and 800/s applied in the oxidizer side.

For the lower strain rate in Figure 4.9, the ethanol and oxygen mass fraction profiles (indicated in the figure by the dotted green line C2H5OH and the dotted blue line O2 respectively) start by keeping constantly their boundary conditions values until they reach the mixing layer where they experience a huge drop (region -0.004m to +0.006m) and these drops are accompanied by respective negative chemical source terms. The important remark here is that ethanol which is the main fuel source is subjected to dissociation and cracking reactions and breaks into secondary fuel products. These chemical mechanisms are endothermic and this is reflected to the energy chemical source term at the position +0.002m where an energy sink is observed. These fuel by-products diffuse and react instantly with the oxygen stream releasing heat and giving space for temperature rise. At position +0.0045m, combustion is intense leading to local maxima for the temperature, the heat release and the oxygen consumption. Also at that position no consumption of ethanol is observed, verifying that it is already decomposed into intermediate species. Then temperature (via heat transfer) diffuses away from the reaction zone towards the fuel and oxidizer streams.

On the other hand, for the significantly higher strain rate of 800/s in Figure 4.10, the higher initial momentum induced on both streams, decreases the residence time of ethanol in the route of approaching the stagnation level and as a result the processes of dissociation and cracking are weakened. Indeed, this remark is evident observing that the drop of ethanol's mass fraction profile starts at a later position than in the previous case and is followed by a steeper negative gradient in the reaction zone. The regions of ethanol and oxygen consumption rates partially coincide indicating that both cracking reactions and combustion of ethanol take place. The existence of cracking reactions is shown by a negative extreme for heat release at the position +0m. However, at the same position there is simultaneous generation of heat, meaning that the combustion has already taken place.

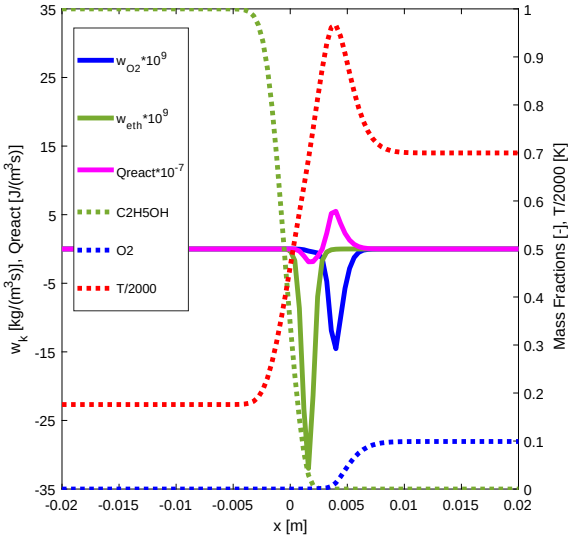

Figure 4.9: Profiles of chemical reaction sources for energy and species, a=55/s

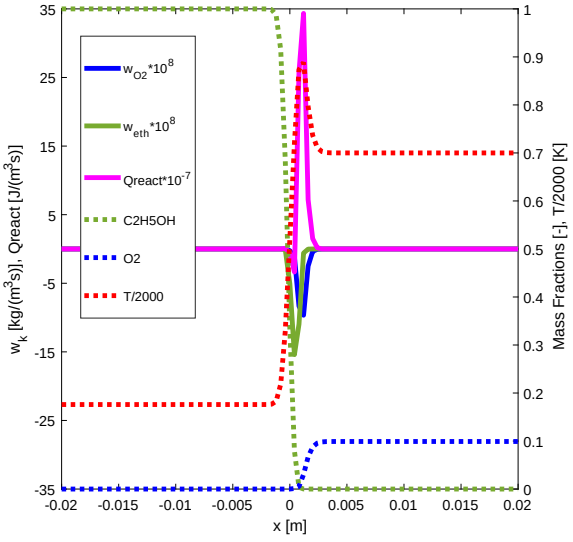

Figure 4.10: Profiles of chemical reaction sources for energy and species, a=800/s

Comparing the two graphs, we can conclude that for the higher strain rate, the reaction is weaker and limited to a narrower region, since the generated heat is convected at a high rate by the opposing streams. Also, the low strain rate case is dominated by cracking reactions and

no combustion of the main fuel is seen, whereas both reaction mechanisms for the main fuel take place in the higher strain rate case that are associated with steeper mass fraction profiles. At last, the order of magnitude of species consumption rate and heat release is larger for the higher strain rate case since the higher imposed boundary velocities lead to higher mass flow rates for both streams.

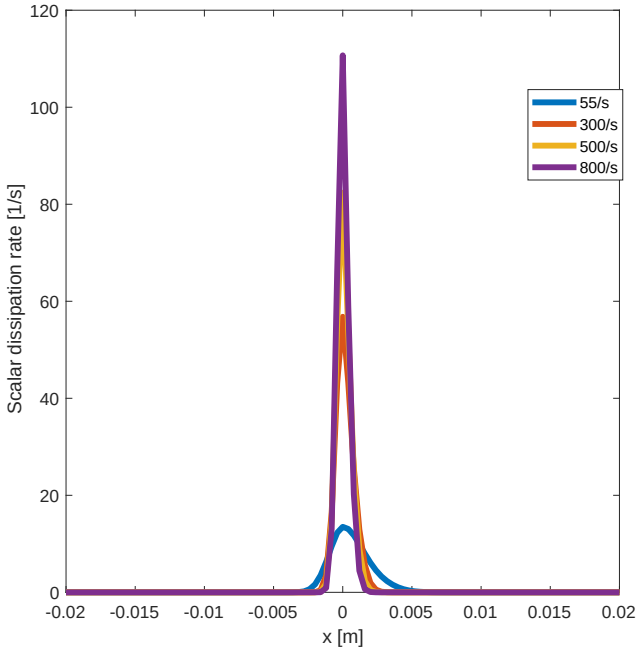

Figure 4.11: Evolution of scalar dissipation rate in physical space for different strain rates

In Figure 4.11 the scalar dissipation rate is plotted for different strain rates. As it was shown in equation (2.102), it depends strongly on the gradients of mixture fraction and in that sense χ controls the mixing [14], so as a result we can say that different evolutions of scalar dissipation rate promote different flame structures. It measures the molecular fluxes of species towards the flame and as χ approaches zero all molecular fluxes are negligible compared to the reaction rates, meaning that the reactants do not mix and as soon as they meet they react due to very short chemical time scales compared to the flow time scales. We also saw in the second chapter that high values of scalar dissipation rate can lead to extinction of the flame. In addition, since scalar dissipation rate has a proportional correlation (see equation 2.106) with strain rate, an increase of the one leads to a consecutive increase of the other. The mixing of the opposing streams occurs at the stagnation plane where the gradients of mixture fraction are steep and this is reflected to the χ profile in Figure 4.11.

4.4. Spray Flamelets

In this section the results regarding the simulations of the spray flamelets are displayed and discussed. These simulations refer to a set of varying parameters according to the table 3.6. More specifically, the influence in the flow characteristics and the flame structure of the spray flamelets will be identified for different values of the equivalence ratio defined on the fuel side, the strain rate defined on the oxidizer side and of different initial droplet sizes.

4.4.1. Temperature and droplets' diameter evolution in the physical space for Φ=1

Figures 4.12 and 4.13 show the evolution of temperature (continuous curves) and droplets' diameter (discrete points) along the center-line of the domain (Figure 4.7) in the physical space. The former one considers a stoichiometric equivalence ratio ($\Phi = 1$), while the latter a richer proportion between spray and oxidizer ($\Phi = 3$). The equivalence ratio is set on the fuel side, where ethanol spray is carried by hot coflow products of low oxygen level, whose composition is shown in table 3.1. Each equivalence ratio case takes also into account variations of the strain rate and initial droplets' diameters as well. Looking at the plots for the stoichiometric equivalence ratio (Figure 4.12), it becomes clear that the flame structure of the spray flamelets is not susceptible only to the changes of the strain rate, as it was shown for the gaseous flamelets in the previous section, but also to the size and the motion of the droplets. For the somewhat low strain rate, a=55/s (Figure 4.12a), we observe that the smallest initial droplets have the shortest lifetime and evaporate very fast already at the position -0.015m. As soon as the initial diameter increases the mass of each individual droplet increases and so does their initial momentum. Also, the amount of heat needed per droplet to evaporate increases. As a result, droplets of larger initial size manage to penetrate further in the domain and we see for example that droplets with Do=100μm reach the stagnation level (+0m).

The position at which the droplets relax and evaporate plays an important role for the outcome of the chemical reactions and the combustion. For example, the generation of fuel vapor by the initially smaller droplets (Do=40μm) occurs closely to the origin of the domain and diffuses in an area where low surrounding temperature conditions and weak reactions dominate. As a result, a wider reaction zone is promoted with a lower peak of temperature. This remark comes to an agreement with the fact that the evaporation process for those droplets takes place in a limited area and acts as an energy sink for the activation of the chemical reactions which are slowed down. On the other hand, initially larger droplets evaporate gradually in a more extensive area promoting narrower but of higher intensity reaction zones. A change in the droplet size affects not only the intensity of the reaction zone but also its location. Thus, for the droplets of Do=80μm and Do=100μm their respective reaction zones move towards the stagnation plane.

The remarkable aspect for those two cases is the creation of a double reaction zone and the existence of a local temperature minimum. This local minimum as it is also reported by Gutheil et al. [47] is provoked by intensified evaporation of the droplets. Indeed, for the droplets of Do=80μm and Do=100μm it seems that their local temperature minimum coincides with the location of their last seen droplets at the position -0.005m and +0m respectively. Approaching the stagnation plane the momentum of both the gaseous and the spray streams is decreased and as a result the residence time of the droplets in that region is increased leading to enhanced evaporation. However, since the surrounding temperature at this region is already high, the reaction rates, according to the Arrhenius law (equation (2.55)) are sensitive to the temperature drop caused by the evaporation and as a result the reactions are slowed down. Greenberg et al. [62] characterize the first seen flame front in which the fresh generated ethanol vapor mixes and reacts with the surrounding oxidizer as a partially premixed flame, and the second one where the rest of the ethanol vapor opposes against the oxidizer stream from the right side of the configuration as a typical diffusion flame. According to T.H.Lin et al. [63], a partially premixed flame is defined as a flame which receives fuel or oxidizer or both from both sides of its reaction zone. This dependency between the droplets' sizes and the temperature may lead to hotter flames compared to the gas diffusion flames that were shown

in the previous section as it is also reported in [64]. The reason for this concept is that if we isolate the diffusion second reaction zone, we see that the boundary temperature condition for the ethanol gas is approximately 1900K which is significantly higher than the one of the gaseous flamelets (352K).

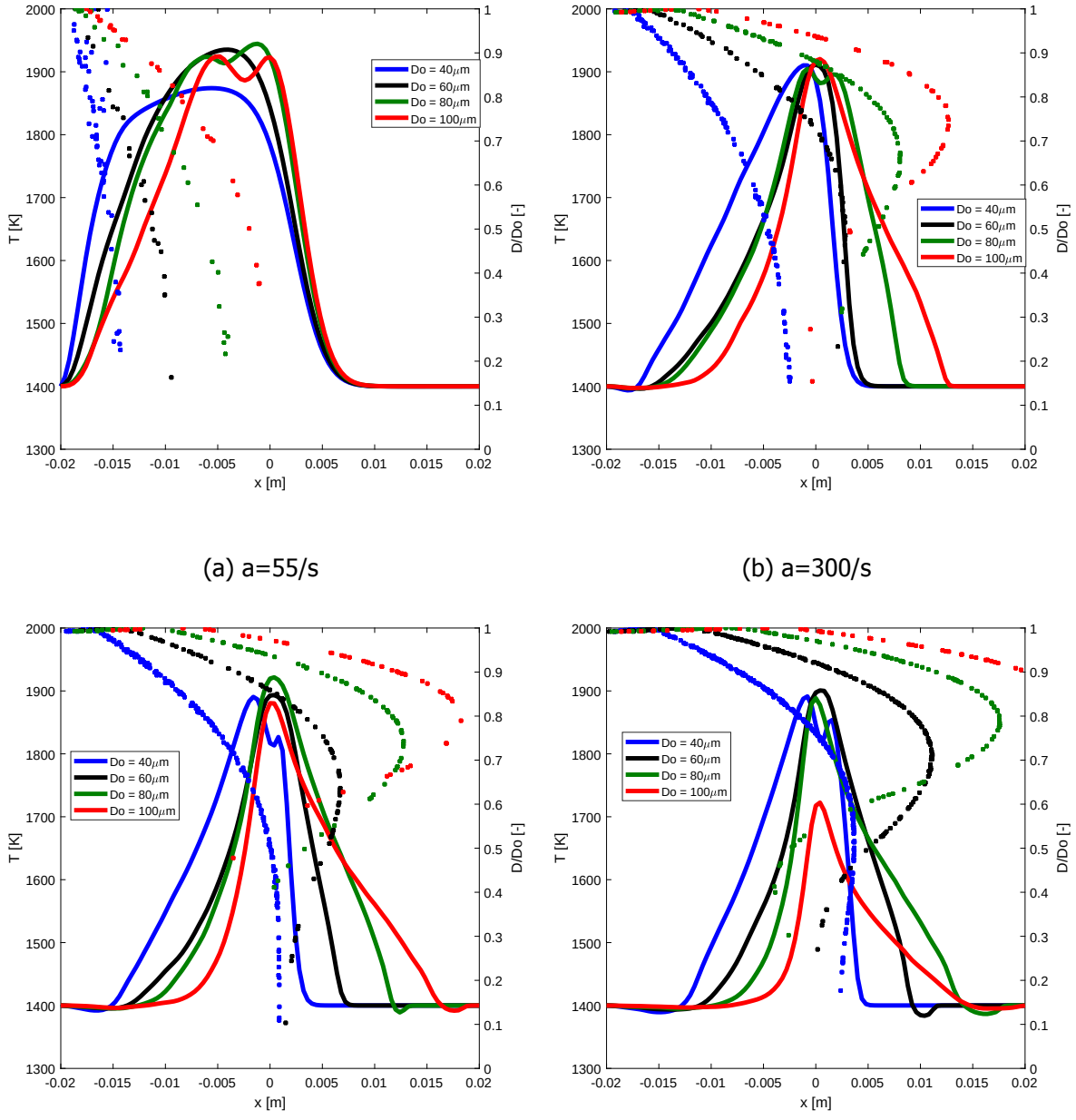

(a) a=55/s (b) a=300/s

(c) a=500/s (d) a=800/s

Figure 4.12: Temperature and Droplets' diameter evolution in the physical space for $\Phi = 1$ on the fuel side, for four different strain rates and four different initial droplets' diameters

Increasing gradually the imposed strain rate, the initial momentum of the droplets is increased and the droplets penetrate further to the right side of the configuration. When this increase of the strain rate is combined with a simultaneous increase of the initial droplets' diameter

then a reversal of the droplets is possible, due to momentum exchange between the droplets and the opposing hot gaseous coflow stream coming from the right side. If the momentum content of the droplets is such that they can cross the stagnation plane twice, then a second reversal occurs and the droplets oscillate around the stagnation plane as it shown for the case of a=800/s, Do=80μm in Figure 4.12d). The possibility for droplets' reversal or oscillation has also been reported by Gutheil et al. [64]. In the same figure and for the case of initial diameter Do=100μm, we see that the momentum of those droplets is so large that they overcome the opposing stream and exit the computational domain at the right hand side leading to an incomplete combustion. As it is already discussed, accumulation of evaporating droplets at a certain location might lead to local drop of temperature and the formation of a double reaction zone. This is also seen for the cases a=300/s-Do=80μm, a=500/s-Do=40μm and a=800/s-Do=40μm.

Overall, we can say that by either increasing the initial droplets' diameter or the imposed strain rate (or both) the initial momentum of droplets increases making them convey further into the computational domain. The longer penetration of droplets of larger initial diameter is also explained by the fact that a larger amount of evaporation heat is needed per droplet. This results in the prolongation of the evaporation process creating locally different fuel vapor states affecting so the reaction zone. On the other hand, lower initial droplets' momentum leads to wider reaction zones of lower peak temperatures. In turn, rising the initial momentum, the reaction zone becomes narrower and if the droplets reach the stagnation plane, enhanced evaporation rate favors the creation of a double flame. Further increase of the initial droplets' momentum leads the droplets into the opposing gaseous stream and one or more droplets' reversal are observed. This increase of the momentum has also the two flames coming closer and even merging at a certain point (see the evolution of temperature profile of Do=80μm for the different strain rates as an example). From these observations we can declare that a converging trajectory of droplets to the stagnation plane without large oscillations around it is a condition for the formation of two reaction zones (see as an example the evolution of temperature profile of Do=40μm for the different strain rates and the evolution of temperature profile of a=55μm for the different initial droplets' diameter). Finally, if the combination of bigger droplets' sizes and higher strain rates leads the evaporation process to regions where combustion is not strong enough, then local flame extinction might happen [47]. In that sense, we realize that apart from the strain rate, also the initial diameter can be a limiting parameter for flame extinction. According to this remark in that case, the flame extinction does not occur due to a lesser residence time of the reactants in the reaction zone as in the case of the gaseous flamelets for increased strain rates, but to the intense evaporation that behaves as an energy sink weakening the reactions.

4.4.2. Temperature and Droplets' diameter evolution in the physical space for Φ=3

Proceeding with the Figure 4.13 the influence of an increased equivalence ratio in the flame structure in considered. For the gaseous flamelets the equivalence ratio does not consist an independent variable since the mass flow rates of the incoming streams are settled by the applied strain rates. However, for the spray flamelets it can be set independently. Hence, by imposing a rich spray to oxygen ratio (Φ=3) on the fuel side, we notice the formation of two reaction zones for all the cases irrespectively of the initial strain rate or droplets' diameter, due to varying availability of oxygen. For lower strain rates and initial droplets' sizes (e.g. Φ=3-a=55/s-Do=40μm, Figure 4.13a), the early evaporation initiates the first reaction zone

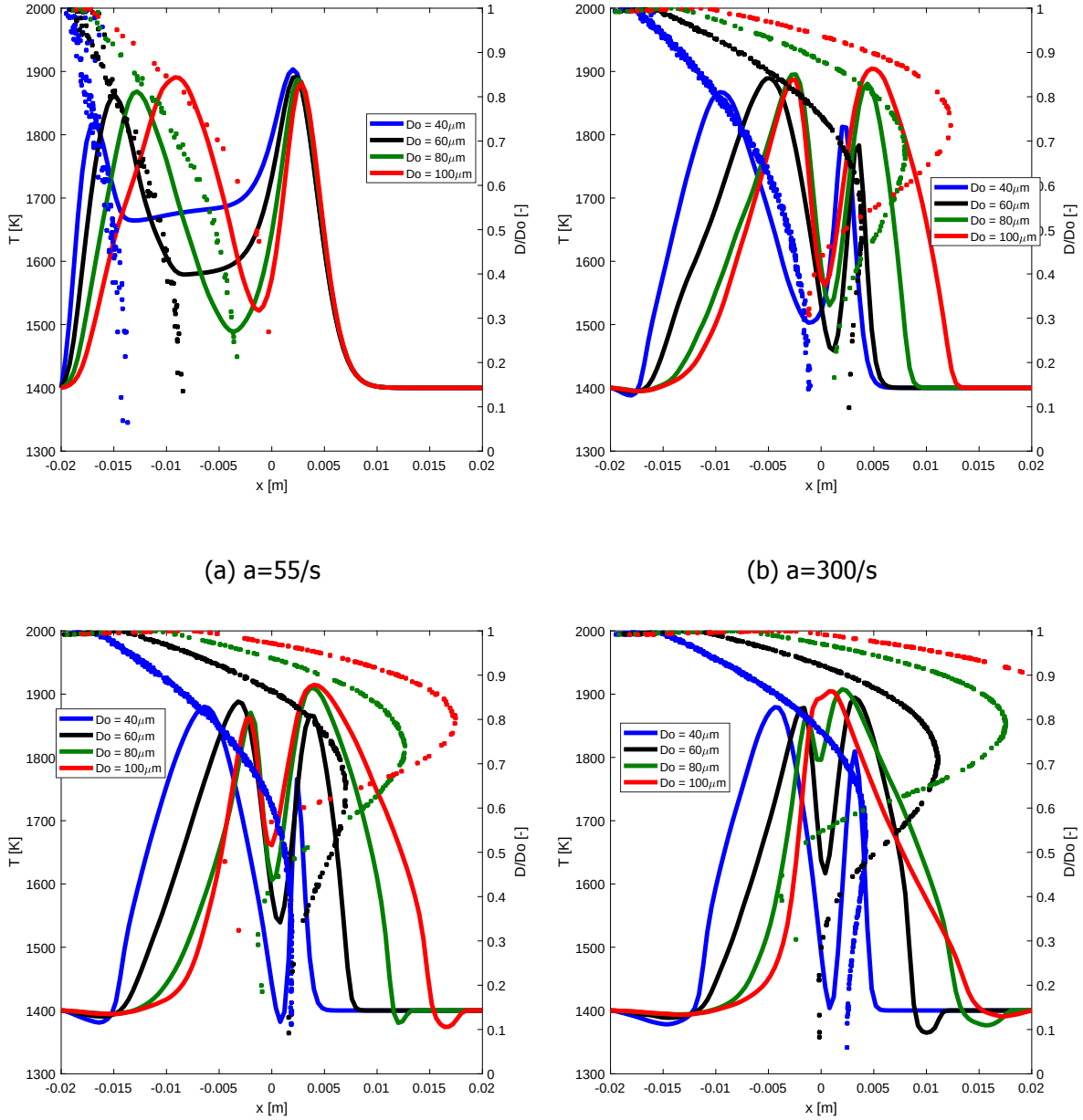

(a) a=55/s

(b) a=300/s

(c) a=500/s

(d) a=800/s

Figure 4.13: Temperature and Droplets' diameter evolution in the physical space for $\Phi = 3$ on the fuel side, for four different strain rates and four different initial droplets' diameters

and the surplus of ethanol vapor that is not consumed in the reactions is diffusing towards the stagnation point where it instantly mixes with the opposing oxidizer stream driving the second reaction zone.

For a=55/s, Figure 4.13a, comparing the two temperature peaks for each profile we can observe that the left peak is lower than the right one for the cases Do=40μm, Do=60μm and Do=80μm due to the excessive evaporation that takes place in the left reaction zone. Nevertheless, a gradual increase of the initial diameter moves the droplets and the evaporation

process further in the domain resulting in a simultaneous increase of the left and decrease of the right temperature peak. For a=55/s, we also see that the location of the diffusion flame (right reaction zone) remains constant and close to the stagnation plane, while the partially premixed flame (the left one) moves together with the droplets and comes closer to the stagnation plane as the initial droplets' size increases due to the dependency of the reaction zone on the generation of fresh fuel vapor. For higher strain rates the two reaction zones come even closer and reversal of the droplets is noticed. Oscillation of droplets around a reaction zone generates fresh fuel vapor and thus enhances the reaction rate locally despite the energy consumption for the evaporation. A characteristic example of this remark is the case Φ=3-a=500/s-Do=100μm (Figure 4.13c) for which the right flame front present a higher temperature rise compared to its left one. Furthermore, a temperature drop below 1400K (temperature boundary condition) can occur due to the evaporation in regions far from the reaction zones as it can be seen from the cases a=800/s-Do=60μm at +0.01m and a=800/s-Do=80μm at +0.015m.

4.4.3. Evolution of mixture fraction and important species mass fractions profiles in the physical space

The evolution of some important species mass fractions are shown in Figure 4.14 for different values of the equivalence ratio, the strain rate and the initial droplets' size. The represented species are C_2H_5OH and O_2 which are the reactants of the main reaction 4.1, the species of H_2O and CO_2 that make up the products of the reaction and define the outer flame structure [65] and finally CO that is formed prior to CO_2 and OH which is a radical that is formed during combustion. In addition, the profile of mixture fraction (z) is plotted. Mixture fraction is the indicator of the local presence of fuel vapor that originally comes from the fuel side of the configuration and for the gaseous flamelets is associated with monotonicity as it was shown in the previous section in Figure 4.4. However, in a spray flame there is no presence of fuel vapor initially and the evaporation creates different mixture fraction states from point to point and as a result this monotonicity is broken.

For the case of the lowest initial droplets' momentum (a=55/s, Do=40μm, Figure 4.14a), the evaporation starts early and the trajectory of the droplets in the domain is short. This instant generation of fuel vapor results in a steep positive gradient for the curve of mixture fraction. At the point of completion of evaporation (-0.015m) where the last droplet is seen, a maximum value of z is recorded which is approximately retained till the point +0.005m where a drop for z starts due to diffusion and mixing with the opposing hot coflow stream coming from the right side of the configuration. At the location of the creation of the mixture fraction's extreme we can make a distinction about the characteristics of the flame. Thus, in the region from -0.02m to -0.015m the flame strongly depends on the evaporation of the droplets and so resembles a partially premixed flame, while right after no droplets are found and the gaseous streams from both sides diffuse, mix and react and so we may attribute this part of the reaction zone as a pure gas diffusion flame. This becomes more clear seeing in Figure 4.14a that the z profile in the region -0.015m to +0.02m is very similar with the one obtained in Figure 4.4 for the gaseous flamelet of a=55/s. As it is expected, in the spray side of the configuration of Figure 4.14a the generated ethanol vapor leads to local increase of the respective mass fraction profile at -0.017m and the same time reactions take place with a simultaneous consumption of O_2. An important remark here is that in the biggest part of the consumption area of O_2 (-0.013m to +0.003m) there is no presence of C_2H_5OH. This means that due to the hot surrounding environment C_2H_5OH is already broken into intermediate

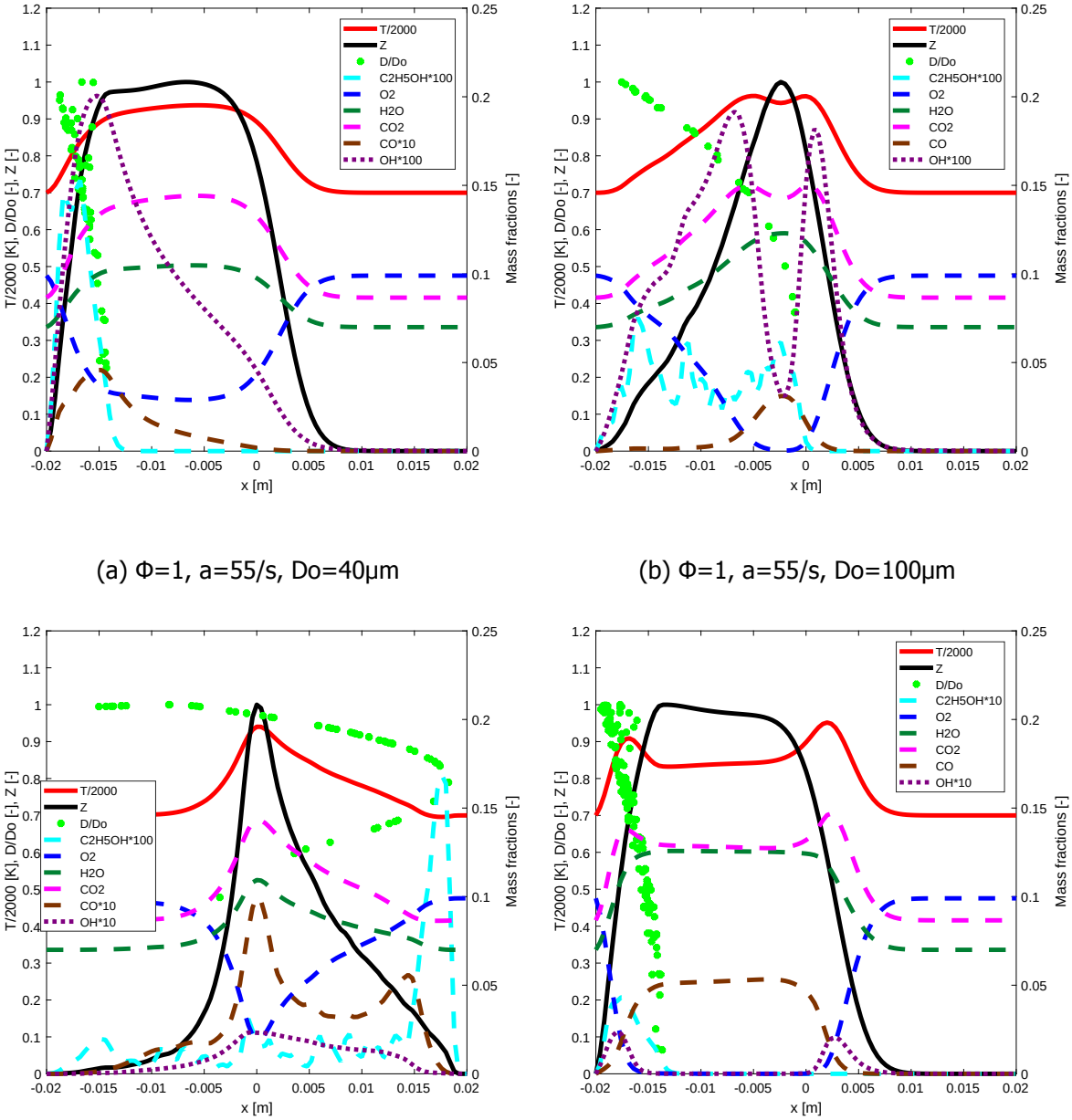

(a) Φ=1, a=55/s, Do=40μm

(b) Φ=1, a=55/s, Do=100μm

(c) Φ=1, a=500/s, Do=100μm

(d) Φ=3, a=55/s, Do=40μm

Figure 4.14: Evolution of mixture fraction (z) and important species in the physical space for various Φ, a and Do

species, which in turn feed the combustion. The begin of the reactions on the left side is marked with creation of a maximum of CO at -0.015m, a species that is formed prior to CO_2. The initiation of the reactions at this point is also verified by a maximum of OH witnessing that ignition has already taken place. In turn, H_2O and CO_2 are the main combustion products and their distributions follow the temperature profile.

By increasing the initial droplets' diameter to Do=100μm (Figure 4.14b) two reaction zones are formed as it is shown by both the profiles of temperature and OH. The droplets due to higher initial momentum manage to reach the stagnation point where the evaporation ends

forming a peak in the z profile. The intense evaporation at -0.002m and the simultaneous local extinction of O_2 leads to the local minimum of temperature and the distinction of two reaction zones and this is also reported in [66] and [47]. The same time, this drop of temperature and the weakening of the reactions gives space for CO formation. Analogous flame structures having air as oxidizer stream at atmospheric conditions have been also reported by [66] and [47].

A following increase in the strain rate to a=500/s (Figure 4.14c) decreases the residence time of the reactants in the reaction zone and the temperature profile experiences lower values at the stagnation point. This slowing of the reaction rates at this region is reflected to the CO curve where a first local maximum is created. This case is characterized by droplets' reversal at +0.018m and their relaxation at this point gives rise to evaporation and a maximum of C_2H_5OH mass fraction profile. This instantaneous formation of ethanol vapor initiates reactions which however due to the low surrounding temperature are weak resulting to the second maximum of CO. In the stagnation point the maximum of z is formed which is not retained since evaporation is on progress and fresh ethanol vapor forwards new mixture fraction states. Finally, the gradient of z in the region -0.02m to -0.008m is very small indicating that no significant evaporation happens there and as a result the reactions are very slow since the temperature and the indicative species H_2O, CO_2 and OH barely increase.

Moving to the case that the equivalence ratio is increased to three (Figure 4.14d) local deficiency of O_2 leads to the existence of two reaction zones, a first partially premixed flame that is fed with fuel vapor and oxygen from the left side of the configuration and a second diffusion flame in which intermediate fuel products after the decomposition of ethanol gas, diffuse and react with oxygen in a counterflow pattern. The strain rate and the initial droplets' size is low and so the evaporation process is not extensive at the end of which a maximum for z is attained at -0.014m. In the region -0.014m to -0.005m the mixture fraction is kept at a high level meaning that the fuel radicals diffuse without mixing with the opposing stream till the second reaction zone takes place. The two reaction zones are also marked by consequent maxima of OH and H_2O profiles. The ethanol profile shows that cracking mechanisms occur after the first reaction zone and as a result intermediate species drive the second flame. The second flame resembles very much the flame of the gaseous flamelet for a=55/s (Figures 4.3 and 4.4) not only in terms of temperature but also in terms of the mixture fraction evolution. Last but not least, it is noticeable that an increase in the equivalence ratio alone does not affect neither the trajectory of the droplets nor the location of the fuel vapor generation. This is justified by a straight comparison between Figures 4.14a and 4.14d, since the two case possess identical a, Do conditions and differ only on Φ. Overall, we can see that the evaporation process plays a crucial role in the distribution of the mass fractions of some important species and so does for the mixture fraction.

4.4.4. Profiles of evaporation and chemical reaction rates

The next set of plots in Figure 4.15 includes for the same conditions of Φ, a and Do with the Figure 4.14 the profiles of the evaporation source term, S_ρ^v of the continuity equation (2.63) and the chemical reaction rates of C_2H_5OH and O_2 appearing as chemical source terms in the species mass fraction transport equation (2.66).
Starting with the lowest examined strain rate, a=55/s, and initial droplets' diameter, Do=40μm, for the stoichiometric equivalence ratio (Figure 4.15a), we see that the early evaporation of the droplets is predicted by the S_ρ^v evaporation source term which becomes zero at the position

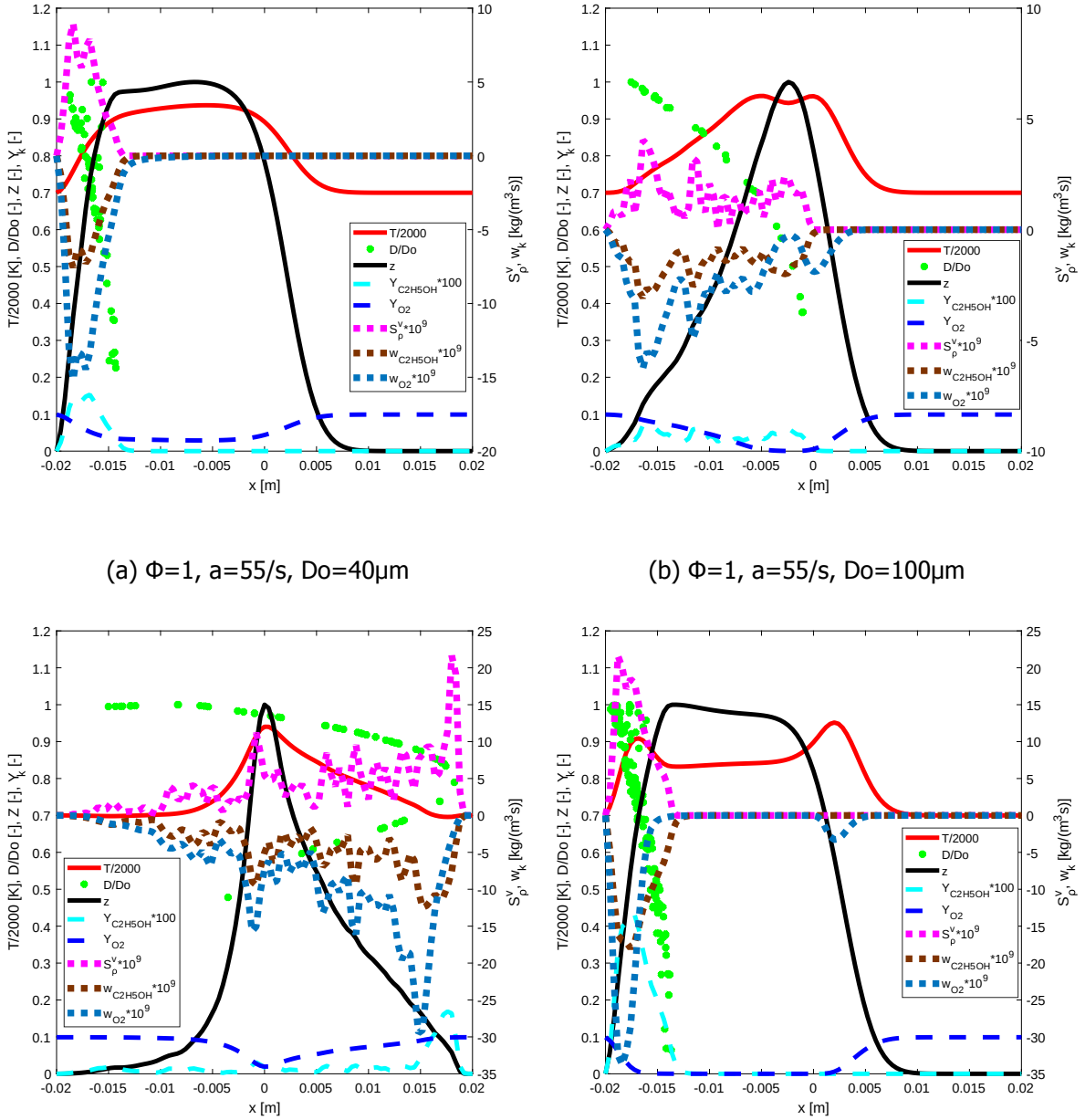

(a) Φ=1, a=55/s, Do=40μm

(b) Φ=1, a=55/s, Do=100μm

(c) Φ=1, a=500/s, Do=100μm

(d) Φ=3, a=55/s, Do=40μm

Figure 4.15: Profiles of evaporation and chemical reaction rates for various Φ, a and Do

of the last seen droplet. As it was discussed previously, the fresh generated fuel vapor at this region initiates the reaction which also in this case is reflected in the negative production rates of C_2H_5OH (w_{C2H5OH}) and O_2 (w_{O2}). The peaks of the three source terms coincide in the same location and more interestingly the peak of oxygen consumption is twice as the one of the ethanol vapor consumption fulfilling the stoichiometric conditions (see equations (4.1) and (4.2)) of the main reaction. Remarkable is also the fact that the evaporation source curve is approximately equal and opposite to the chemical source term of ethanol, showing that as soon as fuel vapor is generated it is also burnt at the same position instantaneously without letting the ethanol vapor to diffuse.

This relation between the three source terms is observed also in the rest of the figures, meaning that wherever a peak of S_ρ^v is formed, respective peaks of the ethanol and oxygen consumption follow at stoichiometric proportions. Exceptions are the regions where there is oxygen deficit as shown in Figure 4.15b at the position -0.003m and the regions where ethanol vapor is already decomposed into intermediate species as for example in Figure 4.15b at the position +0m and in Figure 4.15d at the position +0.002m. In the first place, having no O_2 presence, the ethanol vapor breaks into intermediate species and this is shown by a non-zero value of ethanol consumption while the respective source for oxygen is zero. On the other hand, for the second case, ethanol is already decomposed into radicals, which react in turn with oxygen. We mention here that the local fluctuations on the profiles occur due to non-uniform distribution of the droplets, since the injector releases droplets at random positions in the inlet plane every time step. Finally, local extrema are seen for S_ρ^v and w_{C2H5OH} at the stagnation planes and the reversal positions where the residence time is increased (see Figures 4.15b and 4.15c).

4.4.5. Profiles of scalar dissipation rate and axial Lagrangian and Eulerian velocities

In the following Figure 4.16, for the same variations of Φ, a and Do with the previous Figures 4.14 and 4.15, profiles for the gaseous and droplets' velocities and for the scalar dissipation rate are displayed. We should mention that the velocity profiles shown here refer to the axial velocity components and are normalized by the axial velocity of the main gaseous stream on the fuel (left) side of the configuration. Moreover, a non-slip condition is kept for all the cases in the fuel side of the configuration, meaning that the velocities of both the gaseous stream and the discrete phase match once entering the computational domain. A slip boundary velocity condition is among the five variables that may affect the spray flamelet's flame structure as it has already been discussed, but its influences are not investigated in this report and it is let to be studied in a future project.

Comparing the velocity profiles for the four different cases we see that as soon as the strain rate and the initial droplets' diameter is low, Figure 4.16a, the droplets remain almost attached to the streamlines of the gaseous flow and no substantial slip effects are shown. Similar droplets' behavior is observed also for fuel rich conditions in Figure 4.16d and it can be concluded that an increase in the equivalence ratio does not affect the relative motion between gas and droplets flows. However, an increase in the initial droplets' momentum by an increase of their initial diameter (Figure 4.16b) creates a mismatch for the velocities of the two flows (also reported by Continillo et al. [66]) which becomes more significant for a following increase of the strain rate as shown in Figure 4.16c where the droplets interact with the opposing stream reversing their motion. The higher this mismatch (slip velocity) it is, the higher the drag force acting on the droplets will be, leading to a deceleration of the droplets. We can observe this kind of behavior, which is also reported by Chen et al. [67], at the position -0.007m of Figure 4.16b where a maximum slip velocity occurs, followed by a steep drop of the axial velocity of the droplets towards the stagnation plane. When the droplets cross the stagnation plane and interact with the opposing gaseous stream (Figure 4.16c), the drag force is even larger having the droplets decelerate till they become stagnant (at +0.018m) and eventually reverse their flow. This zero droplets' velocity obtained at the reversal point explains also the increased residence time and the locally enhanced evaporation rate as it was shown in Figure 4.15c previously. Last but not least, an acceleration of the flow is also noticed in Figures 4.16a and 4.16d due to local intense reactions and the thermal expansion of the flow.

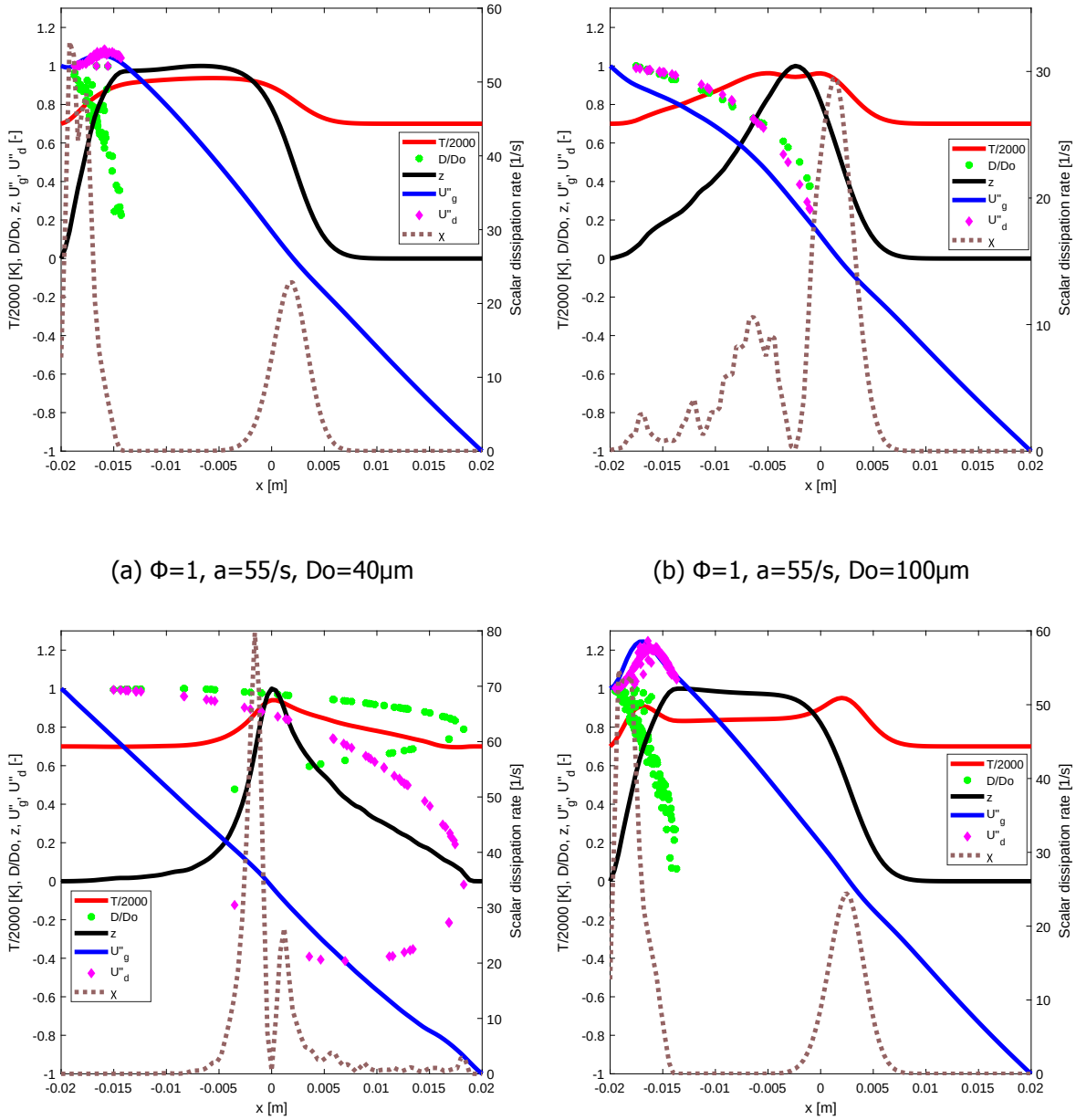

(a) Φ=1, a=55/s, Do=40μm

(b) Φ=1, a=55/s, Do=100μm

(c) Φ=1, a=500/s, Do=100μm

(d) Φ=3, a=55/s, Do=40μm

Figure 4.16: Profiles of normalized axial gaseous (U''_g) and droplets (U''_d) velocity and scalar dissipation rate (χ) for various Φ, a and Do

The significant larger slip velocity for the case Φ=1-a=500/s-Do=100μm (Figure 4.16c) compared to the case Φ=1-a=55/s-Do=100μm (Figure 4.16b) leads to another important remark which regards the evaporation process. This remark is based on the fact that a larger slip velocity makes a single droplet cross multiple fluid elements attached on different streamlines and thus increase the heat exchange between the two phases. If no or low slip velocity exists then a single droplet is attached to a unique (or crosses a lesser number of fluid elements) fluid element resulting in a falling temperature difference between the two phases and the slow down of the heat exchange. Now going back to Figure 4.15c (case Φ=1-a=500/s-Do=100μm),

which is linked to high slip velocity, we can see that the evaporation rate is almost three to four times larger than the one shown in Figure 4.15b (case Φ=1-a=55/s-Do=100μm) of the lower slip velocity. However, we should mention that the increased evaporation rate is mainly due to the increase of the imposed strain rate and the consecutive increase of the mass flow rates. Evaporation enhancement due to higher slip velocity is also reported by H. Olguin et al. [65].

Regarding the scalar dissipation rate (χ) which is associated with the gradient of mixture fraction (see equation (2.102)) and is a measure of the local mixing, we should recall that for the gaseous flamelets (see Figure 4.11) only one peak was found, located at the stagnation plane. For the spray flamelets though more peaks for χ are seen as it is shown in Figure 4.16. A local peak at the stagnation plane is also found here mainly due to the diffusion of the fuel products into the opposing oxidizer stream followed by a negative gradient of the mixture fraction. For the case Φ=1-a=55/s-Do=40μm shown in Figure 4.16a an additional peak of χ is observed at the left side of the configuration at the position -0.019m. This can be explained due to the early and intense evaporation that takes place in that region. The droplets have a relatively low momentum and their lifetime is short generating fresh ethanol vapor which is the source for new mixture fraction states. Subsequently, in the region -0.015m to -0.004m where z retains an almost constant value, χ attains a zero value. Increasing the initial droplets' size (Figure 4.16b), the evaporation process is spread to a larger region and this is reflected to the scalar dissipation profile where local peaks are seen. The biggest peak of χ is found close to the stagnation plane where the second reaction zone that resembles a diffusion flame is located. A following increase in the strain rate (Figure 4.16c) makes the droplets oscillate around the stagnation plane leading locally to enhanced evaporation and increased χ. This has as a consequence the formation of a double peak of χ around the stagnation plane. In addition, a significantly lower but visible local maximum of χ is observed at the position of the droplets' reversal (+0.018m) due to local enhanced evaporation rate. Finally, an increase in the equivalence ratio (Figure 4.16d) does not seem to influence the evolution of χ or the mixing conditions with the opposing stream in comparison to the flamelet of Figure 4.16a. As a conclusion we can say that the typical peak of χ found in the gaseous flamelets at the stagnation plane due to the mixing of the opposing streams is also shown here and is almost constant for all the spray cases. The reason for this constant value especially for the case of a=500/s, where we would expect a much larger peak of χ, is because from the one hand the flame might be strained and the mixing with the opposing stream might be quite intense, but on the other hand on the same region evaporation is on progress compensating so the effects of mixing and keeping at a lower level the scalar dissipation rate [65]. Thus, it appears that χ has a strong dependency on the evaporation and not only creates additional peaks but also it may affect the peak at the stagnation plane if evaporation is present there. As a general rule, we can declare that all the spray cases will present at least two peaks for χ corresponding to the two branches of z, while additional peaks should be found at the droplets' reversal positions.

4.4.6. Use of spray flamelets in turbulent flame modeling

As we clearly saw in the previous figures, the evaporation process in the physical space influences the flame structure due to acting locally as an energy sink and the same time creating different local ethanol vapor states. The latter is the reason for mixture fraction not to retain a monotonous curve as it was the case for the gaseous flamelets. Thus, as it was made clear from Figure 4.14, mixture fraction profile in the physical space is mainly consisting of two

branches. Due to this sort of peculiarity, a straightforward representation of the variables in the mixture fraction space is not obvious, since there is not one-to-one correlation between a variable and mixture fraction. A way to overcome this problem is to use the maximum value of mixture fraction in order to separate the fields of variables in a region of monotonically increasing and a region of monotonically decreasing z, as it is also proposed in [68]. This approach is even more preferable for cases where the droplets evaporate early and as a result the region of increasing z can be considered as a spray side, whereas the region of the decreasing z as a gas side since there are no droplets left. In Figure 4.17 for the case Φ=1-a=500/s-Do=100μm, the profiles of temperature, ethanol and oxygen mass fractions and the evolution of droplets' size are shown in the mixture fraction space, following the distinction of the two z branches as we explained. The left part of the figure considers the increasing and the right one the decreasing branch of z. Note that the droplets perform oscillation in that case (see Figure 4.14c) and are found in both z branches. An interesting remark that can be deduced from that figure is that the maximum of ethanol mass fraction is not followed by a maximum value for z as for the gaseous flamelets. This peak of ethanol is found very close to the oxidizer inlet and therefore the mixture fraction which is based on the elemental mass fractions of C and H (see equation (3.10)) is low.

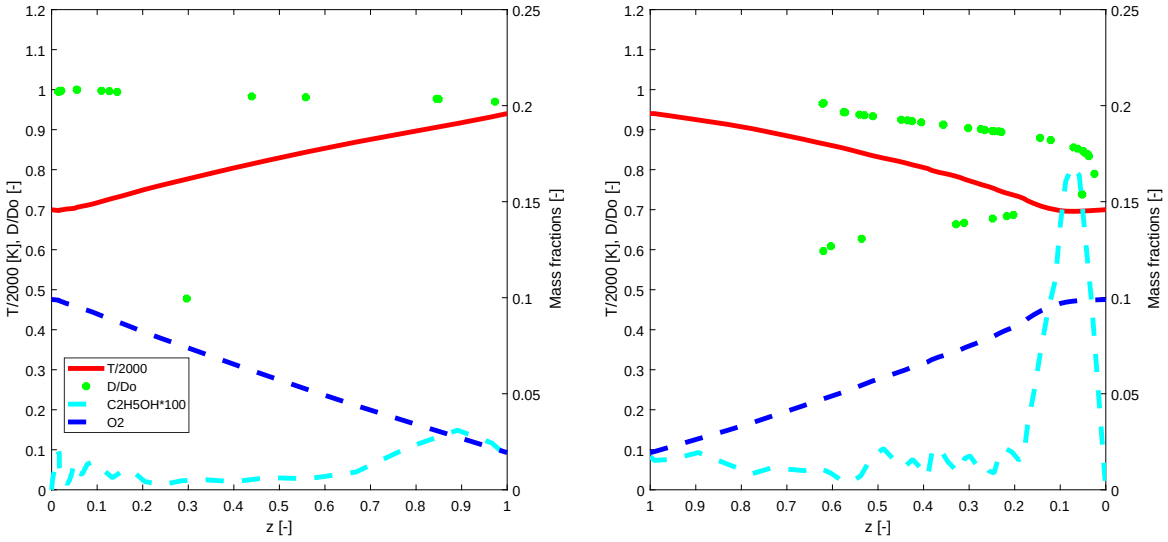

Figure 4.17: Temperature and species profiles in the mixture fraction space for Φ=1, a=500/s, Do=100μm

The connection beetween the turbulence flow calculation and the spray flamelet library remains a subject of discussion and according to the author's knowledge there is no algorithm proposed so far to deal with that kind of complex problem. Nevertheless, we devote these last few words to suggest some ideas that could be possibly evaluated in a future project.

For simplicity we assume that the injector provides mono-dispersed droplets meaning that they have the same initial size. Then in a cell of the turbulence calculation domain we find the droplets that are located there and we track them down to their origin the moment they entered the domain. By tracking their origin we can identify there their initial size and calculate also locally the equivalence ratio. Those two values can be used as boundary conditions (connecting variables) for the spray flamelet library. As we discussed earlier, the mixture fraction (z) is characterized by two branches, so locally at the domain of turbulence calculation

we will need to calculate also the gradient of z. If it is found positive the left branch is used, otherwise the right one (see for example Figure 4.17). The calculation of the z-gradient can be done between the cell that the droplets are currently located and the cell in which they were located in the previous (lagrangian) time step. As a final step, the local values of the mixture fraction and a progress variable can be found solving the corresponding transport equations, according to the method that was explained in the second chapter. If droplets of different sizes found in a cell (poly-dispersed) then it is advised that a weighted summation is applied between the different droplets to calculate the mean fields, where the weight factors should be found with respect to the frequency of the appearance of each droplet size in the cell.

5

Conclusions and Recommendations

5.1. Conclusions

Gradual depletion of fossil fuel sources and the necessity for controlling and limiting the emissions of pollutants that are responsible for the greenhouse effect and the gradual temperature growth of the planet triggers now more than ever to look up for new fuel sources and the same time optimize the current energy processes. Regarding combustion, research is already on progress in order to investigate the prospects of biofuels usage and also use better combustion techniques that reduce the emissions. Following this direction, in this current project we investigated the effects of spray ethanol combustion under MILD (high temperature and low oxygen level of the oxidizer stream) conditions for laminar flames.

In the Theory chapter we saw how the transport equations for (mass, energy and species mass fractions) can be derived for a continuous medium by just balancing the respective surface fluxes and volumetric contributions in a control volume of fluid. In turn, we presented the equations for the discrete phase that rule the motion but also the heat and mass transfer of an ethanol droplet taking into account the effects of evaporation. Then we can solve the two sets of equations in an Eulerian-Lagrangian framework by coupling them with use of source terms. Following, a short discussion was given regarding the nature of the turbulent combustion and the current ways that exist to resolve or model it. Out of all, the FGM approach appears to be a very promising prediction combustion model/tool that allows the use of detailed and multiple chemical-step mechanisms and also offers computational time efficiency. This method is based on solving the chemical reactions in advance and separately from the turbulence flow with the use of one dimensional, laminar counterflow flames (flamelets) and store the results into look-up tables that are retrieved during the resolution of turbulence. When it comes to deal with turbulent spray combustion problems, the question that arises is whether the build up of the look-up table should consider the liquid nature of the fuel. For that reason, in this project, a series of gaseous and spray flamelets are calculated in order to identify the main differences and investigate the influence of spray droplets' motion and evaporation in the flame structure of the flamelets. The outcomes of those calculations can be summarized in the following conclusions:

Regarding the gaseous flamelets, we saw that the strain rate is the only variable that affects the flame structure of a flamelet. This is due to the fact that an increasing strain rate leads to a lesser residence time for the reactants in the reaction zone and as a result weaker reactions are promoted indicated by a lower peak of the temperature. In turn, the mixture fraction

which is an indicator of the local presence of fuel is characterized by monotonicity and varies between a maximum value, z=1, in the fuel side to a minimum one, z=0, in the oxidizer side. This variation of mixture fraction occurs in a thin layer close to the stagnation plane where the two opposing streams mix. Ethanol gas and oxygen mass fraction profiles indicate that the two species diffuse in the domain in a counterflow pattern and only when they are found locally under stoichiometric proportions, reactions take place where also a peak for OH appears. For lower strain rates, ethanol undergoes decomposition and cracking mechanisms (endothermic reactions), which become less significant, giving space for the main reaction to take place as the strain rate increases. The existence of those chemical reactions that lead to decomposition of ethanol into intermediate species is indicated by negative values of the enthalpy chemical reactions source term (heat release). In addition, a peak of the temperature profile coincides with peaks of the heat release and O_2 consumption rate indicating that reactions are locally intense. Finally, the scalar dissipation rate which is indicator of the local mixing, presents a single maximum at the stagnation plane where the two streams mix. This maximum value is proportional to the imposed strain rate.

On the other hand, the flame structure of the spray flamelets, apart from the strain rate is also influenced by the equivalence ratio implied in the fuel side, the initial droplets' diameter and an initial slip velocity (not studied in this report) between the droplets and the carrier gas. The combination of the initial imposed strain rate and droplets' diameter affects the droplets' initial momentum and as a result their motion in the domain. Thus, a lower initial momentum promotes a shorter lifetime of the droplets which is indicated by a short trajectory, while a larger momentum has the droplets penetrate further in the domain. As soon as the droplets cross the stagnation plane and meet the opposing stream one or more reversals are observed. The motion of the droplets is associated with the evaporation process the location of which affects the viability of the flame. Enhanced evaporation at the stagnation plane favors the creation of a double reaction zone. If the ethanol vapor is brought in the reaction zone at a high temperature level a hotter flame compared to the gaseous case can be created. Moreover, if evaporation takes place in regions where combustion is not strong enough, local flame extinction might happen. Thus, not only the residence time of the reactants but also the location and the intensity of the evaporation affect the flame structure. The monotonicity of mixture fraction (z) which is characteristic of the gaseous flamelets is broken for the case of spray flamelets since evaporation creates new z states. Thus, two branches of z-profile are seen, one of increasing z in the fuel side and one of decreasing z in the oxidizer side of the configuration. Mass fraction profiles of CO_2 and H_2O indicate the outer flame structure and follow the temperature profile. Formation of CO occurs prior to CO_2 and is indicator of weakened, incomplete or just started reactions. Local evaporation of the droplets is also predicted by the evaporation source term of the continuity equation and at the location where a local peak is observed additional peaks of the ethanol and oxygen consumption rates are found which are in a stoichiometric ratio. Decomposition of the ethanol gas into intermediate species can occur but is not as evident as for the case of the gaseous flamelets. This is because the droplets are surrounded by the oxidizer the presence of which favors for the main exothermic reation to take place. Considering the relative velocity between the droplets and the carrier gas, droplets' of lower initial momentum remain attached to the streamlines of the gaseous flow. An increase in the initial diameter, creates slip velocity effects which are enhanced for an increase in the strain rate. The higher the slip velocity is the higher the drag force acting upon the droplets will be and this is the main reason for the deceleration of the droplets that follow. As soon as the droplets penetrate into the opposing stream the drag force becomes even higher and this results in the reversal of the droplets. Regarding the equivalence ratio, it can be concluded that it does not affect the trajectory of the droplets or the relative velocity (slip)

between gas and droplets stream nor the region where the evaporation happens. However, it magnifies the rates of evaporation and consumption of fuel and oxygen and prompts for the formation of a second reaction zone due to the excess of ethanol vapor. Finally, the scalar dissipation rate profile shows two maxima that correspond to the two branches of the mixture fraction and additional maxima appear at the droplets' reversal locations. In addition, the evaporation that happens at the stagnation plane can prevent the local scalar dissipation from attaining higher values even if the strain rate is increased. To sum up, the evaporation process and the motion of the droplets significantly influence the flame structure of a flamelet and as a result they have to be captured in the data storage for the generation of the flamelet library.

5.2. Recommendations

After presenting and discussing the obtained results and the working procedure that was followed in this project, a set of recommendations can be proposed in the direction of improving the final results and investigating on additional aspects of the flame structure:

- The simulations of the current project were conducted in a 2D domain where the injector was located in the fuel side providing ethanol droplets at random positions every time step. It is recommended therefore, that the model of the injector be developed further so that a more uniform distribution of droplets is provided. Alternatively, a code dealing with 1D flamelet equations in the physical or the mixture fraction space can be derived so that the computation time be reduced.
- In the derivation of the species mass fraction equation, the species mass diffusivity was replaced by the gas mixture's thermal diffusivity assuming a unity Lewis number. It is recommended that non-unity Lewis numbers should be used for different species to reflect the reality better.
- As it is already mentioned the influences of imposing a slip velocity boundary condition between the droplets and the carrier gas in the flame structure should also be studied. Moreover, an extensive range of values for the strain rate and the initial droplets' diameter should be used so that the igniting and extinguishing flamelets be identified for which unsteady solutions are required. In addition, in order to extend the spray flamelet library, the use of an equivalence ratio that corresponds to lean conditions in the fuel side is advised .
- It is advised that an adaptive mesh refinement approach is used in regions of increasing temperature gradients in the domain so that the reaction zone is predicted more accurately.
- In this project the Marinov chemical scheme is used including 57 species and 383 intermediate chemical reactions. It is a detailed scheme that is used to predict accurately the distributions of the species and the flame structure. However, the more reactions are included in a scheme the stiffer the calculation becomes reducing the chemical time step and as a result increasing the computational time. For that reason, it is recommended that for the same configuration we studied in this project, different chemical schemes of varying number of species and reactions should be used and a map that will relate the different schemes with respective accuracy and computational efficiency should be created, so that the most optimum scheme will be used in future studies decreasing the computational cost without loosing in terms of accuracy.

- For the case of the spray flamelets, the mixture fraction presents a non-monotonous profile which makes the representation of the variables in the mixture fraction space multivalued. For that reason, it is recommended that a new definition of mixture fraction should be investigated that will have it maintain the monotonicity even under spray conditions (for details see [69]).
- An efficient method that will connect the parameters that work as coordinates of the spray flamelet library with the turbulence calculation in every cell of the domain should be investigated.

Bibliography

[1] J. D. Anderson, *Fundamentals of Aerodynamics* (McGraw-Hill Education, 2010).

[2] L. Ma, *Computational Modeling of Turbulent Spray Combustion* (PhD thesis, TU Delft, 2016).

[3] International Energy Agency (IEA), *Key world energy statistics* (2016).

[4] International Energy Agency (IEA), *Annual Energy Outlook 2017 with projections to 2050* (2017).

[5] A. Cavaliere and M. de Joannon, *Mild Combustion,* Progress in Energy and Combustion Science **30**, 329 (2004).

[6] P. S. Nigam and A. Singh, *Production of liquid biofuels from renewable resources,* Progress in Energy and Combustion Science **37**, 52 (2011).

[7] A. Demirbas, *Progress and recent trends in biofuels,* Progress in Energy and Combustion Science **33**, 1 (2007).

[8] Food and Agriculture Organization of the United Nations (FAO), *The state of food and agriculture* (2008).

[9] J. van Oijen., *Flamelet-Generated Manifolds: Development and Application to Premixed Laminar Flames.* (PhD thesis, Eindhoven University of Technology, 2002).

[10] H. C. Rodrigues, *Spray combustion in moderate and intense low-oxygen conditions: An experimental study* (PhD thesis, TU Delft, 2015).

[11] CHEM1D, *A one-dimensional laminar flame code, Eindhoven University of Technology,* (URL:http://www. combustion. tue. nl/chem1d//).

[12] K. Karamcheti, *Principles of Ideal-Fluid Aerodynamics* (Krieger Pub Co, 1980).

[13] H. T. Schlichting, *Boundary Layer Theory* (McGraw-Hill Science/Engineering/Math, 1979).

[14] T. Poinsot and D. Veynante, *Theoretical and Numerical Combustion, Second Edition* (R.T. Edwards, Inc., 2005).

[15] S. S. Sazhin, *Advanced models of fuel droplet heating and evaporation,* Progress in energy and combustion science **32**, 162 (2006).

[16] G. H. Ko and H. S. Ryou, *Droplet collision processes in an inter-spray impingement system,* Journal of Aerosol Science **36**, 1300 (2005).

[17] E. Gutheil, *Issues in computational studies of turbulent spray combustion,* in *Experiments and Numerical Simulations of Diluted Spray Turbulent Combustion* (Springer, 2011) pp. 1–39.

[18] M. Gorokhovski and M. Herrmann, *Modeling primary atomization,* Annu. Rev. Fluid Mech. **40**, 343 (2008).

[19] P. Jenny, D. Roekaerts, and N. Beishuizen, *Modeling of turbulent dilute spray combustion,* Progress in Energy and Combustion Science **38**, 846 (2012).

[20] M. Vujanović, W. Edelbauer, E. Von Berg, R. Tatschl, and N. Duić, *Enhancement and validation of an eulerian-eulerian approach for diesel sprays,* in *Proceedings of the ILASS Europe Conference, Paper* (2008) pp. 2–4.

[21] E. Amani and M. Nobari, *Systematic tuning of dispersion models for simulation of evaporating sprays,* International Journal of Multiphase Flow **48**, 11 (2013).

[22] J. Shirolkar, C. Coimbra, and M. Q. McQuay, *Fundamental aspects of modeling turbulent particle dispersion in dilute flows,* Progress in Energy and Combustion Science **22**, 363 (1996).

[23] L. Schiller and A. Naumann, *A drag coefficient correlation,* V.D.I. Zeitung **75**, 318 (1935).

[24] M. Yuen, *Numerical study of droplet evaporation in a high-temperature stream,* Journal of Heat transfer **105**, 389 (1983).

[25] B. Abramzon and W. Sirignano, *Droplet vaporization model for spray combustion calculations,* International journal of heat and mass transfer **32**, 1605 (1989).

[26] S. Sazhin, W. Abdelghaffar, E. Sazhina, and M. Heikal, *Models for droplet transient heating: effects on droplet evaporation, ignition, and break-up,* International journal of thermal sciences **44**, 610 (2005).

[27] S. Sazhin, T. Kristyadi, W. Abdelghaffar, and M. Heikal, *Models for fuel droplet heating and evaporation: comparative analysis,* Fuel **85**, 1613 (2006).

[28] R. Miller, K. Harstad, and J. Bellan, *Evaluation of equilibrium and non-equilibrium evaporation models for many-droplet gas-liquid flow simulations,* International Journal of Multiphase Flow **24**, 1025 (1998).

[29] R. B. Bird, W. E. Stewart, and E. N. Lightfoot, *Transport Phenomena* (John Wiley & Sons, 1960).

[30] L. Ma, B. Naud, and D. Roekaerts, *Transported pdf modeling of ethanol spray in hot-diluted coflow flame,* Flow, Turbulence and Combustion **96**, 469 (2016).

[31] G. Hubbard, V. Denny, and A. Mills, *Droplet evaporation: effects of transients and variable properties,* International Journal of Heat and Mass Transfer **18**, 1003 (1975).

[32] C. Law and F. Williams, *Kinetics and convection in the combustion of alkane droplets,* Combustion and Flame **19**, 393 (1972).

[33] P. Sagaut, *Multiscale And Multiresolution Approaches In Turbulence* (Icp, 2006).

[34] F. T. Nieuwstadt, J. Westerweel, and B. J. Boersma, *Turbulence: Introduction to Theory and Applications of Turbulent Flows* (Springer, 2016).

[35] N. Peters, *Turbulent Combustion (Cambridge Monographs on Mechanics)* (Cambridge University Press, 2000).

[36] S. B. Pope, *Turbulent Flows* (Cambridge University Press, 2000).

[37] J. van Oijen, L. de Goey, and D. Roekaerts, *Course on Combustion* (Technische Universiteit Eindhoven, 2013).

[38] H. Bao, *Development and Validation of a New Eddy Dissipation Consept (EDC) Model for MILD Combustion* (MSc thesis, TU Delft, 2017).

[39] N. Peters, *Reducing mechanisms,* in *Reduced Kinetic Mechanisms and Asymptotic Approximations for Methane-Air Flames: A Topical Volume*, edited by M. D. Smooke (Springer Berlin Heidelberg, Berlin, Heidelberg, 1991) pp. 48–67.

[40] F. Mauss and N. Peters, *Reduced kinetic mechanisms for premixed methane-air flames,* in *Reduced Kinetic Mechanisms for Applications in Combustion Systems*, edited by N. Peters and B. Rogg (Springer Berlin Heidelberg, Berlin, Heidelberg, 1993) pp. 58–75.

[41] U. Maas and S. Pope, *Simplifying chemical kinetics: Intrinsic low-dimensional manifolds in composition space,* Combustion and Flame **88**, 239 (1992).

[42] N. Peters, *Laminar diffusion flamelet models in non-premixed turbulent combustion,* Progress in Energy and Combustion Science **10**, 319 (1984).

[43] M. Ihme and Y. C. See, *Prediction of autoignition in a lifted methane/air flame using an unsteady flamelet/progress variable model,* Combustion and Flame **157**, 1850 (2010).

[44] S. Pope, *Pdf methods for turbulent reactive flows,* Progress in Energy and Combustion Science **11**, 119 (1985).

[45] B. Naud, R. Novella, J. M. Pastor, and J. F. Winklinger, *RANS modelling of a lifted H_2/N_2 flame using an unsteady flamelet progress variable approach with presumed PDF,* Combustion and Flame **162**, 893 (2015).

[46] M. Chrigui, J. Gounder, A. Sadiki, A. R. Masri, and J. Janicka, *Partially premixed reacting acetone spray using LES and FGM tabulated chemistry,* Combustion and Flame **159**, 2718 (2012), special Issue on Turbulent Combustion.

[47] H. Olguin and E. Gutheil, *Theoretical and numerical study of evaporation effects in spray flamelet modeling,* in *Experiments and Numerical Simulations of Turbulent Combustion of Diluted Sprays* (Springer International Publishing, 2014) pp. 79–106.

[48] *OpenFOAM, The open source CFD toolbox,* http://www.openfoam.com/ ().

[49] *Conquering C++,* http://www.sstutor.com/cpp/contents.aspx.

[50] C. J. Greenshields, *OpenFOAM - The Open Source CFD Toolbox - User's Guide*, OpenCFD Ltd., United Kingdom, 4th ed. (2016).

[51] *OpenFOAM/OpenFOAM-2.3.x,* https://github.com/OpenFOAM/OpenFOAM-2.3.x ().

[52] N. M. Marinov, *A detailed chemical kinetic model for high temperature ethanol oxidation,* International Journal of Chemical Kinetics **31**, 183 (1999).

[53] *Openfoam Wiki,* https://openfoamwiki.net/.

[54] F. Moukalled, L. Mangani, and M. Darwish, *The Finite Volume Method in Computational Fluid Dynamics: An Advanced Introduction with OpenFOAM® and Matlab (Fluid Mechanics and Its Applications)* (Springer, 2015).

[55] J. H. Ferziger and M. Perić, *Computational Methods for Fluid Dynamics* (Springer Berlin Heidelberg, 2002).

[56] C. J. Greenshields, *OpenFOAM - The Open Source CFD Toolbox - Programmer's Guide*, OpenCFD Ltd., United Kingdom, 3rd ed. (2015).

[57] S. Patankar and D. Spalding, *A calculation procedure for heat, mass and momentum transfer in three-dimensional parabolic flows,* International Journal of Heat and Mass Transfer **15**, 1787 (1972).

[58] R. Issa, *Solution of the implicitly discretised fluid flow equations by operator-splitting,* Journal of Computational Physics **62**, 40 (1986).

[59] R. Barlow, J. Frank, A. Karpetis, and J.-Y. Chen, *Piloted methane/air jet flames: Transport effects and aspects of scalar structure,* Combustion and Flame **143**, 433 (2005).

[60] A. VALLIER, *Tutorial icoLagrangianFoam / solidParticle* (CFD WITH OPENSOURCE SOFTWARE, ASSIGNMENT 3, LUND TEKNISKA HOGSKOLA, 2010).

[61] R. L. Gordon, A. R. Masri, and E. Mastorakos, *Simultaneous Rayleigh temperature, OH- and CH2O-LIF imaging of methane jets in a vitiated coflow,* Combustion and Flame **155**, 181 (2008).

[62] J. Greenberg and N. Sarig, *An analysis of multiple flames in counterflow spray combustion,* Combustion and Flame **104**, 431 (1996).

[63] T. Lin and S. Sohrab, *On the transition of diffusion to premixed flames in conserved systems,* Combustion and Flame **68**, 73 (1987).

[64] E. Gutheil and W. Sirignano, *Counterflow spray combustion modeling with detailed transport and detailed chemistry,* Combustion and Flame **113**, 92 (1998).

[65] H. Olguin, P. Hindenberg, and E. Gutheil, *Numerical and theoretical analysis of laminar counterflowing spray flames for use in turbulent combustion modeling,* in *ASME 2014 4th Joint US-European Fluids Engineering Division Summer Meeting collocated with the ASME 2014 12th International Conference on Nanochannels, Microchannels, and Minichannels* (American Society of Mechanical Engineers, 2014) pp. V01CT15A013–V01CT15A013.

[66] G. Continillo and W. Sirignano, *Counterflow spray combustion modeling,* Combustion and Flame **81**, 325 (1990).

[67] N.-H. Chen, B. Rogg, and K. Bray, *Modelling laminar two-phase counterflow flames with detailed chemistry and transport,* Symposium (International) on Combustion **24**, 1513 (1992), twenty-Fourth Symposium on Combustion.

[68] H. Olguin and E. Gutheil, *Influence of evaporation on spray flamelet structures,* Combustion and Flame **161**, 987 (2014).

[69] B. Franzelli, A. Vié, and M. Ihme, *On the generalisation of the mixture fraction to a monotonic mixing-describing variable for the flamelet formulation of spray flames,* Combustion Theory and Modelling **19**, 773 (2015), http://dx.doi.org/10.1080/13647830.2015.1099740 .